TECHNISCHE UNIVERSITÄT MÜNCHEN
Lehrstuhl für Messsystem- und Sensortechnik

Laser-based Measurement Systems for Space Applications

Markus Plattner

Vollständiger Abdruck der von der Fakultät für Elektrotechnik und Informationstechnik der Technischen Universität München zur Erlangung des akademischen Grades eines

Doktor-Ingenieurs

genehmigten Dissertation.

Vorsitzender: Univ.-Prof. Dr. rer. nat. habil. Bernhard Wolf

Prüfer der Dissertation:

1. Univ.-Prof. Dr.-Ing. Dr. h.c. Alexander W. Koch
2. Univ.-Prof. Dr.-Ing. Klaus Brieß, Technische Universität Berlin

Die Dissertation wurde am 17.10.2011 bei der Technischen Universität München eingereicht und durch die Fakultät für Elektrotechnik und Informationstechnik am 28.03.2012 angenommen.

Abstract

Measurement systems based on laser technology are widely used in laboratories, metrology institutes and industry. Measurement applications like optical sensing and optical spectroscopy are state of the art. For space applications, however, laser systems are rarely used due to the sensitivity of optical components to the harsh environmental conditions. The focus of this work lies on further development of laser technologies for the applications optical frequency comb generation and fiber-optic sensing. In order to identify suitable laser technologies, the conditions for systems that shall be operated in space are analyzed thoroughly. The influences due to the space environment are considered and the radiation and temperature effects on laser optics are determined.

Commercially available femtosecond fiber lasers based on mode-locking technologies non-linear polarization rotation and quasi-soliton generation are functionally tested in order to verify the theoretical analysis. Thermal-vacuum and Gamma radiation test series are carried out and the performance of the lasers is measured online. Evaluation of measurement data, assessment of laser setups in terms of robustness and their behaviors during tests allow concluding an optimized femtosecond laser design. This design serves as baseline for further development and will yield a system that can cope with the requirements for an application in space.

In order to demonstrate the functionality of fiber-optic sensing based on a tunable laser diode, an interrogator system is built and tested in the frame of this work. This technology, based on a monolithic laser, enables an all-in-fiber setup without any free-space optics. The laser wavelength is tuned by feeding in three control currents. Thereby, the connected fiber Bragg grating temperature sensors are sampled spectrally. Newly developed algorithms enhance the measurement performance, evaluate the back reflected sensor responses and determine the measurement value.

This work was carried out in the frame of several projects partly funded by the German and European Space Agencies DLR and ESA. The results of this work flow into successor projects aiming at the development of the described measurement systems as space qualified instruments.

Zusammenfassung

Laser basierte Messsysteme sind in Laboren, in Metrologie Instituten und in der Industrie weit verbreitet. Messapplikation wie optische Sensorik und Spektroskopie sind Stand der Technik. Für Anwendungen im Weltraum sind Lasersysteme, wegen ihrer Empfindlichkeit gegenüber den vorherrschenden Umgebungsbedingungen, jedoch selten im Einsatz. Der Schwerpunkt dieser Arbeit liegt in der Weiterentwicklung von Lasertechnologien für die Anwendungen als optischer Frequenzkammgenerator und zur faser-optischen Sensorik. Um geeignete Lasertechnologien auszuwählen wird eine gründliche Analyse durchgeführt, mit dem Ziel die Bedingungen für den Betrieb von Systemen im Weltraum zu charakterisieren. Verschiedene Annahmen für wechselnde Umgebungsbedingungen im Weltraum werden betrachtet und die Effekte auf Laseroptik durch Bestrahlung und Temperaturänderungen analysiert.

Kommerziell erhältliche Femtosekundenlaser basierend auf den Modenkopplungstechnologien nicht-lineare Polarisationsrotation und Quasi-Soliton Generierung werden funktionell und unter wechselnden Umgebungsbedingungen getestet um die theoretische Analyse zu verifizieren. Thermal-Vakuum und Gamma Bestrahlungstests werden durchgeführt während die Betriebseigenschaften der Laser in Echtzeit gemessen werden. Die Auswertung der Messdaten, die Bewertung der Laseraufbauten bezüglich Robustheit und das Verhalten der Laser während der Tests ermöglichen den Entwurf eines optimierten Femtosekundenlasers. Dieses Design ist die Basis für zukünfige Entwicklungen welche ein System hervorbringen, dass mit den Bedingungen im Weltraum zurechtkommt.

Um die Funktionalität von faser-optischer Sensorik basierend auf einem Laser mit verstimmbarer Ausgangswellenlänge zu demonstrieren wird im Rahmen dieser Arbeit ein Interrogatorsystem entworfen, aufgebaut und getestet. Diese Technologie, basierend auf einer monolithischen Laserdiode ergibt einen robusten faserbasierten Aufbau ohne Freistrahlstrecken. Die Ausganswellenlänge des Lasers wird durch das Einspeisen von drei Kontrollströmen verstimmt, dadurch werden angeschlossene Faser Bragg Gitter Temperatursensoren abgetastet. Neu entwickelte Algorithmen verbessern die Messperformance, werten die reflektierten Sensorantworten aus und bestimmen die aktuelle Messgröße.

Diese Arbeit wurde im Rahmen mehrerer Projekte der nationalen und europäis-

chen Raumfahrtagenturen DLR und ESA durchgeführt. Die Ergebnisse dieser Arbeit fließen in Nachfolgeprojekte ein, mit dem Ziel weltraum-qualifizierte Instrumente zu entwickeln.

Contents

1. Introduction

Within this work, space borne optical technologies in the fields of frequency measurement and fiber based sensing are further developed. In order to reach the required high technological readiness of a system to be able to pass space qualification tests, complex research and development processes have to be carried out. Due to the high costs of bringing and operating systems in space, the risk for a potential failure of the system has to be reduced to the minimum.

1.1. Photonics in Space - State of the Art and Ongoing Developments

Several fundamental physics experiments and future trends for existing space technologies based on photonics are already under development or have been proposed [18]. This chapter gives an overview of state-of-the-art measurement systems based on frequency standards and optical fiber sensing with regard to space applications.

1.1.1. Optical Frequency Measurement

The invention of optical frequency comb technology resulted in a simplified method for the measurement of optical frequencies [146][171][186]. In order to benefit from this new technology, frequency combs are used in scientific laboratories and optical frequencies are distributed to enable comparison of frequency standards [118]. The technology is further developed towards compact ultrafast lasers which is a first step for achieving a more robust system [85].

Up to now optical frequency measurement based on optical frequency combs (OFC) is available in laboratories only. Commercial OFCs are available, but

these systems cannot cope with the environment in space. In order to support future missions based on optical atomic clocks (OAC), like the proposed Einstein Gravity Explorer [160] with an OFC, further development has been initiated by the European and the German Space Agencies, ESA and DLR. In line with this work, available OFC technologies are examined for the use in space environment and promising subsystem candidates are evaluated by elaborate environmental tests. The results obtained by this work enable the design and development of an OFC based on the best suited technology for a space-borne system.

In the field of frequency standards and clocks, several missions are currently under development or have already been started. The ACES (atomic clock ensemble in space) mission develops a Cesium fountain atomic clock that will be operated onboard the international space station ISS [24]. The most accurate frequency standard in space today is the hydrogen maser onboard the GIOVE (Galileo in orbit verification) satellite [188]. The SOC (space optical clocks) [161] project is the first development of an optical frequency standard towards a compact and transportable system.

Optical frequency combs as one major subsystem of an OAC are, up to now, not available in a space qualified version. Therefore OFC technology is the focus of ESA and DLR initiated projects (see appendix A.1).

1.1.2. Optical Fiber Sensing

Fiber based sensing is currently no standard technology for space applications. The advantages of fiber optic sensing in spacecrafts have been theoretically and practically studied in several space related projects [116] but until now sensing is dominated by electrical means. In particular, thermal mapping with high numbers of temperature sensors is one application wherefore fiber based sensing would enhance the measurement in terms of reduced complexity and weight. Therefore, the lower maturity of optical compared to electrical technologies required for fiber optic sensing in space has to be overcome by further development.

Several studies have already been carried out having in view the utilization of

fiber optic sensing in space [116][38][57]. Up to now only one fiber Bragg grating (FBG) interrogator, developed by MPB Communications, has been developed for space flight demonstration onboard the PROBA-2 satellite [97][98]. This interrogator provides six external sensor channels. Four of the channels support fibers that accommodate up to four FBG sensors each, the fifth and sixth channel read out one high temperature and one combined temperature-pressure sensor respectively. Since this system is used for feasibility demonstration on-board a low Earth orbit satellite where environmental loads and mission lifetime are low, it is built on commercial components without space qualification.

Within this work an alternative fiber-optic interrogation breadboard based on a monolithic laser diode is designed, developed and tested. This scanning-laser sensing technology would significantly enhance sensing on spacecrafts.

1.2. Objective

The main objectives of optical frequency comb and optical fiber sensing development, which are in focus of this work, are described within this section.

1.2.1. Optical Frequency Comb Development

The main objective of the work on optical frequency comb (OFC) development are investigations on existing OFC technologies in terms of applicability for space use. Therefore a detailed literature inquiry and a trade-off between available technologies have been carried out. Two selected OFCs based on fiber lasers are further analyzed by environmental testing at subsystem level. Thermal-vacuum and Gamma-radiation tests are performed and new results concerning optical output performance are described. Differences in the levels of radiation induced degradation are observed when the fibers are illuminated with high intense pulses. This would allow system lifetime extension by permanent operation. Design conclusions for further development of a space-borne OFC are drawn and a development roadmap is established in the conclusion.

1.2.2. Optical Fiber Sensing Development

The main objective of the work on optical fiber sensing (OFS) is to identify the potential benefits of fiber optic instrumentation for launchers (e.g. Ariane, Vega) and to demonstrate the feasibility and functional performance with a representative interrogation demonstrator. Therefore an interrogator based on a modulated-grating tunable laser diode is developed and functionally tested. A measurement accuracy below ± 0.5 K and a sensor sample rate of up to 10 kHz is achieved, which is comparable to existing conventional instrumentation and fulfills the performance requirements for temperature sensing on board launchers. New measurement algorithms, peak-tracking and time-of-flight, are developed in order to enhance the measurement performance. A roadmap for further development of the scanning laser based interrogator is given in the conclusion.

1.3. Outline

In chapter 2, the implementation of an OFC inside an optical atomic clock (OAC), which is one main application of an OFC, is described. First, optical atomic clock technology is introduced in section 2.1. The principle architecture of OACs and differences between single-ion and lattice clocks are explained in section 2.2. An all-optical atomic clock based on clock stabilization using an OFC is illustrated in detail in section 2.3. In section 2.4, the requirements for an OFC to be used in an OAC are given. Simulation results shown in section 2.5 demonstrate the positioning performance benefits of OACs operated in global navigation satellite systems (GNSS).

Chapter 3 treats linear and non-linear optical phenomena in view of metrological purposes. In section 3.1, the differences between linear and nonlinear optics are described. Second harmonic generation is introduced and related to applications in OFC and OAC technology in section 3.2. Furthermore, intensity dependence of optical material properties are summarized and resulting effects that enable mode-locking are explained in section 3.3. The theoretical principles of phase matching are shown in section 3.4. The basics of multiple wave

interferences as they occur in OFC and in OFS are derived in sections 3.5 and 3.6 and illustrated by simulation results.

The theory of OFC generation and stabilization is outlined in chapter 4. The optical frequency comb is defined in section 4.1. Optical frequency measurement based on heterodyne beat detection is explained in section 4.2. Section 4.3 shows the general architecture of an OFC. The core element of an OFC is the ultra-short pulsed laser. Alternative designs and mode-locking principles of this element are described in section 4.4. OFC stabilization based on f-2f interferometry is discussed in section 4.5.

Optical fiber sensing (OFS) is introduced in chapter 5. The main advantages of OFS for spacecraft monitoring are given in section 5.1 and the principle of fiber Bragg grating (FBG) based sensing is outlined in section 5.2. Different interrogation technologies are introduced in section 5.3 and the technology of MG-Y lasers is presented in section 5.4.

Chapter 6 points out the characteristics of developing systems for space applications. Section 6.1 outlines the characteristics and constraints of developing space-borne systems. The space radiation environment and its effects on electric and optical components are illustrated in section 6.2. Issues due to microgravity, vacuum, shock and vibration are outlined in sections 6.3 and 6.4.

The development of OFC technology for space applications which has been carried out in the frame of this work is described in chapter 7. In section 7.1, a trade-off between the available technologies from the space engineering point of view is carried out. Two laser systems based on mode-locking principles nonlinear polarization rotation and SESAM based soliton generation are described in section 7.2. Test plans and test environments that have been established are shown in section 7.3. Thermal-vacuum tests have been carried out in section 7.4 in order to identify the temperature range in which the lasers are able to operate. The measurement results are compared with thermal simulations for verification. The results of extensive Gamma radiation test series are summarized in section 7.5. Three different test setups have been used in order to investigate the important effects of radiation on mode-locked fiber lasers during operation.

In chapter 8, the development of the scanning laser breadboard is summarized. A trade-off between interrogation technologies in view of implementation in

space is given in section 8.1. The interrogation principle of the chosen scanning laser system is explained in section 8.2. The hardware architecture based on a DSP and FPGA controlled MG-Y laser diode is shown in section 8.3. Section 8.4 describes the characterization of the interrogation setup and the reason for non-equidistant sampling. The soft- and firmware architectures based on the developed peak-tracking and time-of-flight algorithms are demonstrated in section 8.5. The evaluation of tests carried out with the scanning laser interrogation system are outlined in section 8.6.

The conclusion of this work is given in chapter 9. The results of OFC development and the roadmap for further development towards a space borne system are summarized in sections 9.1 and 9.2. Scanning laser development results and the roadmap for further development are discussed in sections 9.3 and 9.4.

2. Optical Atomic Clocks in Space - Motivation for Future Missions

This chapter introduces the principles of optical atomic clocks (OAC). First, OACs are introduced generally in section 2.1 and their operation principles are explained in section 2.2. A possible setup for an all-optical atomic clock based on an optical frequency comb (OFC) is illustrated in section 2.3. Requirements for OFCs to be used as clockwork in an OAC are outlined in section 2.4. Finally, in section 2.5, potential benefits using OACs in satellite navigation systems which is one major space application are summarized.

2.1. Optical Atomic Clock Technology

Any type of clock consists of an oscillator that produces pulses at a constant rate and a counter that adds up the single pulses of the clock oscillator [10]. Pendulum clocks for example use the swinging of a pendulum as clock oscillator and a mechanical clockwork rotates the clock hands which together with the clock face form the counter. The term optical atomic clock (OAC) refers to a type of clock of which the oscillator is frequency-coupled to an optical transition of a reference particle [147]. An ultra-stable laser serves as the oscillator that probes this atomic transition. For many applications however, the stability and accuracy of the optical frequency of the laser has to be converted to the radio-frequency regime in order to allow signal processing by electronic means. Therefore the optical frequency comb servers as "gear-box" and transfers the optical into a radio-frequency.

The high optical frequency of the oscillator in the hundred Terra-Hertz region in principle allows very accurate measurement of time. Compared to todays standard, the oscillator frequency of an optical standard is roughly by a factor

of 50000 higher than that of the cesium standard. This is comparable to the difference between a pendulum clock that oscillates once a second and a quartz clock with an oscillation frequency of approximately 33 kHz.

Figure 2.1 shows the development and improvement of microwave and optical standards for the last decades. Recently optical standards have been produced that have higher stability and accuracy than the current microwave fountain standards (e.g. NIST-F1). This goes along with the problem that the second as defined internationally by the cesium clocks can no longer be used for calibration and comparison of newly developed optical standards. Two optical standards have to be compared mutually, when their accuracy exceeds the microwave standard unless the second is redefined by means of optical standards [63].

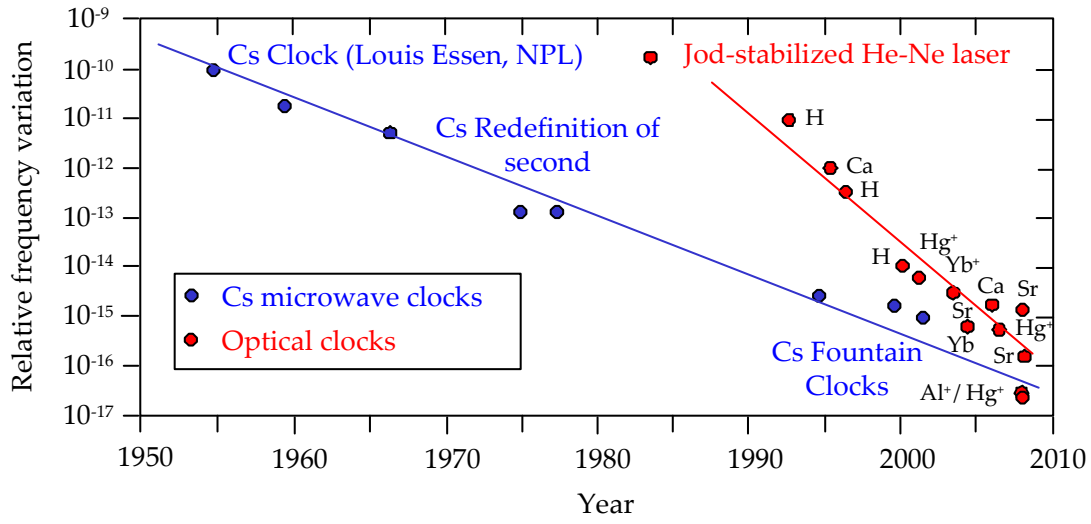

Fig. 2.1.: Overview of the improvement of clock stability over the last decades according to [88]. Optical standards show a steeper gradient indicating that their development progress is higher.

The higher accuracy and stability of optical standards gives rise to numerous applications e.g. verification of fundamental physic laws and constants [147], enhanced optical communication or improved global navigation satellite systems (GNSS). The latter application, and the possible improvements that can be achieved by the use of optical clocks are described in chapter 2.5.

2.2. Operation Principle of an OAC

The main subsystems of optical atomic clocks (OAC) are a trap which confines the reference particle(s), an ultra-stable clock laser that probes the reference particle(s) and an optical frequency comb that transforms the optical frequency of the clock laser and its stability and accuracy into the radio frequency domain [111][61].

OAC technology can be divided into two categories, the first type is based on a single ion trapped in an electromagnetic field, whereas the other type confines a high number of neutral atoms in an optical lattice. The most accurate and precise clocks are quantum logic clocks based on Mercury and Aluminum ions [26][150][80]. This type of OAC has a higher complexity since an additional ion is trapped that is required for cooling and clock transition probing [162]. Therefore quantum logic clocks are not considered for further development towards a space-borne system within this work. An overview of systems that could be developed for operation in space is given in [61], [32] and [62].

Although single-ion and optical lattice clocks are rather different from each other, the basic operation principle is the same: The reference particle is confined in a laser cooled trap. As long as the particle is in its ground state, laser cooling yields fluorescence that is monitored by a photo detector. An ultra-stable laser probes an optical transition of the reference particle. If the probe laser frequency matches the transition frequency, the particle changes to a different energy level. At this upper state, the laser cooling fluorescence disappears. Thereby it is monitored if the clock laser frequency matches the particle(s) transition frequency [113]. A feedback electronic continuously tunes the clock laser frequency such that the single reference particle is excited with highest probability in the case of a single-ion clock, respectively that the majority of all particles is excited in the case of an optical lattice clock. The probe laser frequency is then transferred to the rf-region by an optical frequency comb in order to achieve an all optical self-stabilizing clock (see section 2.3).

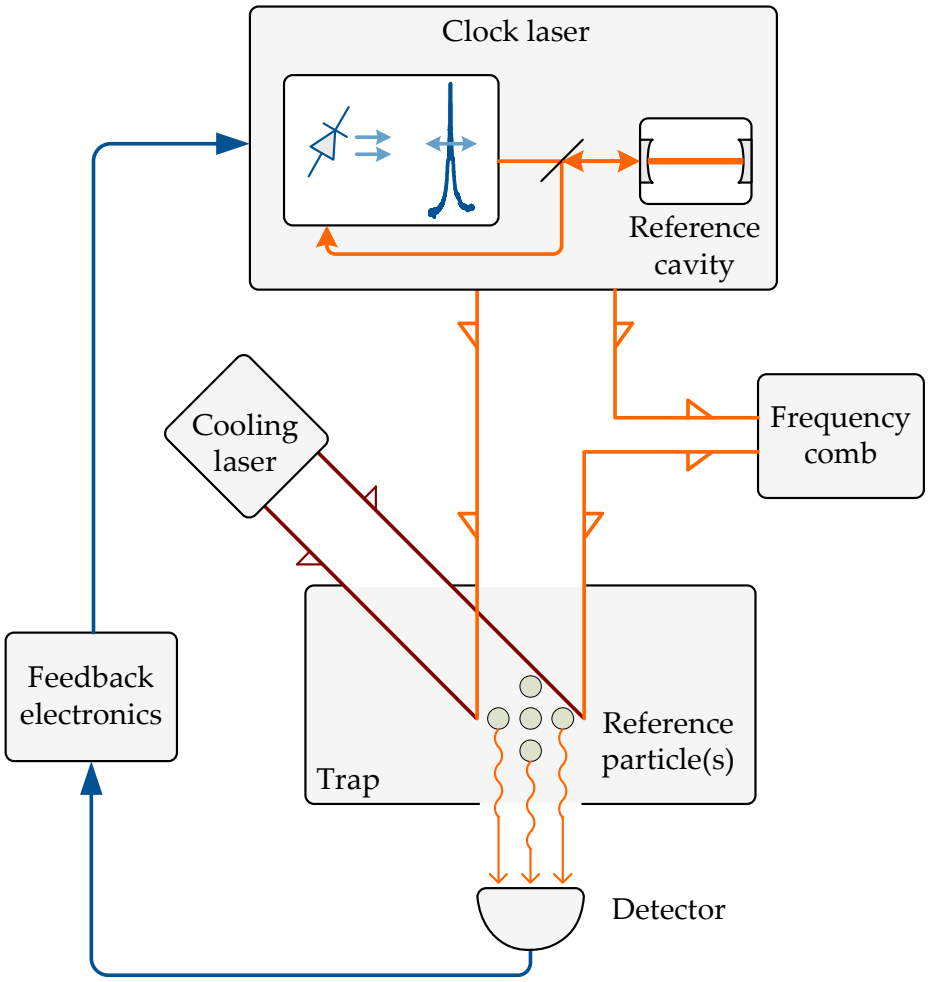

Fig. 2.2.: Principle block diagram of an optical atomic clock (OAC). The reference particle(s) are confined in a laser cooled trap. Feedback electronics tunes the clock laser frequency such that it matches the reference transition of the particle(s) and the particle is excited. The optical frequency comb transfers the clock laser frequency to the rf regime.

The detailed setup of an optical clock is determined by the reference particle(s). The main criteria for the choice of a reference atom are:

- The optical reference transition has a very narrow bandwidth and therefore a long upper-state lifetime, also called a meta-stable or forbidden transition. According to [147] the lifetime τ of a transition is reciprocally proportional to the linewidth of the transition $\Delta\omega$

$$\Delta\omega = {}^{1}/_{\tau}. \tag{2.1}$$

A long upper-state lifetime allows a long interrogation time and yields a narrow frequency linewidth.

- Additional transitions that can be used for laser cooling are available. The atom has to be confined to a spatial region at the size of the probe wavelength [113]. This is achieved by a combination of electromagnetic or magneto-optic traps and laser Doppler cooling.
- All wavelengths used for probing and cooling have to be accessible by means of lasers. For the development of space borne optical clocks, the types of required lasers have to be able to cope with the environmental conditions e.g. vacuum and radiation. Therefore diode, fiber and other solid state lasers are preferred (see chapter 6).

Figure 2.3 shows a simplified energy level scheme of a Strontium ion clock as example [62]. Additionally to the reference transition, that is probed by

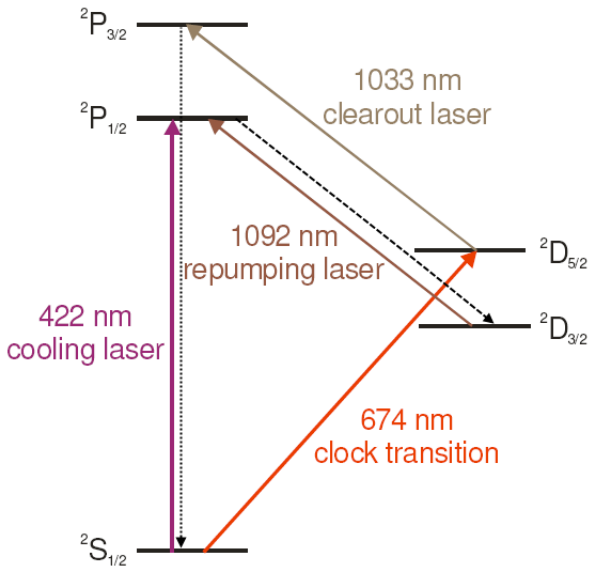

Fig. 2.3.: Simplified transition scheme of a Strontium ion. Clock, cooling, clear-out and re-pumper transition are shown [62].

the clock laser at a wavelength of 674 nm, three other laser wavelengths are required. A wavelength at 422 nm is used for laser Doppler cooling. With a probability of $\approx 8\%$, the ion decays to the meta-stable level $^2D_{3/2}$ from the upper cooling state $^2P_{1/2}$ (dashed line). Therefore a repumping laser at 1092 nm is

used to ensure continuous operation. Furthermore a clear-out laser (dotted line) at a wavelength of 1033 nm returns the ion into the ground state after the clock transition has been probed.

Clock Laser

Atomic transitions of the reference particles have linewidths at Hertz level or below. In order not to lose accuracy when probing the transition, the probe laser also needs a linewidth lower than one Hertz [114]. State of the art commercially available diode and solid-state lasers have linewidths of several hundred Hertz to mega Hertz. Therefore special techniques have been developed for achieving such narrow linewidths mainly due to reduction of noise from different sources [187].

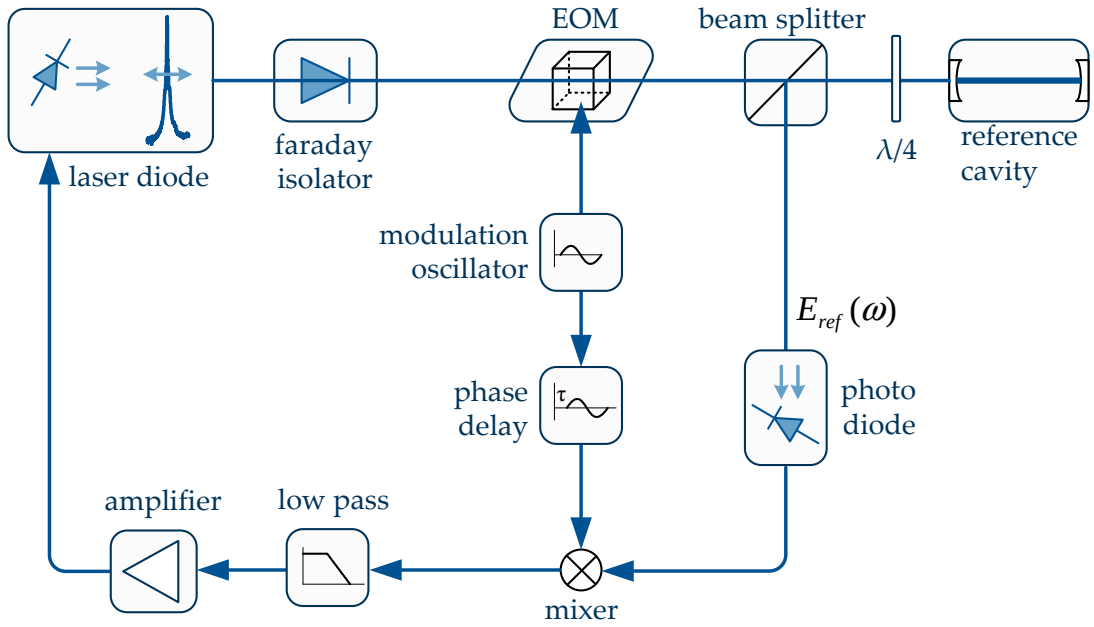

Fig. 2.4.: Pound-Drever-Hall locking for laser stabilization [17]. An electro-optical modulator shifts the laser frequency towards a cavity mode. The mixed signal is measured and a feedback control loop locks the laser to the cavity mode.

Commonly the laser is stabilized to a high finesse optical cavity to achieve high short-term stability [5] by the Pound-Drever-Hall locking technique [35].

An electro-optic modulator (EOM) is used to tune the laser frequency. If the frequency of the laser matches one resonance frequency of the cavity, the reflected intensity shows maximum magnitude. Mixing the modulating signal of the EOM (usually of sinusoidal form) with the intensity signal measured by a photo detector yields the difference frequency of both input frequencies as error signal. This signal is low-pass filtered and fed back to the laser in order to achieve locking (see figure 2.4).

The cavity is made from ultra-low expansion (ULE) glass, which is designed to have a low thermal expansion coefficient over a temperature range of 5 to 35°C. Finesse values in the order of 10^5 have been demonstrated [62]. Thereby the clock laser reaches high short term stability in the millihertz region [155], when the cavity is decoupled from environment. The cavity is located inside a thermal vacuum chamber, temperatures are thus efficiently kept constant. Vibration damping is achieved by implementing the thermal vacuum chamber which includes the reference cavity into a vibration insulated box that is damped by e.g. rubber foots.

Laser Doppler Cooling

All trap systems operate in vacuum in order not to suffer from collision of the particle(s) under test with surrounding gas atoms. Trapping is always combined with cooling, since a trap only works efficient if the trapped particles have a low temperature and thereby avoid frequency shifts.

The temperature of a particle in a gas is determined by its random motion. The higher the velocity of the particle, the higher is its temperature. If a photon hits the particle and is absorbed, the particle changes to a higher energy state (one electron changes into a higher electron shell). Through spontaneous emission, the particle sends out a photon and changes back to its original lower energy state. Irradiating a particle with a laser beam at suitable wavelength results in sequenced absorption and emission of photons. The momentum which is transferred to the particle during the absorption of a photon always points in the same direction thereby slowing down the atom in direction opposite to the beam of the cooling laser. The spontaneous emission of a photon does not show a preferred direction and the transferred momentum acts in random direction

each time a photon is emitted. Thereby the net momentum transferred to the particle due to spontaneous emission after many repeated photon emissions approaches zero [141].

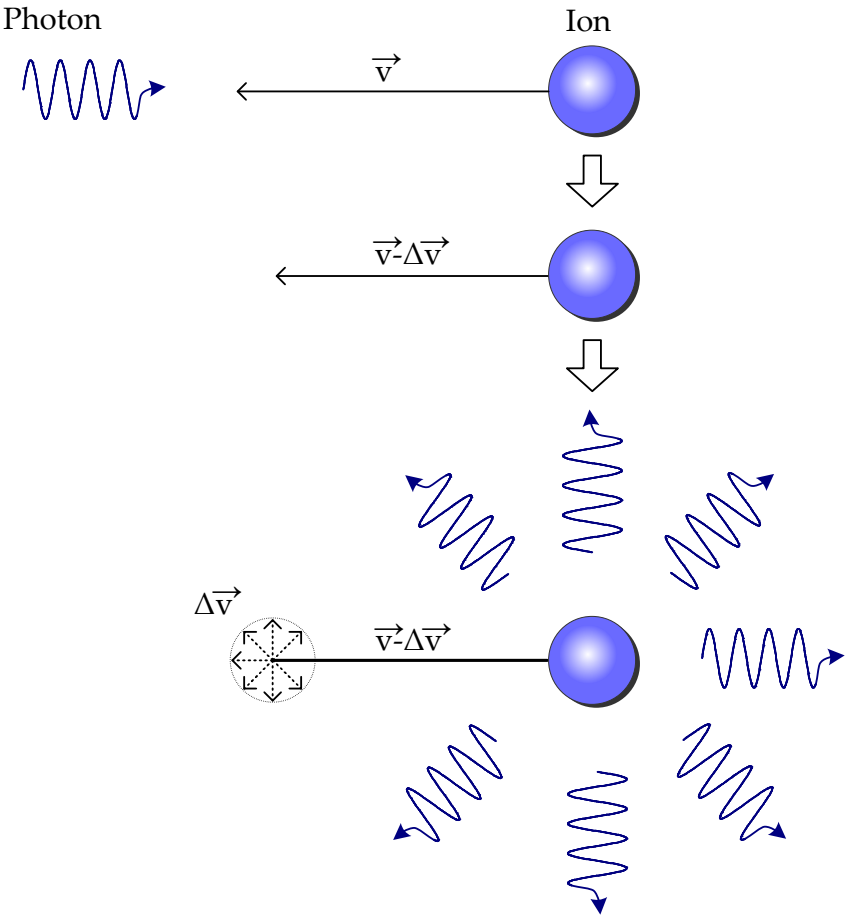

Fig. 2.5.: A photon of the cooling laser beam in x-direction is absorbed by the ion and emitted by spontaneous emission in random direction. Many absorption - spontaneous emission cycles result in a deceleration of the particle in x-direction.

The continuous process of absorbing photons in fixed direction and emitting photons in random direction reduces one component of the velocity vector of the particle, the one that points opposite to the cooling laser beam. If the frequency of the cooling laser matches the resonance frequency of the cooling transition of the particle, photons of the laser beam can be absorbed by the particle. Since the particle is in motion during the cooling process, its transition

frequency is shifted due to the Doppler effect [141]. In order to slow down a particle in the direction opposite to the laser beam, the laser frequency has to be shifted by the same amount thereby allowing the particle to absorb photons.

In figure 2.6 two counter propagating laser beams are shown that have a red-shifted frequency compared to the cooling transition frequency. Thereby the force which can be applied by one of the lasers to the particle is maximum when the particle moves towards the respective laser beam.

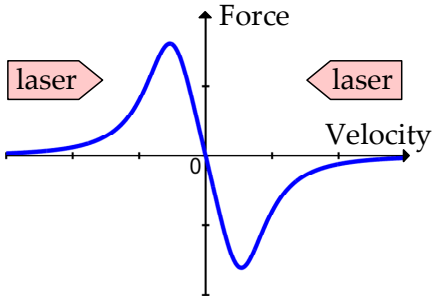

Fig. 2.6.: Laser cooling by two counter-propagating laser beams slows down one component of the velocity vector of the particle [94].

The use of e.g. three laser beams pointing in three spatial directions allows to slow down a particle in three dimensions. Since thermal atoms have a momentum that is orders of magnitude higher than that of a single photon, cooling of an atom requires many absorption - emission cycles.

Laser cooling requires particles that show a two level absorption meaning that the photon which is absorbed and the photon which is emitted have to have the same energy. The result is that the particle switches continuously between two states during the cooling process. If in real systems the particle changes by incident to a state where the cooling laser photons cannot be absorbed, an additional re-pumper laser is necessary. Re-pumping brings the particle back to its defined state thereby allowing the cooling process to be enabled again [62].

Trap techniques that use cooling lasers confine particles to less than one optical wavelength of the probe laser [112]. Thereby the absorption of the clock transition does not show any Doppler shifts in first order. The above described laser Doppler cooling is able to reach temperatures down to hundreds of micro Kelvin.

Single-Ion vs. Optical-Lattice Trap

Since ions are charged particles, they can be seen as having a "handle" where they can be held. This effect is used in Paul- or Penning-type ion traps, where a time-varying electric field (in the case of a Penning-type trap in combination with a homogeneous magnetic field) builds a potential that confines the ion locally [136]. In principle the same kind of trap can be used for several different ions, but amplitude and frequency of applied voltages (and of magnetic fields if applicable) have to be adapted according to mass and charge of the particle. Different designs have been developed reaching from complex three dimensional trap electrode-structures to simpler linear traps that allow easier particle loading and enhance laser cooling and measurement access [112].

In an optical-lattice clock, a magneto-optical trap is deployed. An optical lattice is created by a standing laser wave that creates potential wells and a spatial varying magnetic field. A Zeeman shift [49] in the atomic levels is thereby implemented that increases with the radial distance from the center of the trap. The idea of magnetic trapping is that in a magnetic field, an atom with a magnetic moment will have quantum states of which the magnetic or Zeeman energy increases with increasing field [141]. Thereby the cooling transition of the neutral atoms is shifted towards the frequency of the cooling laser, as an atom moves away from the center of the trap. In order to compensate for the interaction of the atoms with the lattice laser light, the lattice wavelength is tuned such that the introduced shift of both energy states of the reference transition is equal [138]. At this so called "magic wavelength" the reference transition of the atoms can be probed by the clock laser and the level shift due to the lattice laser interaction cancels out.

2.3. All Optical Atomic Clock based on an OFC

With the aid of an OFC, the accuracy of an optical frequency standard can phase-coherently be transferred to the rf domain. Therefore a setup according to figure 2.7 based on [33] can be used.

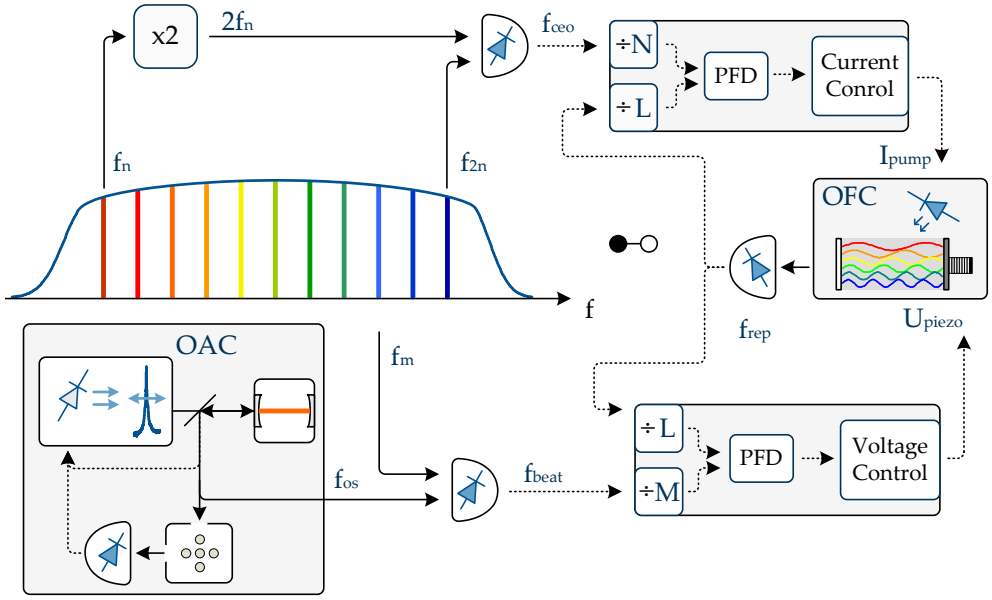

Fig. 2.7.: In an all-optical atomic clock, the repetition frequency of the OFC is locked to the frequency of the clock laser which itself is locked to the atomic reference frequency. Thereby the frequency of the optical standard is converted error-free to the rf output.

The frequency f_q of the comb line number q is according to equation 4.1 determined by $f_q = q \cdot f_{rep} + f_{ceo}$. Therein two frequencies, the repetition rate f_{rep} and the carrier envelope offset f_{ceo} indicate the spacing between and the common offset to all comb lines respectively (see sections 3.6 and 4.1 for details). According to section 4.5, the repetition rate f_{rep} is accessible by photo detection of the OFC output pulse train whereas the carrier envelope offset frequency f_{ceo} is obtained by f-2f interferometry. In order to achieve highest performance using an all-optical-clock approach, f_{rep} and f_{ceo} are locked to the optical standard f_{os} as explained hereinafter.

The frequency of the optical standard f_{os} is optically beated with one comb line f_m yielding

$$f_{beat} = f_{os} - f_m = f_{os} - m \cdot f_{rep} - f_{ceo}. \tag{2.2}$$

The OFC parameters f_{rep} and f_{ceo} are adjusted by variation of the piezo voltage U_{piezo} that holds one cavity end mirror and the pump laser diode control current I_{pump}. Two phase frequency detectors (PFD) combined with pre-scalers are implemented, that lock the phases of the two beat signals f_{ceo} and f_{beat} to the

phase of the repetition rate f_{rep} according to

$$f_{ceo} = \frac{N}{L} \cdot f_{rep} \tag{2.3}$$

and

$$f_{beat} = \frac{M}{L} \cdot f_{rep} \tag{2.4}$$

wherein L, M and N are integer values of the pre-scalers. Thereby the two control loops of figure 2.7 are closed. The control loops are similar to phase locked loops (PLL) whereas the laser oscillator acts as voltage controlled oscillator (VCO) which is implemented in a standard PLL [12].

Inserting equations 2.3 and 2.4 into equation 2.2 yields

$$f_{rep} = \frac{f_{os}}{m + M/L + N/L}. \tag{2.5}$$

Equation 2.5 shows that the frequency of the optical standard f_{os} is transferred to the electrical frequency f_{rep} by the setup shown in figure 2.7. The unknown value of the mode number m can be obtained by a procedure described in section 4.2. Thereby all frequencies of the all-optical OAC setup are referenced to f_{os} without the need of any external frequency reference. The repetition rate of the OFC serves as rf output signal of the OAC.

2.4. OFC Requirements

This section summarizes the main points which characterize an appropriate OFC that can be used in an OAC setup. Professor Schiller who is the project leader of the Space Optical Clocks (SOC) project [161] from the University Düsseldorf kindly provided these requirements. References for confirmation of feasibility of compliance when using a fiber-based laser is given for each point.

- **Stability requirements**
  Maximum carrier-envelope and repetition frequency cycle-slip rate of $2\pi \frac{rad}{1000s}$ (frequency deviation of 1 mHz) [174][108].
- **Line width of OFC lines**
  Maximum line width of a single frequency comb line $< 1\ Hz$, if the comb is phase stabilized to a clock laser with a line width of $< 1\ Hz$. [173].

- **Power per comb line**
  Minimum power of $0.1\,\mu W$ per comb line (only necessary for the measurement line and not for each line of the whole comb) [158].

- **Comb line spacing**
  High power per line results in improved beat signal between the clock laser and the comb. High repetition rates from 250 MHz to 1 GHz yield high line powers [172].

- **OFC frequency range**
  The optical frequency comb shall span a frequency range wherein the corresponding optical clock transitions lies. Today's laboratory OACs [62] work at different transition wavelengths: 698 nm (neutral Strontium), 689 nm (Sr+ Strontium ion), 871 nm (Yb+ Ytterbium ion), 1156 nm (neutral Ytterbium). Frequency conversion (see chapter 3) of the OFC output might be necessary to obtain comb lines near the actual clock laser frequency.

2.5. Optical Atomic Clocks for GNSS

Optical frequency measurement based on OFCs has application possibilities reaching from astronomical spectroscopy [169][105] over high accurate distance measurement [11][194] for e.g. satellite formation flights to clockwork operation inside an optical atomic clock [159][190][160]. The latter is the OFC application that is in view of this work and was examined in a DLR study carried out by Professor Hugentobler (see annex A.1).

Clocks play a fundamental role in global satellite navigation systems (GNSS) [120]. As GNSS is a one way measurement system based on light travel time measurement. The emitter on board the satellite and the receiver on ground have to be equipped with clocks. The key of GNSS is the fact that simultaneous measurements of signals from several satellites allow a synchronization of all clocks.

Satellites are equipped with atomic frequency standards. The second Galileo test satellite - GIOVE-B - launched in 2008 carries a passive hydrogen maser, currently the most stable clock in space [148]. Future satellites of the Galileo

and GPS systems could carry optical clocks with even higher performance in order to enable more accurate positioning.

In order to investigate the impact of clock modeling and prediction for ultra-stable clocks, simulations were performed in the frame of a DLR project (see annex A.1). The GNSS Bernese [9] simulator generated dual-frequency observations based on realistic orbit, troposphere delay and antenna errors. Different scenarios have been taken as basis for the simulations. A space segment of 32 satellites and a ground segment of 15 resp. 6 stations equipped with either Rubidium atomic frequency standards (RAFS), passive Hydrogen masers (PHM), active Hydrogen masers (AHM), space optical atomic clocks (SOAC) or ground optical atomic clocks (GOAC) were assumed. The accuracies and stabilities of RAFS, PHM and AHM were assumed to equal devices that are currently in use on board GPS and Galileo satellites. For SOAC and GOAC devices, expected values were taken from the Einstein Gravity Explorer proposal [160]. Simulation results for clock modeling and epoch-wise estimation are listed in table 2.1.

Tab. 2.1.: RMS of alongtrack orbit prediction errors of all satellites after 10 days for scenarios with modeled clocks and with epoch-wise estimated clock corrections.

Scenario **Space Clocks - Ground Clocks**	**Clocks modeled** **RMS error [m]**	**Clocks estimated epoch-wise** **RMS error [m]**
32 RAFS - 15 RAFS	780 m	110 m
32 PHM - 15 AHM	80 m	110 m
32 SOAC - 15 GOAC	40 m	110 m
32 SOAC - 6 GOAC	170 m	1200 m

While estimated GNSS orbits are independent from the performance of used clocks if the clocks are synchronized epoch-wise, clock modeling improves the orbit prediction if stable clocks such as Hydrogen masers and optical atomic clocks are used. Results are degraded, on the other hand, if the system is

operated with clocks that do not allow linear modeling over one day such as Rubidium clocks. A significant gain is achieved through clock modeling of stable clocks for a sparse tracking network, a result that may be of interest for the design of the ground system for future satellite navigation systems. With as few as six sensor stations similar results are obtained as for 15 sensor stations with epoch-wise clock estimation. This reduction of ground stations by a factor of more than two would significantly reduce efforts and costs for operators of a future GNSS based on optical atomic clocks.

3. Metrology Based on Linear and Nonlinear Optics

Within this chapter an introduction of the theory behind the linear and nonlinear optical effects that enable optical frequency comb generation and optical fiber sensing is given. The difference between linear and nonlinear optics is described in section 3.1 and optical non-linearities that arise from the interaction of high intense light and materials showing special properties are examined in sections 3.2 throughout 3.4. Constructive interference of monochromatic waves responsible for fiber Bragg grating based sensing and ultra-short pulse generation are theoretically introduced in sections 3.5 and 3.6 respectively.

3.1. Nonlinear vs. Linear Optics

Nonlinear optics is the field of optics in which the response of the polarization density $\vec{P}$ to the electric field $\vec{E}$ is nonlinear. This gives rise to several differences compared to linear optics [151][20]:

- The refractive index and other properties of optical media are dependent on light intensity.
- The principle of superposition is not valid for nonlinear optical media.
- The frequency of light changes when it passes a nonlinear optical medium.
- Interaction of two light beams is possible inside nonlinear optical media.

Nonlinear optics does only occur inside media, such media are therefore called nonlinear optical media and are characterized by a nonlinear relation between the polarization density $\vec{P}$ and the electric field $\vec{E}$.

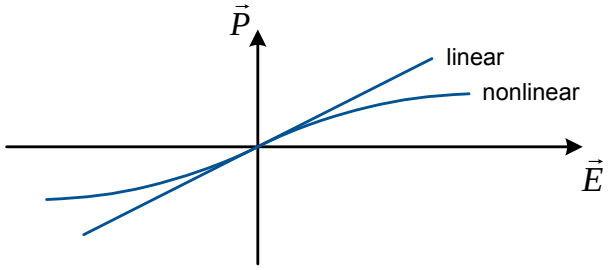

Fig. 3.1.: Relation between the polarization density $\vec{P}$ and the electric field $\vec{E}$ indicates linear or nonlinear media according to [156].

Electric field strengths of optical waves are usually small compared to interatomic fields even for focused laser beams. The relation between $\vec{P}$ and $\vec{E}$ is therefore linear. The function that relates $\vec{P}$ and $\vec{E}$ can be enhanced to a power series around $\vec{E} = \vec{0}$ [37]

$$\vec{P} = \varepsilon_0 \cdot \left(\chi^{(1)}\vec{E} + \chi^{(2)}\vec{E}^2 + \chi^{(3)}\vec{E}^3 + \cdots\right) \tag{3.1}$$

wherein χ is the magnetic susceptibility and ε_0 is the vacuum permittivity.

For convenience $\vec{P}$ is split up into linear and nonlinear terms

$$\vec{P} = \vec{P}_L + \vec{P}_{NL} \tag{3.2}$$

with

$$\vec{P}_L = \varepsilon_0 \chi^{(1)}\vec{E} \tag{3.3}$$

and

$$\vec{P}_{NL} = \varepsilon_0 \cdot \left(\chi^{(2)}\vec{E}^2 + \chi^{(3)}\vec{E}^3\right) \tag{3.4}$$

when only second- and third order nonlinearities are considered.

Assuming an isotropic and homogeneous medium, the basic wave equation for nonlinear media according to [156], [154] is

$$\nabla^2\vec{E} - \frac{\partial^2\vec{E}}{c^2\partial t^2} = \mu_0\frac{\partial^2\vec{P}_{NL}}{\partial t^2}. \tag{3.5}$$

wherein c and μ_0 are the speed of light and the vacuum permeability respectively. ∇ denotes the Nabla-operator [143]. Equation 3.5 differs from the wave equation of linear optics by the occurrence of the right hand side.

Using the Born approximation [154], the right hand side of equation 3.5 is considered as a light source S which is dependent on an incident electric field $\vec{E}_0$. The incident field in combination with the nonlinearity of the optical medium thereby creates the radiation source $S(\vec{E}_0)$ which itself emits a new electric field $\vec{E}_1$. Therefore a new radiation source $S(\vec{E}_1)$ is built up radiating a field $\vec{E}_2$, and so on. Using only the first step of iteration (so-called first Born approximation) is adequate when light intensity is weak and therefore the nonlinear processes are small. The first Born approximation is the simplified method used to describe second- and third-order nonlinear optics. Light which is propagating through a nonlinear medium as an electromagnetic wave having an electric field vector $\vec{E}_0$ creates a radiation source $S(\vec{E}_0)$ based on the nonlinear polarization density $\vec{P_{NL}}$. Since $S(\vec{E}_0)$ is a nonlinear function of $\vec{E}_0$, new frequencies are created. The scattered (radiated) light with an electric field vector $\vec{E}_1$ therefore comprises frequencies which were not included in the initial wave of $\vec{E}_0$. Several phenomena such as optical frequency conversion and wave mixing are the useful result of nonlinear optics.

3.2. Second-order Nonlinear Phenomena

Within this paragraph optical media which show second-order nonlinearity at the highest are considered. The nonlinear polarization density $\vec{P_{NL}}$ of equation 3.5 reduces to [20]

$$\vec{P}_{NL} = \varepsilon_0 \chi^{(2)} \vec{E}^2. \tag{3.6}$$

Second Harmonic Generation

The incident monochromatic wave $\vec{E}(t)$ is assumed to have a wavelength λ_0 in vacuum of

$$\lambda_0 = 2\pi c_0/\omega \tag{3.7}$$

wherein c_0 is the speed of light in vacuum and $\omega = 2\pi f$ is the angular frequency of the monochromatic wave. Assuming a complex amplitude $\vec{E}$ yields

$$\vec{E}(t) = \mathrm{Re}\{\vec{E}\exp(j\omega t)\} = {}^1\!/_2 \left[\vec{E}\exp(j\omega t) + \vec{E}^*\exp(-j\omega t)\right]. \tag{3.8}$$

This results in a nonlinear polarization density $\vec{P_{NL}}$ of

$$\begin{aligned}\vec{P}_{NL} &= \frac{\varepsilon_0\chi^{(2)}}{4}\left[\vec{E}\exp(j\omega t)+\vec{E}^*\exp(-j\omega t)\right]^2\\ \vec{P}_{NL} &= \frac{\varepsilon_0\chi^{(2)}}{4}\left[2\vec{E}^2+\vec{E}^2\exp(j2\omega t)+\left(\vec{E}^*\right)^2\exp(-j2\omega t)\right]\\ \vec{P}_{NL} &= \frac{\varepsilon_0\chi^{(2)}}{2}\left[\vec{E}^2+\mathrm{Re}\left\{\vec{E}^2\exp(j2\omega t)\right\}\right]. \end{aligned} \tag{3.9}$$

The source $\vec{S} = \mu_0\partial^2\vec{P}_{NL}/\partial t^2$ therefore radiates light at a frequency of 2ω with an amplitude of

$$\left|\vec{S}\right| = \frac{-2\omega^2\chi^{(2)}}{c_0^2}. \tag{3.10}$$

Common materials used as frequency doubling crystals are lithium niobate, potassium titanyl phosphate and beta barium borate [37]. Second harmonic generation is for example applied in f-2f interferometers (see section 4.5).

Three Wave Mixing

In the case that the electromagnetic field consists of two monochromatic waves at angular frequencies ω_1 and ω_2 ($\omega_1 > \omega_2$), $\vec{E}(t)$ results in

$$\vec{E}(t) = \mathrm{Re}\{\left|\vec{E}_1\right|\exp(j\omega_1 t)+\left|\vec{E}_2\right|\exp(j\omega_2 t)\}. \tag{3.11}$$

The nonlinear polarization component according to formula 3.6 yields

$$\vec{P}_{NL} = \varepsilon_0\chi^{(2)}1/2\begin{bmatrix} E_1E_1^*+E_2E_2^*\\ +\mathrm{Re}\{E_1^2\exp(j2\omega_1 t)\}\\ +\mathrm{Re}\{E_2^2\exp(j2\omega_2 t)\}\\ +2\,\mathrm{Re}\{E_1E_2\exp(j(\omega_1+\omega_2)t)\}\\ +2\,\mathrm{Re}\{E_1E_2^*\exp(j(\omega_1-\omega_2)t)\}\end{bmatrix} \tag{3.12}$$

$\vec{P}_{NL}$ contains five different components at frequencies 0, $2\omega_1$, $2\omega_2$, $(\omega_1+\omega_2)$ and $(\omega_1-\omega_2)$.

The radiation source $S(\vec{E})$ according to $\vec{P}_{NL}$ not necessarily radiates all of these frequencies. Only frequency components for which the additional phase

matching condition is satisfied are radiated by the source (see section 3.4). Phase matching can therefore be used to select the desired nonlinear effect, usually either sum $(\omega_1 + \omega_2)$ or difference $(\omega_1 - \omega_2)$ frequency generation. Sum and difference frequency generation is used for creation of wavelengths that cannot be emitted by laser sources directly.

3.3. Third-order Nonlinear Phenomena

Within this section optical nonlinear media that show third-order nonlinearity are observed. Their nonlinear behavior is described according to equation 3.4 by

$$\vec{P}_{NL} = \varepsilon_0 \cdot \chi^{(3)} \vec{E}^3. \tag{3.13}$$

The incident monochromatic wave $\vec{E}$ is assumed to be

$$\vec{E}(t) = \mathrm{Re}\{\vec{E}\exp(j\omega t)\} = {}^1\!/_2 \left[\vec{E}\exp(j\omega t) + \vec{E}^*\exp(-j\omega t)\right]. \tag{3.14}$$

This results in a nonlinear polarization density $\vec{P_{NL}}$ of

$$\vec{P}_{NL} = \frac{\varepsilon_0 \chi^{(3)}}{4}\left[\mathrm{Re}\left\{\vec{E}^3\exp(j3\omega t)\right\} + 3\left|\vec{E}\right|^2 \mathrm{Re}\left\{\vec{E}\exp(j\omega t)\right\}\right]. \tag{3.15}$$

The source S therefore radiates light with angular frequencies ω and 3ω.

Optical Kerr effect

Inserting the above calculate nonlinear polarization component $\vec{P_{NL}}(\omega)$ into formula 3.2 results in

$$\vec{P} = \left(\varepsilon_0 \cdot \chi^{(1)} + \frac{3\varepsilon_0\chi^{(3)}}{4}\left|\vec{E}\right|^2\right)\mathrm{Re}\left\{\vec{E}\exp(j\omega t)\right\} + \frac{\varepsilon_0\chi^{(3)}}{4}\mathrm{Re}\left\{\vec{E}^3\exp(j3\omega t)\right\}. \tag{3.16}$$

This can be interpreted as an expansion of the linear polarization component P_L by a delta-susceptibility $\Delta\chi$

$$\vec{P}_L = \varepsilon_0\left(\chi^{(1)} + \Delta\chi\right)\vec{E} \tag{3.17}$$

wherein

$$\Delta\chi = \frac{3\chi^{(3)}}{4}\left|\vec{E}\right|^2. \tag{3.18}$$

Since $n^2 = 1 + \chi$, a change of $\Delta\chi$ results in change of $\Delta n = \Delta\chi/2n$. Thus the change in the refractive index according to [154] is

$$\Delta n = \frac{3}{4}\frac{\chi^{(3)}}{n^2}\sqrt{\frac{\mu_0}{\varepsilon_0}} \cdot I. \tag{3.19}$$

The result is an overall refractive index which is dependent on the optical intensity I of the incident wave $\vec{E}$

$$n(I) = n + n_2 I \tag{3.20}$$

with

$$n_2 = \frac{3}{4}\frac{\chi^{(3)}}{n^2}\sqrt{\frac{\mu_0}{\varepsilon_0}}. \tag{3.21}$$

This self-induced effect is called optical Kerr effect and causes an intensity dependent phase velocity of the electromagnetic wave $\vec{E}(t)$. Optical media that exhibit third-order nonlinearity are therefore also called Kerr media.

Self-Phase Modulation

The linear phase shift φ of light when it travels through a medium of length l is $\varphi = -k \cdot l = -2\pi nl/\lambda_0$. Due to the optical Kerr effect (equation 3.20) an intensity dependent phase shift of

$$\Delta\varphi = -2\pi n_2 \frac{l}{\lambda_0} I \tag{3.22}$$

is introduced which adds up to the linear phase shift. Thereby high intense parts of a traveling pulse experience a higher phase shift than low intense parts. Due to this self-phase modulation (SPM) a chirped pulse with altered instantaneous frequencies as shown in figure 3.2 is generated [4].

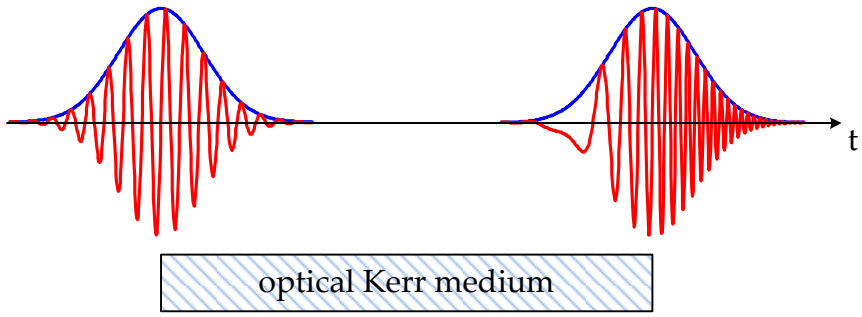

Fig. 3.2.: Self-phase modulation results in an intensity dependent phase shift. Thereby the instantaneous frequency is altered such that the leading and trailing edges are shifted to lower and higher frequencies respectively.

Self-Focusing

A laser beam with a Gaussian transversal intensity distribution that travels through a parallel plate consisting of a Kerr medium undergoes focusing. Due to SPM the high intense center part of the beam experiences an additional phase shift $\Delta\varphi$ according to equation 3.22. The parallel plate acts like a graded-index medium. Since the intensity magnitude of the laser beam decreases with the transversal distance from the center of the beam also the introduced phase shift reduces with increasing distance from the beam center. SPM in the Kerr medium thereby generates a converging lens for the transmission of the laser beam. Kerr lens mode-locking described in section 4.4.3 uses the self-focusing effect together with an aperture in order to build up an artificial saturable absorber.

3.4. Phase Matching

Phase matching refers to fixing the relative phase between two or more frequencies of light during propagation through a frequency conversion crystal [181]. Supposed that the two monochromatic waves $\vec{E}_1(\omega_1)$ and $\vec{E}_2(\omega_2)$, the sum-frequency component $\vec{P}_{NL}(\omega_1 + \omega_2)$ of equation 3.12 for example is only generated if its corresponding wavevector $\vec{k}_{sum}$ is the vectorial sum of both

wavevectors $\vec{k}_1$ and $\vec{k}_2$ of the incident waves [154]

$$\vec{k}_{sum} = \vec{k}_1 + \vec{k}_2. \tag{3.23}$$

Since all optical media exhibit chromatic dispersion (i.e. the refractive index is a function of frequency $n = n(\omega)$), equation 3.23 can be rewritten in dependence of the angular frequencies and the refractive indexes

$$\omega_{sum} n_{sum} \vec{u}_{sum} = \omega_1 n_1 \vec{u}_1 + \omega_2 n_2 \vec{u}_2. \tag{3.24}$$

wherein the unit vectors $\vec{u}_{sum}$, $\vec{u}_1$ and $\vec{u}_2$ point in the propagation direction of $\vec{E}_{sum}(\omega_{sum})$, $\vec{E}_1(\omega_1)$ and $\vec{E}_2(\omega_2)$ respectively. Only if this vectorial phase matching condition is satisfied along with the sum-frequency condition $\omega_{sum} = \omega_1 + \omega_2$ of equation 3.12, the source $S(\vec{E})$ emits light at wavelength ω_{sum}. The generated wave $\vec{E}_{sum}(\omega_{sum})$ then also interacts with the incident waves $\vec{E}_1(\omega_1)$ and $\vec{E}_2(\omega_2)$ thereby creating difference frequencies $\omega_2 = \omega_{sum} - \omega_1$ and $\omega_1 = \omega_{sum} - \omega_2$ because the phase matching condition is already fulfilled. These nonlinear processes of mutual interaction of three waves are subordinated to the concept of three-wave mixing. The nonlinear medium of second-order thus can be used to mix three waves and thereby enable sum-frequency and difference-frequency generation as described in section 3.2.

In order to achieve phase matching condition, two ways are used in practical work [156]:

- Adjustment of the angles of propagation vectors of incident waves. This method works with isotropic and anisotropic materials.
- Exploiting birefringence in anisotropic media allows to phase match incident waves by adjustment of their polarization directions with respect to the optical axis of the nonlinear medium.

If not the sum-frequency but another component of equation 3.12 shall be generated, phase relations have to be adapted accordingly.

Quasi-Phase Matching A phase mismatch $\Delta\vec{k} = \vec{k}_{sum} - (\vec{k}_1 + \vec{k}_2) \neq \vec{0}$ yields a reduced wave-mixing efficiency, because different positions within the interaction volume of the nonlinear medium radiate with different phases. Since

all radiation source points contribute to the common generated field, phase mismatch causes a reduced intensity of the radiated wave $\vec{E}_{sum}$.

In order to fulfill the phase matching constraints, the mismatch $\Delta\vec{k}$ can be compensated using a medium with position dependent nonlinearity [181]. Thereby a periodic phase direction change aligns the different distributed radiation elements. In case of a collinear propagation in x direction, a position dependent nonlinear coefficient $d(x)$ in the form of a harmonic function $d(x) = d_0 \exp(-jdx)$ would ideally eliminate the phase mismatch [154]. In praxis a simpler periodic pattern that alternates between to constant values $\chi^{(2)} = +\chi_0$ and $\chi^{(2)} = -\chi_0$, a phase grating, is used. The grating period Λ is chosen to

$$\Lambda = 2\pi m/\Delta k \tag{3.25}$$

wherein m is an integer multiplication factor for the grating period. The fabrication of such a periodic nonlinear structure can be achieved by applying an alternating electric field during crystal growth that alternates the resulting permanent electric polarization direction of the crystal [119]. Periodically-poled Lithium Niobate (PPLN) is one well known frequency conversion crystal that is built by this technique. The technique is called quasi-phase matching (QPM).

3.5. Interference of Multiple Waves with Equal Phase Differences

A monochromatic wave $\vec{E}_0$, that is reflected by a dielectric mirror (e.g. a SESAM or a fiber Bragg grating), is determined by the interference of M monochromatic waves $\vec{E}_1$, $\vec{E}_2$, $\vec{E}_3$, ... $\vec{E}_m$, ... $\vec{E}_M$ superimposing to the reflected wave $\vec{E}_r$:

$$\vec{E}_r(x) = \sum_{m=1}^{M} \vec{E}_m(x) \tag{3.26}$$

with

$$\vec{E}_m(x) = E_m \exp(j(kx - m\varphi)). \tag{3.27}$$

The wave number $k = \frac{2\pi n}{\lambda}$ is determined by the refractive index n and the wavelength λ. $m\varphi$ is the phase shift between the reflected wave $\vec{E}_m$ and the

initial wave $\vec{E}_0$. The phases of two waves reflected from two consecutive layers at normal incidence angle differ by a constant value $\varphi = 2kd$, wherein d is the distance between two consecutive layers.

The amplitudes E_m of the reflected fractions are assumed to successively decrease after each reflection at a grating or mirror layer:

$$E_m = \sum_{m=1}^{M} rE_0(1-r)^{m-1} \tag{3.28}$$

wherein a constant layer reflection coefficient r is assumed.

The reflected intensity $I = \left|\vec{E}_r\right|^2$ assuming a layer separation of d yields

$$I = \left\langle \left[\sum_{m=1}^{M} rE_0(1-r)^{m-1} \cdot \sin\left(\frac{2\pi n}{\lambda}(x - m \cdot 2d)\right)\right]^2 \right\rangle \tag{3.29}$$

wherein $\langle\cdot\rangle$ denotes time averaging.

Numerical simulation with an initial amplitude of $E_0 = 1$, a number of $M = 10^4$ layers, a reflection coefficient $r = 6 \cdot 10^{-5}$, a refractive index $n = 1.5$ and a layer separation of $d = 517\ nm$ yields an overall reflection shown in figure 3.3.

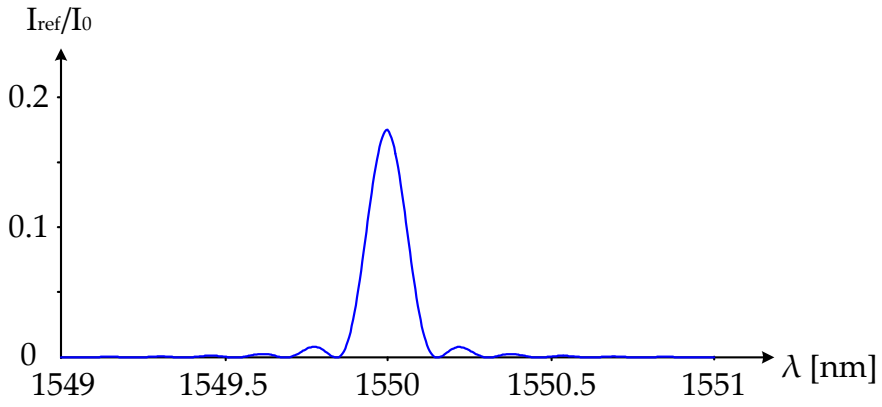

Fig. 3.3.: Simulation results of interference of 10^4 waves that have a constant phase difference. This could for example be the reflected intensity of a fiber Bragg grating.

The reflected intensity I reaches its maximum when the wavelength λ is an integer multiple of the grating period d. The simulation parameters have been chosen to match the values for fiber Bragg grating (FBG) sensors (see chapter 5.1).

3.6. Interference of Multiple Waves with Equally Spaced Frequencies

Ultrashort pulses are generally generated by the interference of a large number of monochromatic waves. Assuming on odd number of waves $M = 2L+1$, each with intensity I_0 and zero phase and spaced by a constant frequency interval of f_Δ centered around a frequency f_T results in a complex wavefunction

$$E(t) = \sqrt{I_0} \sum_{k=-L}^{L} \exp\left[j2\pi(f_T + kf_\Delta)t\right]. \tag{3.30}$$

The according intensity can be calculated as geometric series [154] to

$$I = I_0 \frac{\sin^2\left(M\pi t f_\Delta\right)}{\sin^2\left(\pi t f_\Delta\right)}. \tag{3.31}$$

Figure 3.4 shows simulation results of equations 3.30 (blue) and 3.31 (red) for a superposition of ten modes with equally spaced frequencies.

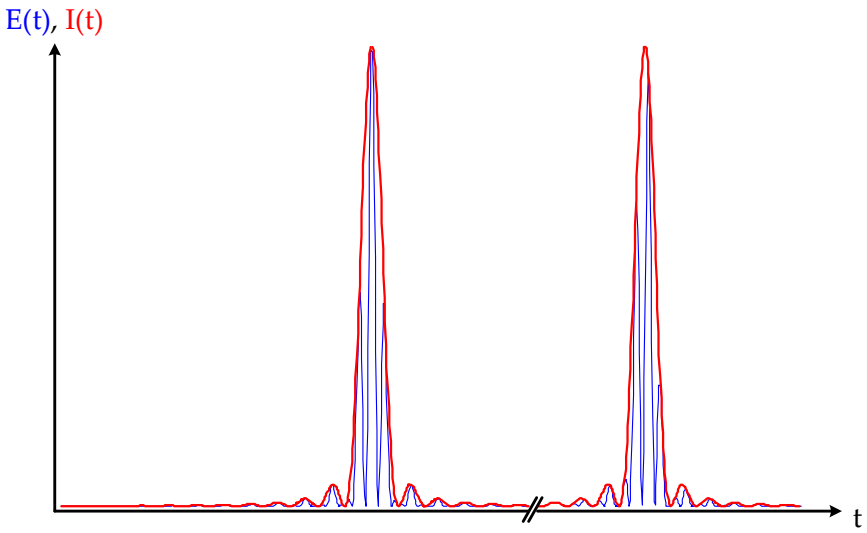

Fig. 3.4.: Simulation results of mode-locking. Ten frequencies that are equally spaced have been simulated. The blue graph shows the result of formula 3.30, the red graph shows the intensity envelope according to formula 3.31.

Figure 3.4 shows that consecutive pulses have equal envelopes but different carrier waves. This carrier-envelope offset (see also chapter 4.1) is due to the

physical effect that the carrier wave and the envelope propagate with different velocities v_p and v_g. Denoting the absolute value of the wave vector as k and the angular frequency as ω yields

$$v_P = \frac{\omega}{k} \quad \text{and} \quad v_g = \frac{\partial w}{\partial k} \tag{3.32}$$

Inserting v_p into v_g and using $k = 2\pi/\lambda$ results in

$$\begin{aligned} v_g &= \tfrac{\partial (k \cdot v_p)}{\partial k} = v_p + k \tfrac{\partial v_P}{\partial k}, \\ v_g &= v_P - \lambda \tfrac{\partial v_P}{\partial \lambda} = \tfrac{c}{n(\lambda)} - \lambda \cdot \tfrac{\partial}{\partial \lambda} \left(\tfrac{c}{n(\lambda)} \right), \\ v_g &= \tfrac{c}{(n(\lambda))^2} \left(n(\lambda) + \lambda \cdot \tfrac{\partial n(\lambda)}{\partial \lambda} \right). \end{aligned} \tag{3.33}$$

Insertion of the wavelength dependent refractive index $n(\lambda)$ according to the Sellmeier equation [29]

$$n(\lambda) = \left(1 + \sum_{i=1}^{3} \frac{A_i \lambda^2}{\lambda^2 - {B_i}^2} \right)^{1/2} \tag{3.34}$$

into formula 3.33 and calculation of the corresponding phase and group velocity of e.g. fused silica SiO_2 ($\mathrm{A_1} = 0.6962$, $\mathrm{A_2} = 0.4079$, $\mathrm{A_3} = 0.8975$, $\mathrm{B_1} = 68.4$ nm, $\mathrm{B_2} = 116.2$ nm, $\mathrm{B_3} = 9896.2$ nm) yields

$$\begin{aligned} v_P(1550nm) &= \tfrac{c}{n(1550nm)} \approx 2.08 \cdot 10^8 \tfrac{m}{s} \\ v_g(1550nm) &\approx 2.05 \cdot 10^8 \tfrac{m}{s}. \end{aligned} \tag{3.35}$$

This difference between the carrier and the envelope velocity results in a phase delay $\Delta\varphi_{ce}$ between carrier and envelope for each pulse, which can be seen in figure 3.4 [195]. $\Delta\varphi_{ce}$ results in an offset frequency f_{ceo} to the entire frequency comb [122][195]:

$$f_{ceo} = \frac{\Delta\varphi_{ce}}{2\pi} f_{rep} \tag{3.36}$$

wherein the repetition rate $f_{rep} = v_g/2L$ is determined by the group velocity v_g and the (linear-) resonator length L (see chapter 4.1) [146].

4. Optical Frequency Comb Technology

Within this chapter the technology of optical frequency combs (OFC) is introduced. The definition of an OFC is given in section 4.1. In section 4.2 the principle of optical frequency measurement by heterodyne beating is illustrated. Section 4.3 outlines the general architecture of an OFC. The femtosecond laser which is the core element of an OFC is explained in detail in section 4.4 and means of OFC stabilization are given in section 4.5.

4.1. Optical Frequency Comb Definition

The optical frequency comb (OFC) is an instrument to access the frequency of light in a direct way. The frequency of light is not accessible by means of electronic measurement devices. Beating of neighboring frequencies is a way to yield beat signals at lower frequencies. Prior to the invention of the OFC, frequency measurement chains [53][196] that operate several frequency transformation stages consecutively have been used to measure the frequency of lasers. In most cases, when high accuracy of frequency measurement is not required, optical spectrum analyzers are used to measure the wavelength of light instead of its frequency. The accuracy is limited by the wavelength measurement which is usually based on optical refraction in order to determine the angle of diffraction and calculate the wavelength thereof. The frequency is then calculated by $f = c/\lambda$. The invention of the OFC lead to a new approach allowing to determine the frequency of light directly without making a detour by wavelength measurement.

An OFC is named after its optical output spectrum which has a comb structure. Figure 4.1 shows a principle OFC in the spectral domain. It consists of equidistant frequencies separated by intervals of f_{rep}. All frequencies share a common

offset f_{ceo} [195].

The frequency of every "tooth" of the OFC and thereby the entire comb is characterized by only two parameters: the frequency spacing f_{rep}, and the offset frequency f_{ceo}. By stabilization of f_{ceo} and f_{rep}, the frequencies of all comb lines are kept constant and the frequency of the q-th tooth is determined by:

$$f_q = q \cdot f_{rep} + f_{ceo} \tag{4.1}$$

wherein q is the consecutive number of the comb line, also called mode number.

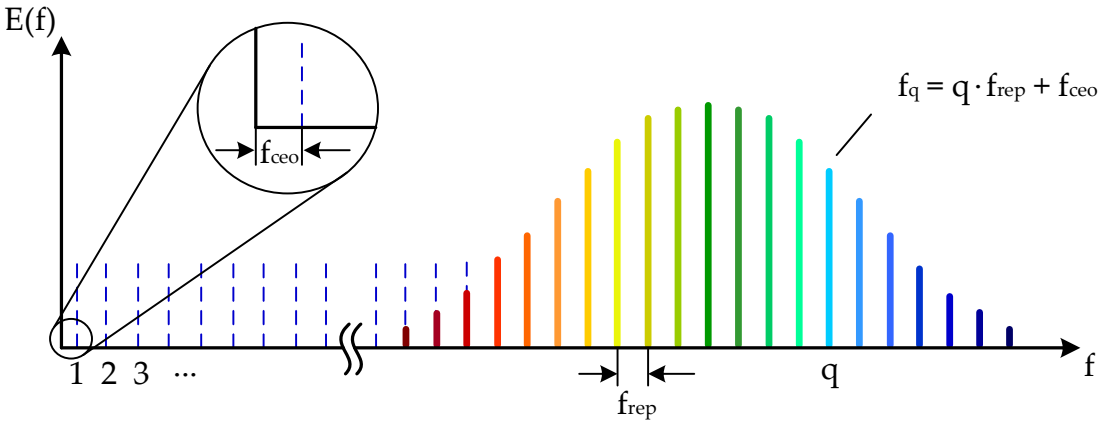

Fig. 4.1.: An optical frequency comb is an optical spectrum consisting of a series of equidistantly spaced laser lines. The extrapolation of the mode frequencies towards lower values shows the offset frequency f_{ceo} which can be interpreted as an offset of the entire spectrum.

4.2. OFC based Optical Frequency Measurement

An absolute frequency of a coherent and thereby narrow-band light source like a laser can be determined by heterodyne detection [185][195]. Optical heterodyne detection is based on the superposition of two monochromatic waves of different frequencies on a photo detector. The intensity I of a monochromatic wave equals the absolute square of its complex electromagnetic field $\underline{E}$: $I = |\underline{E}|^2$. The complex representation of the electric field, according to the definition in chapter 3, is

$$\underline{E}(t) = \underline{E}_0 \cdot e^{j\omega t}. \tag{4.2}$$

Heterodyning of two monochromatic waves $\underline{E}_1$ and $\underline{E}_2$ with angular frequencies ω_1 and ω_2 yields

$$\underline{E}(t) = \underline{E}_1(t) + \underline{E}_2(t) = \underline{E}_{01} \cdot e^{j\omega_1 t} + \underline{E}_{02} \cdot e^{j\omega_2 t}. \tag{4.3}$$

The intensity of the heterodyne signal results in

$$\underline{I}(t) = \underline{E}_{01}^2 + \underline{E}_{02}^2 + 2\underline{E}_{01}\underline{E}_{02} \cos\left[(\omega_1 - \omega_2)\, t\right]. \tag{4.4}$$

Thereby a time-varying signal with a beat frequency of $\omega_{beat} = |\omega_1 - \omega_2|$ is generated. The closer the two superimposed frequencies are, the lower becomes the beat frequency. This low frequent intensity oscillation can be detected by a photo detector and measured by electronic means. Figure 4.2 illustrates the generation of a low frequency beat signal between an unknown laser frequency and an OFC.

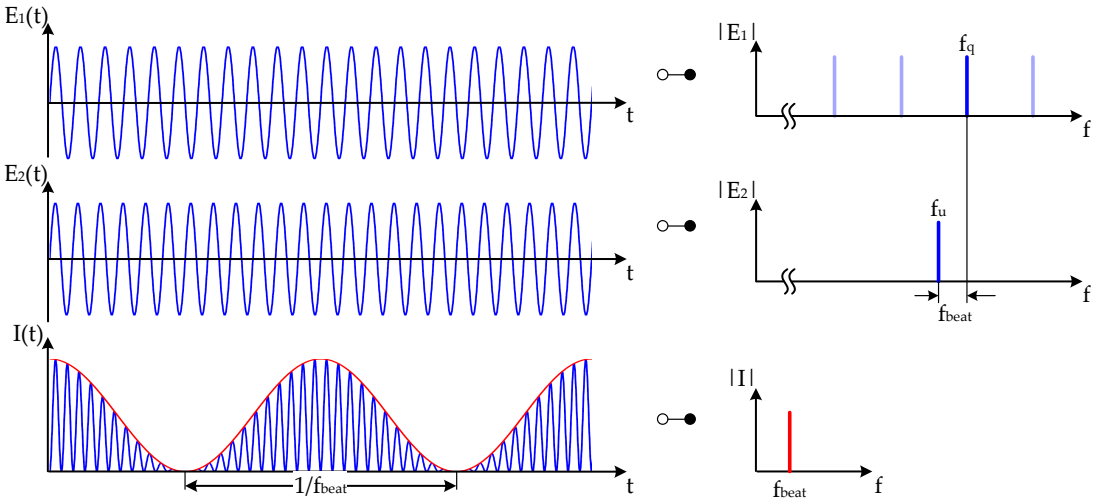

Fig. 4.2.: Optical frequency measurement based on heterodyne beating of two laser beams with nearby frequencies. An OFC provides many equidistant spectral lines and is therefore also called an optical ruler. Beating of an unknown frequency f_u with one of the comb lines f_q results in an intensity modulation at a frequency f_{beat} that is measurable by a photo detector.

An unknown frequency f_u within the output spectrum of the OFC beats with nearby frequencies of the comb spectrum. The presence of more than one reference frequency (comb line) induces superposition of different beat notes (see

also figure 4.15. Because of this, the electric signal at the detector output is low pass filtered in order to select the beat note with lowest frequency. The lowest beat frequency always results from heterodyning of the unknown frequency f_u with the closest comb line f_q. Therefore this fundamental beat frequency f_{beat}, generated when beating f_u with the entire OFC output spectrum, has a maximum value of $f_{rep}/2$. Implementation of an electric low-pass filter with a cut-off frequency of $f_{rep}/2$ therefore eliminates all higher frequencies and only f_{beat} appears at the low pass filter output. Thereby the unknown frequency f_u can be calculated by

$$f_{beat} = |f_u - f_q| \Rightarrow f_u = f_q \pm f_{beat} = (q \cdot f_{rep} + f_{ceo}) \pm f_{beat}. \tag{4.5}$$

Upon f_{rep} and f_{ceo} have been stabilized, only the integer mode number q has to be identified in order to calculate f_u. Measuring the wavelength λ_u of the unknown signal with a high resolution optical spectrum analyzer would for example allow to estimate the unknown frequency to $f_u \approx c/\lambda_u$. Assuming a measurement accuracy of $\Delta\lambda = 0.1\ pm$ at an absolute wavelength of $\lambda_u = 1550\ nm$ would result in a frequency uncertainty of approximately $\Delta f = 12.5\ MHz$. The mode number n of an OFC with a repetition rate of 100 MHz could therefore be determined with high certainty except f_{beat} lies between 44 MHz and 56 MHz.

Furthermore it has to be identified if f_u is lower or higher than f_q, i.e. if + or - sign applies in formula 4.5. Therefore the repetition rate could for example be increased. If f_{beat} rises, the unknown frequency is lower than the comb line ($f_u < f_q$) and a minus sign is chosen in formula 4.5. Otherwise, when f_{beat} decreases, f_u is higher than f_q and the plus sign is chosen. Varying the repetition rate of the OFC can also by applied as method for identification of the mode number q of the comb line that beats, as explained in [197].

4.3. Optical Frequency Comb Architecture

In chapter 3.6 it is shown that an optical frequency comb consists of a high number of monochromatic waves at different frequencies with common phases. In the time domain this is achieved by mode-locked lasers that emit a train of ultra-short pulses. Theoretically a pulse train in the spectral domain and a

pulse train in the time domain build a Fourier transformation pair [126]. As mentioned in chapter 4.1, the two parameters f_{rep} and f_{ceo} have to be stabilized in order to stabilize the entire OFC. This stabilization requires equipment additional to the pulsed laser. Several different technologies are available to establish a stable optical frequency comb, a general architecture of an OFC is introduced in this chapter. Figure 4.3 shows the principle configuration of an OFC.

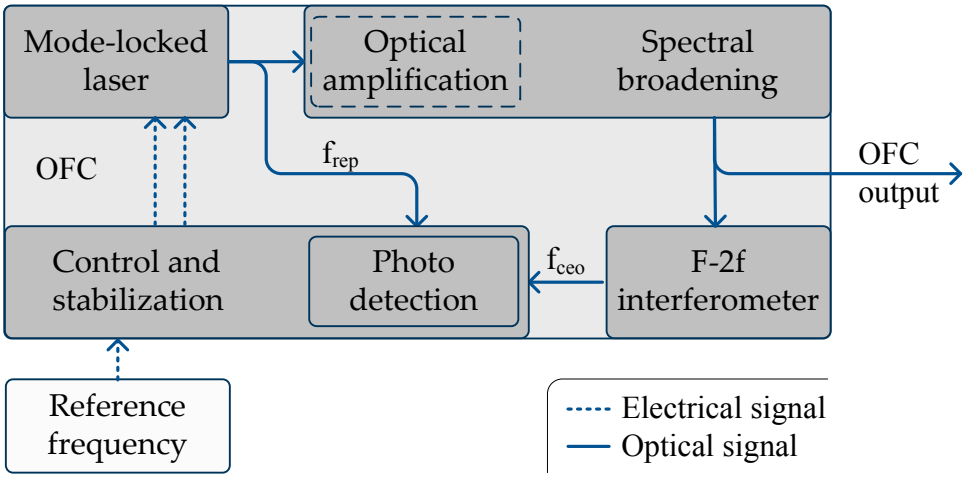

Fig. 4.3.: Configuration of a stabilized optical frequency comb (OFC). The photodetector and the external reference signal are needed to stabilize the comb.

The four main subsystems of an OFC are:

- **Mode-locked laser**
  Pulses with femtosecond durations are generated by a mode-locked laser (chapter 4.4). The train of ultra-short output pulses at a repetition rate f_{rep} in the time domain corresponds to a spectrum of equidistant lines separated by f_{rep} and sharing a common offset f_{ceo} (see also chapter 3.6). Thereby the comb structure of optical frequencies is generated.

- **Spectral broadening unit**
  In order to achieve an octave spanning spectrum, which is required for stabilization of the OFC, the output spectrum of the comb is broadened by guiding the laser light through a highly nonlinear fiber (chapter 4.5).

The nonlinear effects that cause the spectral broadening are intensity dependent (see also chapter 3), therefore optical amplification [3] is usually required prior to coupling the laser light into the nonlinear fiber. Rare-earth doped fiber amplifiers are a common type of optical amplifiers.

- **Control and stabilization unit**
  Stabilization of the OFC requires control of the two parameters f_{rep} and f_{ceo} (chapter 4.5). Therefore these frequencies are phase locked to an external reference frequency that is provided to the OFC. Whereas f_{rep} can be measured by means of monitoring the output frequency of the pulse train with a photo detector, the offset frequency f_{ceo} is only accessible using a f-2f interferometer. Control inputs of the mode-locked laser allow adjusting of the frequencies f_{rep} and f_{ceo}.

- **F-2f interferometer**
  The carrier-envelope offset frequency f_{ceo} is an offset common to all frequencies of the OFC (see also chapter 4.1). A f-2f interferometer beats the low frequency part of the optical output spectrum of the OFC with its high frequency part. This heterodyne beating enables the measurement of f_{ceo} using a photo detector.

The mode-locked laser generates the OFC and is therefore also called optical frequency comb generator (OFCG). All additional equipment is only necessary to stabilize the two OFC parameters f_{rep} and f_{ceo}.

In case that the OFC is used as clockwork in an optical atomic clock (OAC), the clock laser delivers all reference frequencies. Repetition rate and carrier envelope offset are thereby locked to the optical standard (see figure 2.7).

4.4. Femtosecond Laser - The OFC Generator

In chapter 3.6 it is shown that a comb-like structure in the spectral domain (see also figure 4.1) corresponds to a superposition of a high number of waves with equally spaced frequencies in the time-domain. All superimposed waves have a constant phase relation to each other (in section 3.6 zero phase was assumed). Waves that have constant phase relation are also called phase-locked or mode-

locked. Superposition or constructive interference of multiple phase-locked waves results in ultra-short pulses with time durations in the order of less than hundred femtoseconds. In mode-locked lasers one pulse is reflected back and forth in the cavity with a round-trip time of T_{rep}. Every time it hits the output coupler, a part of the pulse is emitted thereby generating a pulse train with a repetition rate of $f_{rep} = 1/T_{rep}$ at the output of the laser.

Figure 4.4 shows the principle setup of a mode-locked femtosecond laser. The gain medium within the cavity is optically pumped in order to reach inversion level. A pulse generator, i.e. a technique or mechanism that achieves mode-locking, generates an ultra-short pulse that generates an output pulse train. The cavity length L determines the round-trip time of the pulse and thereby the repetition rate of the laser:

$$f_{rep} = \frac{1}{T_{rep}} = \frac{v_g}{k \cdot L} \tag{4.6}$$

wherein v_g stands for the group velocity of the laser pulse (see also section 3.6). The integer value k parameterizes f_{rep} according to the laser configuration: $k = 2$ for linear and $k = 1$ for ring resonators.

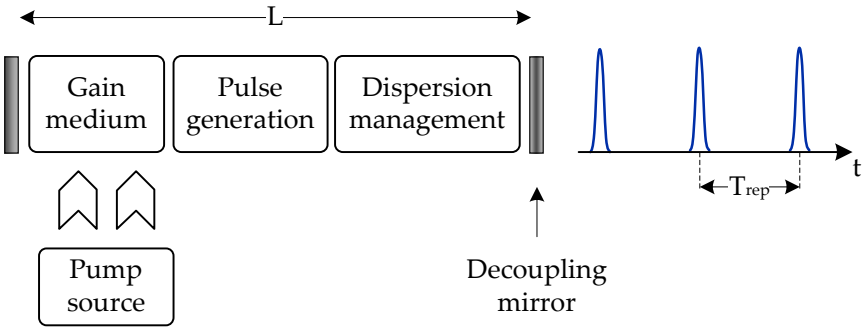

Fig. 4.4.: Principle design of a mode-locked femtosecond laser. A pulse generator produces a high intense optical pulse which in turn generates an output pulse train with a period of T_{rep}.

Since the pulse is generated by mode-locking of multiple modes at different frequencies, dispersion compensation is necessary in order to prevent the pulse from dissolving. Within a laser, standing waves i.e. monochromatic waves at resonance frequencies of the cavity are generated[89][42]. Assuming a cavity

according to figure 4.4, the longitudinal resonator modes are separated by constant frequency differences called the free spectral range FSR.

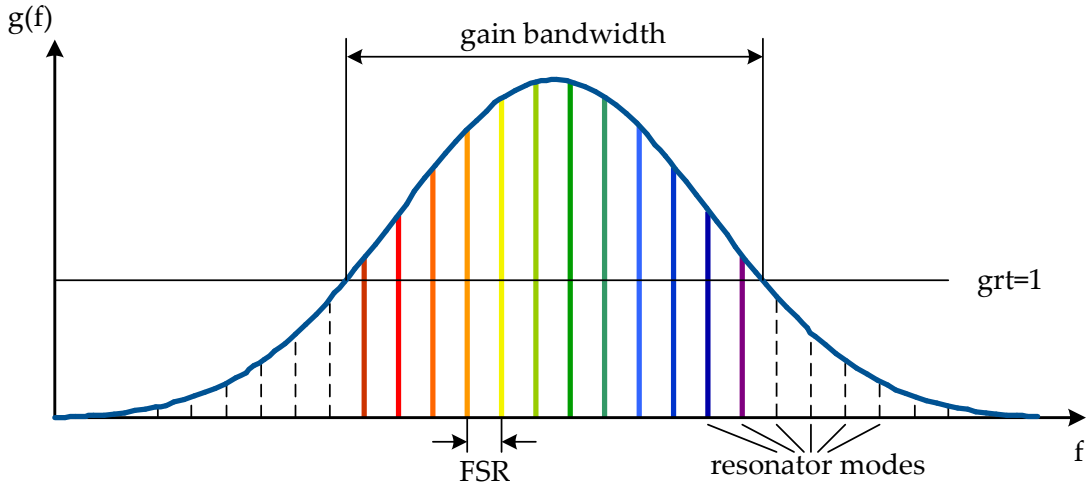

Fig. 4.5.: Longitudinal modes of a resonator are separated by FSR. Resonator modes within the gain bandwidth of the laser are amplified and create standing waves.

4.4.1. Dispersion Compensation

Group velocity dispersion (GVD) appears in dispersive media due to the wavelength dependent phase velocity [4]. Ultra-short pulse generation by mode-locking is based on a fixed phase relation between all resonator modes (see chapter 3.6). Since all optical media exhibit wavelength dependent dispersion, different modes within the resonator circulate with different phase velocities. Dispersion thereby tends to broaden the pulse [4]. Unless a mechanism inside the resonator achieves constant overall dispersion for all modes during one round-trip, a constant phase relation between all modes cannot be sustained. Figure 4.6 illustrates broadening of a laser pulse due to wavelength dependent dispersion.

In order to compensate for normal dispersion, anomalous dispersion has to be inserted in the resonator. This can be achieved by various methods including chirped mirrors and arrayed waveguide gratings (AWG) [170]. In free-space, a prism pair [6] configuration according to figure 4.7-a can be used. Thereby

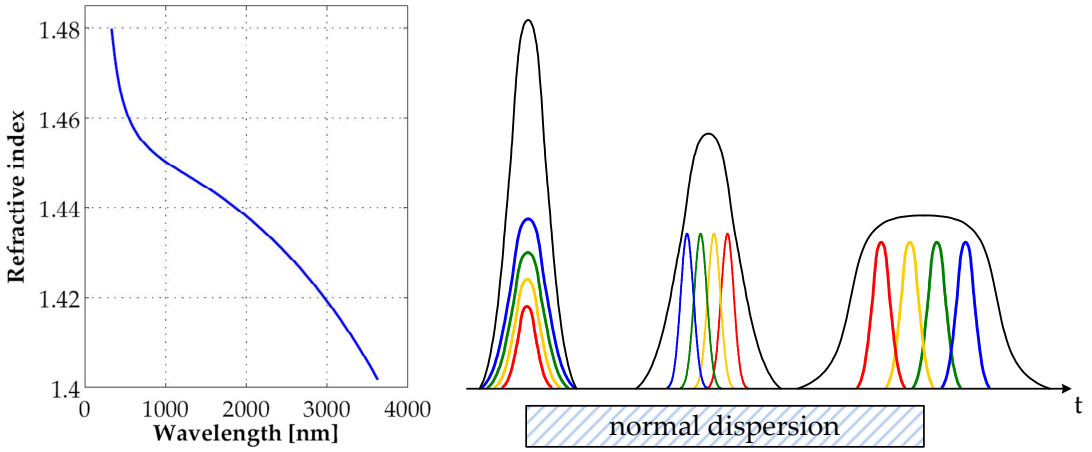

Fig. 4.6.: Normal (chromatic) dispersion of fused silica according to the Sellmeier equation [154]. Dispersion results in dissolving of a pulse that is built-up by locking of different modes.

the optical path length for wavelengths that experience a lower refractive index is increased in order to compensate dispersion differences. By adjustment of the two prisms, the optical path lengths can be adapted such that the overall dispersion for one round-trip of the pulse is equal for all modes.

For fiber lasers one solution is to use chirped gratings as one end mirror of the resonator (see figure 4.7-b). This technique is also used in fiber based data communication where the dispersion of optical fibers has to be compensated [103]. Applying a temperature gradient on the chirped grating allows to adjust the dispersion.

Another way of dispersion compensation in mode-locked fiber lasers is to split the resonator and splicing in dispersion compensating fibers that exhibit anomalous dispersion. Adjustment of the lengths of normal and anomalous fibers allows to achieve the desired overall zero dispersion [154].

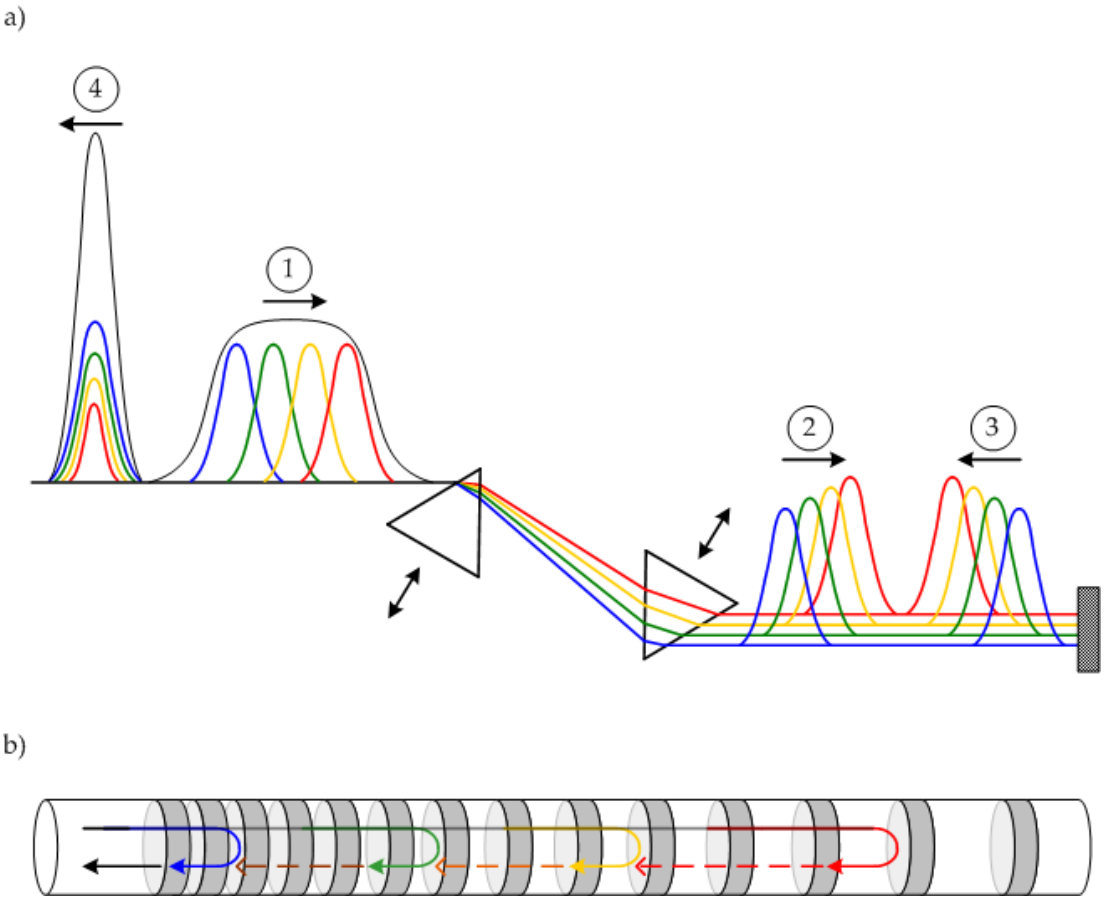

Fig. 4.7.: Dispersion compensation is achieved by elongation of the optical path length for light at wavelengths that experience a low refractive index. a)In free-space one common method is to use a prism pair; b) in fiber optics a chirped grating or mirror can be used.

Soliton Pulses

A medium which is both, nonlinear and dispersive can be used to compress, stretch or maintain a pulse, depending on the magnitudes of GVD and SPM. The maintenance of a pulse is desired in mode-locked lasers in order to reach stable operation. Solitons are single wave packets that propagate through a medium without altering their width or shape [3]. Solitons occur when self phase modulation compensates group velocity dispersion (see also section 3.3). In fiber lasers, balancing of GVD and SPM can be achieved by splicing together a sequence of fibers exhibiting alternating negative GVD and positive SPM yielding quasi-soliton operation. Gain provided by the amplifying region

compensates attenuation so that the pulse maintains its peak intensity and thereby its soliton properties.

4.4.2. Saturable Absorption and Mode-Locking

Saturable absorption is a property of an optical component or system: When the intensity of light, that incidents in the saturable absorber material, increases, the absorption decreases. In other words, a saturable absorber is a device of which the absorption is inversely proportional to the light intensity [3]. Saturable absorption can be deployed in transmission or in reflection. The latter one yields saturable absorber mirrors (SAM).

Mode-locking is a technique to coherently lock the phases of many modes (see figure 4.8) inside a laser resonator [151][195]. Saturable absorbers modulate the loss for light that travels inside the cavity. Modes that show phase-locked condition superimpose to high intense pulses (see also chapter 3.6) which results in higher saturation of the saturable absorber than continuous-wave light. During each round-trip the number of modes that contribute to the pulse increases due to stimulated emission that occurs when the resonator losses are reduced by high intensity. In the steady-state all resonator modes that lie within the gain bandwidth of the gain medium are phase-locked because the highest intensity corresponding to the lowest resonator loss is achieved.

It can be distinguished between "natural" and "artificial" saturable absorbers:

- **Natural Saturable Absorbers**
  Natural saturable absorbers are devices that exhibit the above described material property. Semiconductor saturable absorber mirrors (SESAM) are such devices (see figure [4.11]). In steady state, the leading edge of circulating pulse saturates the absorber layer and thereby reduces the loss for the high intense part of the pulse. Low intense background light that hits the absorber experiences high losses because the absorber is not saturated by low intensity.
- **Artificial Saturable Absorbers**
  Saturable absorption can also be achieved by configurations of optical components inside the laser cavity that exploit nonlinear behavior. These

configurations achieve high losses for low intense and low losses for high intense light not by properties of a material but by the characteristic of the configuration. The non-linear Kerr-effect (see also section 3.3) thereby enables artificial saturable absorption. Examples outlined in the following are Kerr-lens and non-linear polarization-rotation mode-locking.

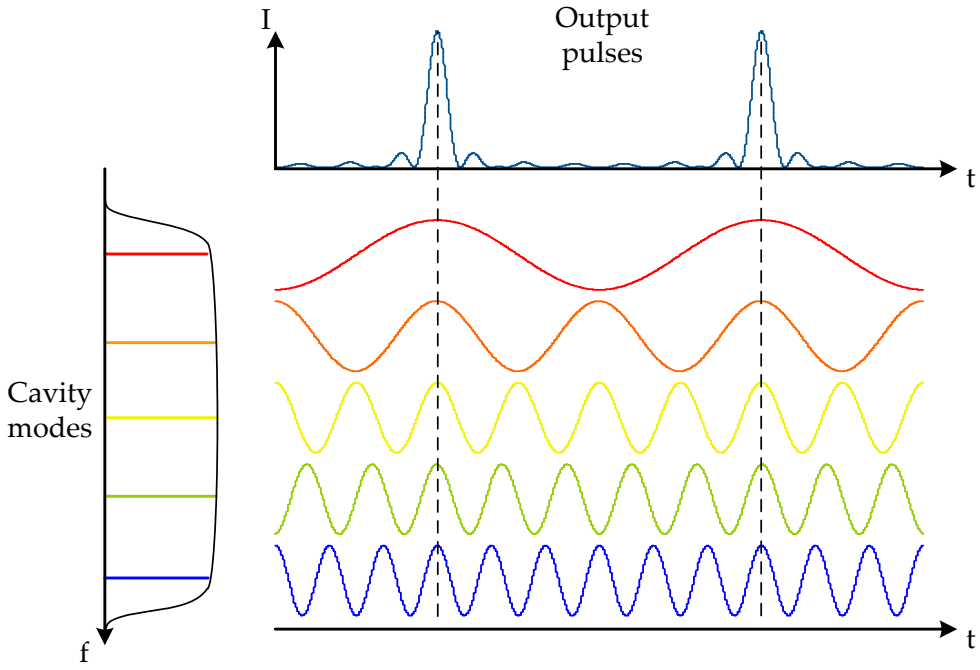

Fig. 4.8.: Mode-locking of resonator modes yields high intensity output pulses.

Lasers that start its mode-locking automatically after the pump power has been switched on are called self-starting. A SESAM for example is a passive device that supports self-starting once a spontaneous fluctuation of laser power has overcome the saturation level [184]. A description on how an ultra-short pulse develops after switching on the pump power is given in [166]. Self-starting is required for a laser to be used in a space-borne application.

4.4.3. Mode-Locking Examples

Three common types of passive mode-locking [134] that have been investigated in this work are outlined in this section.

Kerr Lens Mode-locking

Kerr-Lens mode-locking (KLM) is a passive mode-locking technique typical for bulk solid state lasers like Titanium doped Sapphire lasers. KLM relies on the nonlinear optical Kerr-effect in which the refractive index of a material changes according to the optical intensity [151]. A medium which presents nonlinear optical characteristics, usually the gain material itself, acts as a lens with a focal length inversely proportional to the intensity (see also chapter 3.3).

The Kerr-effect causes a reduction of the beam size for high intense light and, in combination with an aperture, is used as artificial saturable absorber: The high intense center of the laser pulse experiences a higher refractive index than the low intense edges; thereby the pulse is refracted towards its center. The transversal intensity distribution of a Gaussian beam results in a refractive index change across the beam profile. By implementation of an aperture behind the crystal, the high intense center of the beam passes whereas the low intense and continuous-wave light is blocked as illustrated in figure 4.9. The very fast response and the simple configuration of this artificial saturable absorber are the advantages of the KLM method.

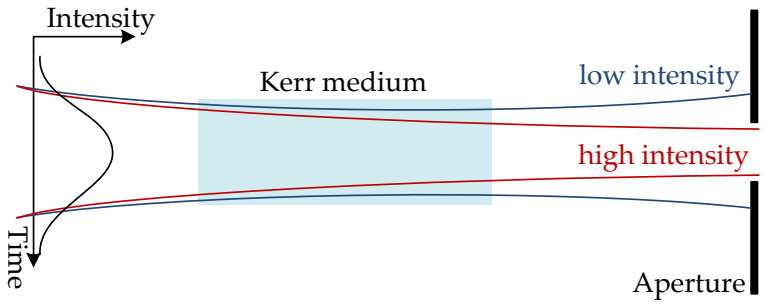

Fig. 4.9.: The refractive index at the edge is lower than in the center of the beam. The Kerr-medium thereby acts as a lens which results in attenuation of low intense light.

Nonlinear Polarization-Rotation Mode-Locking

Nonlinear polarization-rotation mode-locking (NLPR) relies on the intensity dependent rotation of an elliptical polarization state in an optical fiber [176][34].

Mode-locking based on polarization rotation uses the effect that high intense optical pulses change their polarization state when propagating through an optical fiber. This is due to combined effects of self-phase modulation and birefringence of an (non-polarization maintaining) optical fiber [2][91]. Figure 4.10 illustrates the principle of this kind of artificial saturable absorber.

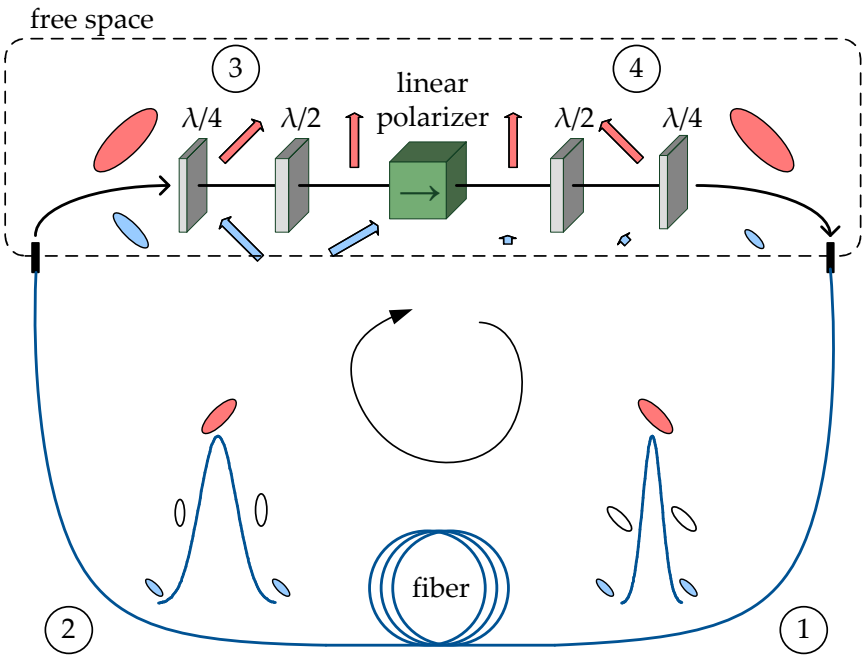

Fig. 4.10.: Schematic of passive mode-locked by NLPR. The polarization angle changes with regard to light intensity. Only the high intense part of the pulse (red) is transmitted, low intense light (blue) is blocked.

Light that leaves the free space part of the ring oscillator (position 1) shows an elliptic polarization state at a certain angle. Propagation of the pulse through the optical fiber alters the polarization rotation. High intensity (red) thereby results in a higher degree of rotation than low intensity (blue). At the beginning of the free space part (position 3), elliptically polarized light passes the $\lambda/4$ wave plate and is converted to linearly polarized light. The $\lambda/2$ wave plate rotates the linear polarization state. Assumed that the initial angle of the input elliptic polarization was at a certain angle, the linearly polarized light passes the polarizer almost loss-less. Since the elliptic polarization angle is dependent on intensity, the wave plates at position 3 can be adjusted such that the high intense light (red) passes where else low intense light (blue)is blocked by the

polarizer. Polarization controlling at position 4 finally adjusts the polarization state in a way that equilibrium is achieved i.e. that the elliptic polarization states at all positions remain constant after each round-trip.

Consequently this setup of waveplates and polarizer allows only the high intense central part of the pulse to pass and blocks low intensity light. Thereby an artificial saturable absorber is implemented.

SESAM Soliton Mode-Locking

A saturable absorber inside the resonator modulates the losses inside the cavity [109]. In a semiconductor saturable absorber mirrors (SESAM) saturable absorption is a material property. This is due to the fact that in the absorber layer of the SESAM (a quantum well [193]) the atoms in the ground state are excited into a higher energy state by incident photons. If the rate of photons is high enough, the ground state depletes and thereby the absorption saturates [86]. In SESAM devices a Bragg mirror is implemented beneath the absorber whereby incident high intense light that passes the absorption layer is reflected. Figure 4.11 illustrates the basic structure of a SESAM.

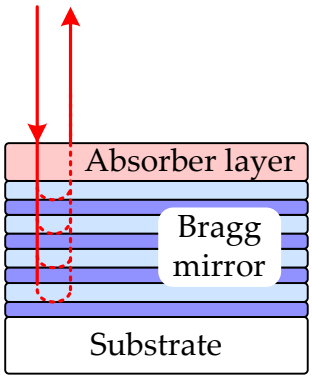

Fig. 4.11.: The absorber layer of the SESAM enables saturable absorption. The successive Bragg mirror reflects high intense light that has achieved saturation of the absorber layer.

The SESAM is placed at the end of the laser cavity and works like a fast optical switch typically on picosecond time scale [96]. It only reflects the laser light

when saturated with high peak powers. Amplified spontaneous emission (ASE) [151] is completely absorbed each round trip because it does not reach the saturation level of the SESAM. After formation of a stable laser pulse (steady-state) the SESAM efficiently absorbs residual laser light and therefore stabilizes the circulating laser pulse. Working with a so-called "slow" SESAM with switching times on the picosecond time scale requires that the laser operates in the soliton regime for generating femtosecond laser pulses [135]. In this mode, the laser pulse is not formed by the SESAM itself but by soliton pulse formation (see also section 4.4.1).

4.5. OFC Stabilization

In order to stablize the two parameters of an optical frequency comb, the repetition rate f_{rep} and the carrier-envelope offset frequency f_{ceo}, two control loops have to be implemented [195]. The actual values of both frequencies are compared to set values derived from the external reference frequency source (see figure 4.3). This is achieved by phase detectors that are known from phase-locked loops (PLL) [12]. Contrary to standard PLLs, a deviation of the actual frequency from the set frequency does not adjust a voltage controlled oscillator. The OFCG itself is adjusted such that the frequency (either f_{rep} or f_{ceo}) matches the corresponding set value.

The repetition rate f_{rep} is adjusted by changing the resonator length. The output pulse train of the laser is measured with a photo detector in order to obtain the actual value of f_{rep}. Comparing the actual value of f_{rep} with the set value given by a reference frequency generates an error signal. This signal stabilizes the voltage of a piezo stack which holds one end mirror of the resonator.

Stabilization of the carrier-envelope frequency f_{ceo} is more complex than repetition rate control. Since f_{ceo} is not directly measurable, a special type of interferometer is required to access f_{ceo}. This f-2f interferometer requires an octave spanning spectrum [8] where the highest frequency of the spectrum is twice the lowest frequency. In order to obtain an octave spanning spectrum, a spectral broadening unit as illustrated in figure 4.3 is required.

Spectral Broadening

In fiber based OFCGs, the output spectrum of the laser does usually not provide an octave spanning spectrum. Therefore a highly nonlinear fiber (HNLF) is used to broaden the spectrum [144]. HNLFs are fibers that support guiding of high intensities, thereby enabling nonlinearities like self-phase modulation that broaden the spectrum [124][27]. Tapered fibers [153] with reduced core diameter or photonic-crystal fibers (also called micro-structured or holey fibers) [152], that enable bandgap engineering, are two examples of HNLFs. At the left-hand side of figure 4.12, the structure of a photonic crystal fiber is shown. Air holes in the fiber round a solid core change the mean refractive index and thereby act like a fiber cladding. Changing the structure of the holes allows to design the properties of the fiber.

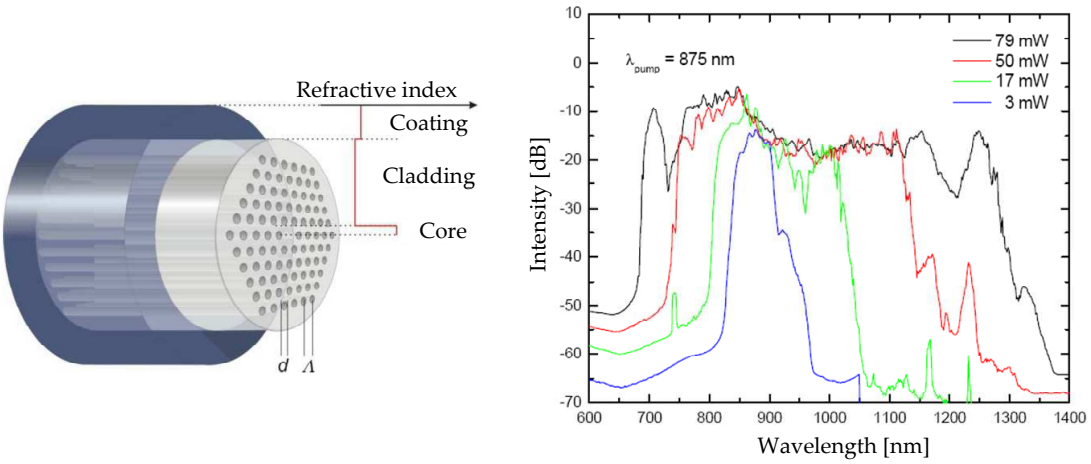

Fig. 4.12.: A photonic crystal fiber achieves spectral broadening dependent on the intensity of the pulses [142].

The output spectrum in dependence of the power of the input pulses is shown at the right hand side of figure 4.12, demonstrating that the nonlinear effects that broaden the spectrum strongly depend on light intensity .

Figure 4.13 shows a measurement of the broadened output spectrum of an OFCG dependent on the relative position of two prisms of a subsequent prims compensator (see also figure 4.7). At a prism position of approximately $3 \cdot 10^4 \mu m$, an octave spanning spectrum is achieved. Intensities up to -30 dBm at 1000 nm

and 2000 nm allow f-2f interferometry and thereby comb stabilization (see also section 4.5).

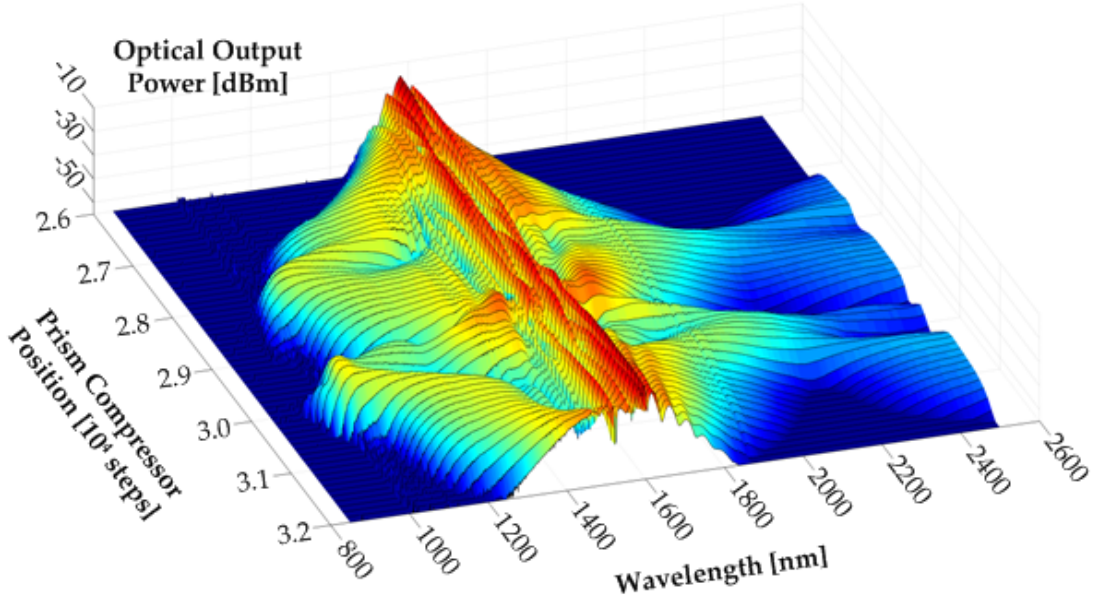

Fig. 4.13.: Output spectrum of an OFCG. By prism positioning, the dispersion is adjusted such that an octave broad spectrum is achieved from 1000 nm to 2000 nm.

F-2f Interferometer

As shown in chapters 4.1 and 4.3, carrier-envelope offset frequency stabilization is required in order to stabilize the OFC. Therefore a control loop is necessary that holds f_{ceo} constant by measuring it and adjusting the current of the laser pump diode [177]. For measurement of f_{ceo}, an f to 2f (also f-2f) interferometer is required. Figure 4.14 illustrates the principle of f_{ceo} measurement using an f-2f interferometer. F-2f interferometry requires an octave spanning optical output spectrum. Other schemes that do not require an octave spanning spectrum (e.g. 2f-3f interferometry [79] [104]) have also been developed but are more complex and therefore not taken into account for space applications. Alternative CEO stabilization approaches use acousto-optic modulators for shifting the entire output of the OFC by f_{ceo} [90].

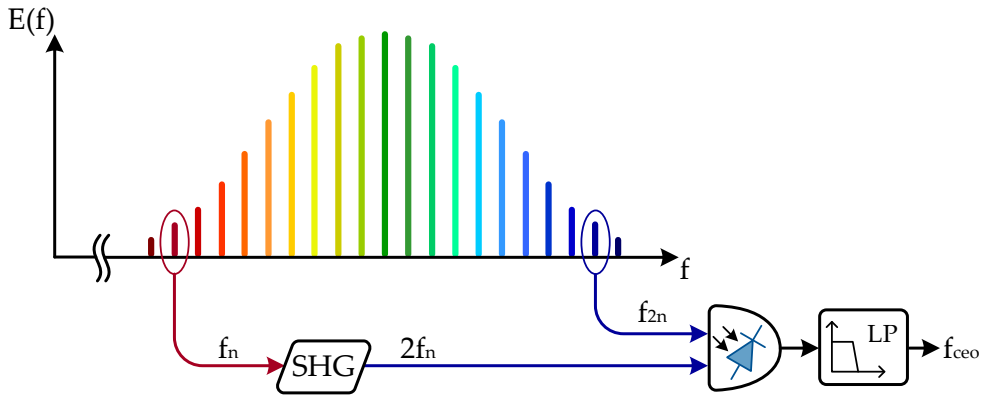

Fig. 4.14.: Principle operation of an f-2f interferometer. Light at the low frequency end of an octave spanning spectrum is frequency doubled by second-harmonic generation (SHG) and brought to interference with high frequency light for f_{ceo} determination.

In order to achieve f_{ceo}, a low frequency mode f_n of the optical spectrum (shown in dark red in figure 4.14) is frequency doubled by second-harmonic generation according to section 3.2. Thereto the light is focused into a frequency doubling crystal. By the second-order non-linearity of the material, light at frequency $2f_n$ is generated (see also section 3.2).

Periodically poled Lithium Niobat (PPLN) for example is a highly efficient medium for frequency doubling. In the conversion process, a single input photon is split into two new generated photons. The restriction for photon frequencies is that the overall energy is maintained. New photon frequencies are generated when the waves are phase matched. Changing the temperature of the crystal varies the phase matching condition. This alters the periodicity of the poling in the crystal and thereby allows tuning of the generated photon frequency [181].

Assuming that the red mode in figure 4.14 has a frequency of $f_n = n \cdot f_{rep} + f_{ceo}$ according to formula 4.1, the frequency doubling results in:

$$2f_n = 2(n \cdot f_{rep} + f_{ceo}) = 2n \cdot f_{rep} + 2f_{ceo}. \tag{4.7}$$

The frequency doubled light is then brought to interference with a high frequency mode $f_{2n} = 2n \cdot f_{rep} + f_{ceo}$ from the other end of the octave spanning

spectrum (shown in dark blue in figure 4.14). Thereby a beat node at the difference frequency f_{beat} is generated according to formula 4.4. This frequency beating yields the carrier-envelope offset frequency:

$$f_{beat} = |2f_n - f_{2n}| = f_{ceo}. \tag{4.8}$$

The frequency beating (compare also to chapter 4.2) leads to an intensity modulation with a frequency of f_{ceo} that is measured by a photo detector. Usually not only single modes but several modes from both ends of the spectrum are brought to interference at the photo detector in order to enhance the SNR (see figure 4.15). Corresponding frequencies of high and low modes of the spectrum (f_n and f_{2n}, f_{n+1} and $f_{2(n+1)}$, f_{n+2} and $f_{2(n+2)}$, ...) interfere with each other and generate the same beat frequency f_{ceo}. But also all adjacent frequencies beat

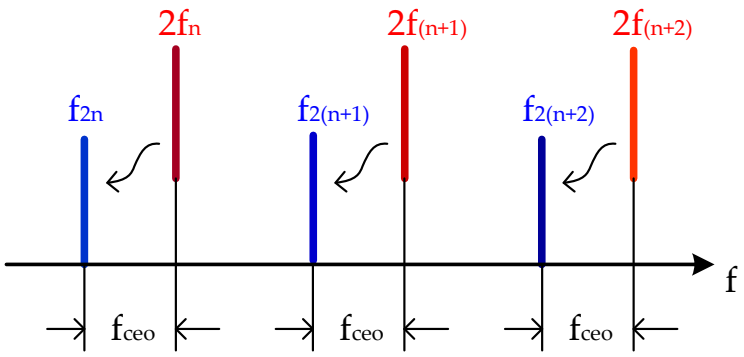

Fig. 4.15.: Beating of frequency-doubled modes (red) from the low frequency end of the spectrum with modes from the high frequency end of the spectrum (blue) yields the carrier-offset frequency f_{ceo}.

with each other (e.g. $2f_n$ and $f_{2(n+1)}$) and yield parasitic frequencies different from f_{ceo}. These beat frequencies are always higher than f_{ceo} since the modes are separated wider (see also formula 4.5). An electric low pass filter with a cut-off frequency of $f_{rep}/2$ at the output of the photo detector eliminates these unwanted higher harmonics.

Because the OFCG produces laser pulses, the spectral lines are only available within the pulse duration. Therefore the beat-note measurement as described above basically equals sampling of the carrier-envelope frequency f_{ceo} with the

repetition rate f_{rep} as shown in figure 4.16. Due to the fact that f_{ceo} always lies between two adjacent modes (see figure 4.15), the maximum frequency of the carrier-envelope frequency is half the repetition rate:

$$f_{ceo,max} = \frac{f_{rep}}{2}. \tag{4.9}$$

Thereby the Nyquist-Shannon theorem for sampling [126] is fulfilled innately.

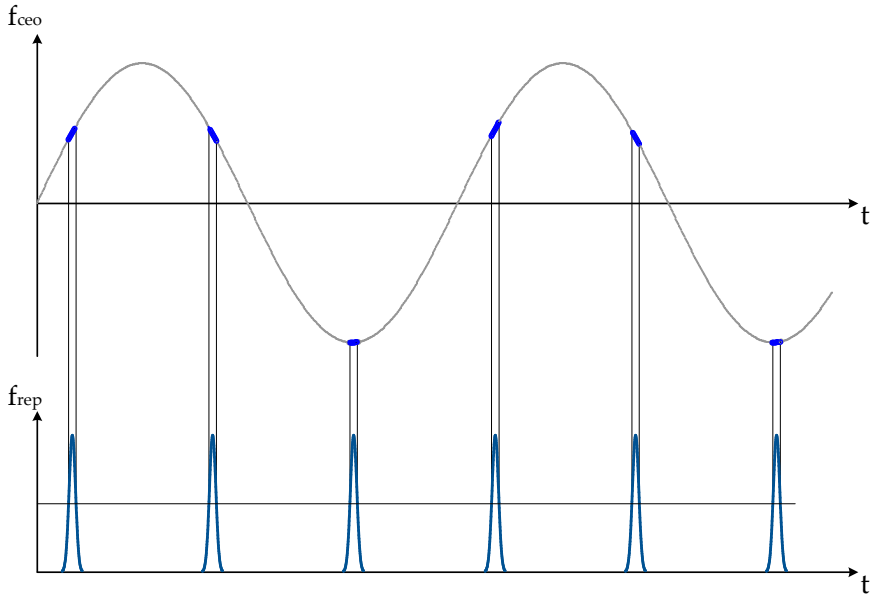

Fig. 4.16.: Measurement of the carrier-envelope offset basically results in sampling of f_{ceo} with f_{rep}, whereby the sampling theorem is always fulfilled.

5. Optical Fiber Sensing Technology

Within this chapter sensing based on optical fiber sensors is outlined. Fiber Bragg gratings (FBG) and their use as sensors are explained in sections 5.1 and 5.2. Three different schemes for FBG sensor interrogation are introduced in section 5.3. The tunable modulated-grating laser diode used for the interrogation system developed in this work (see chapter 8) is described in section 5.4.

5.1. Fiber Bragg Grating Sensors

The most common types of optical fiber based sensors are fiber Bragg gratings (FBG) named after the British physicist William Lawrence Bragg. Fiber Bragg gratings are in principle dielectric filters that are based on multiple layers of alternating high and low refractive indexes. At every optical transition between two consecutive layers light is reflected partially. When the optical path length differences of the reflections are integer multiples of the wavelength, constructive interference occurs. Thereby fiber Bragg gratings are wavelength sensitive filters that, by variation of layer thicknesses, can be designed to reflect one specific wavelength and transmit all others. Figure 5.1 illustrates the principle structure of a FBG sensor, theoretical aspects are explained in section 3.6.

In optical fibers the Bragg grating can be generated by inscription with an UV laser [128][56][77]. The laser beam is split into two arms and is brought to interference at the position of the fiber core. Thereby the core melts at places where high intense constructive interference occurs. This changes the refractive index of the core and results in a periodic grating with a period Λ. Light at the so called Bragg wavelength λ_B that matches the Bragg condition

$$\lambda_B = 2n_{eff}\Lambda \tag{5.1}$$

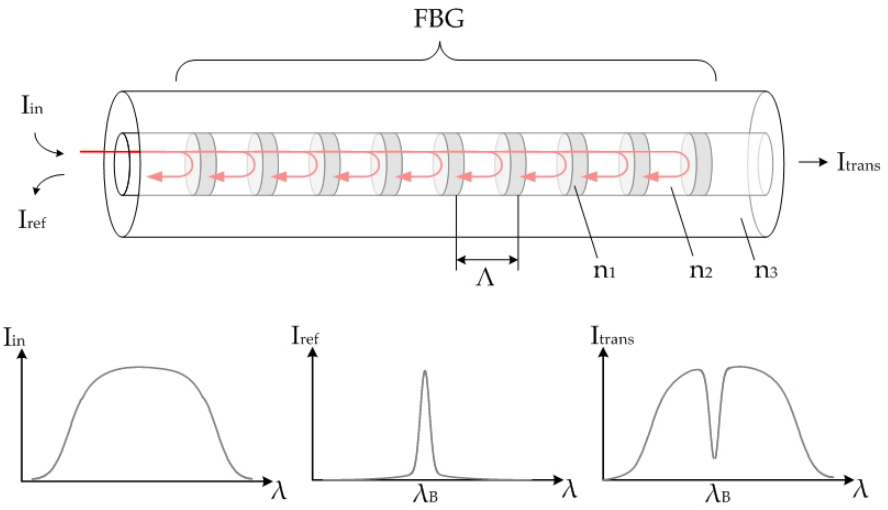

Fig. 5.1.: Principle structure of a fiber Bragg grating (FBG). Partially transmitting mirrors act as interference filter and thereby implement a wavelength dependent behavior. Light that matches the Bragg wavelength λ_B is reflected by the FBG.

is partially reflected by the FBG, all other wavelengths are transmitted unaltered. $n_{eff} = \frac{n_1+n_2}{2}$ thereby stands for the effective refractive index of the fiber core, the mean value of the fiber core refractive indexes n_1 and n_2 according to figure 5.1.

Fiber Optic Sensing (FOS) provides a promising alternative to electric sensing technologies. FOS instrumentation has the potential to improve conventional instrumentation in several ways. The design and development activities and subsequent demonstration within this work prove the potential of FOS instrumentation in terms of:

- Capability of sensor distribution. Sensor arrays, i.e. several sensors with different grating periods Λ inscribed along one single fiber can be used. The sensors reflect light at different wavelengths. Fiber optic sensing thereby can be regarded as a sensor bus comparable to electric sensor buses like one-wire or I^2C. Figure 5.2 illustrates the possibility of sensor distribution.

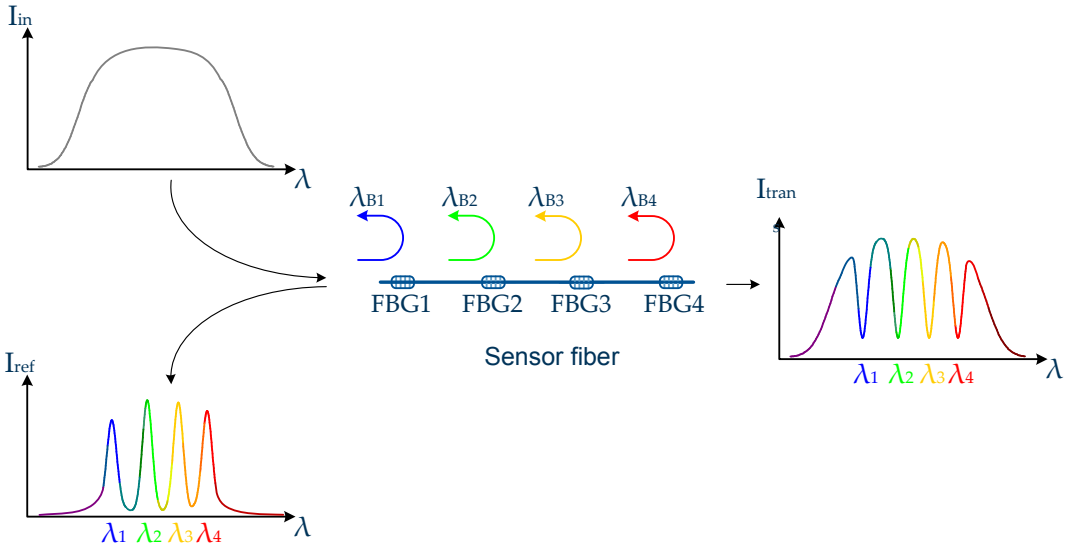

Fig. 5.2.: FBGs with different grating periods that are inscribed in an optical fiber serially implement a sensor array.

- Insensitivity to electromagnetic (em) interferences. FBG sensors are read-out optically; the measurement accuracy is not influenced by any em fields near the sensor location. Furthermore, FOS does not induce any interferences that could harm surrounding equipment wherefore em shielding can be omitted.
- Reduced mass and volume of the sensor network. One single optical fiber is required that guides the light in both directions, from interrogator to the sensors and back. Optical sensor fibers can be embedded in composite materials which reduces the effort for assembly and integration because sensor mounting is not required.

5.2. FBG Measurement Principle

The wavelength itself which is reflected by a FBG does not allow any conclusion about the current measurement parameter (e.g. temperature or strain) at the location of the sensor. Everything that influences the Bragg condition (formula 5.1) results in a change of the wavelength that is reflected. This wavelength shift is evaluated by the interrogator and allows to conclude about the relative

change in magnitude of the actual measurand.

FBGs are sensitive to temperature and strain variations because both measurand changes influence the geometry of the FBG structure and the refractive indexes of the core material. According to [87], the spectral sensitivities of a FBG sensor at a design wavelength λ_B to applied strain ε and temperature T amount to

$$\frac{\delta\lambda_B}{\delta\varepsilon} = 0,78 \cdot 10^{-6}\frac{\lambda_B}{\mu\varepsilon} \tag{5.2}$$

respectively

$$\frac{\delta\lambda_B}{\delta T} = 6,67 \cdot 10^{-6}\frac{\lambda_B}{K}. \tag{5.3}$$

In the case of a design wavelength of $\lambda_B = 1550\,nm$, the overall wavelength shift $\Delta\lambda_B$ of a FBG due to applied strain $\Delta\varepsilon$ and temperature ΔT results in

$$\Delta\lambda_B = 1,21\frac{pm}{\mu\varepsilon} \cdot \Delta\varepsilon + 10,34\frac{pm}{K} \cdot \Delta T. \tag{5.4}$$

One issue that arises from the sensitivity of a FBG sensor given by formula 5.4 is that it cannot be distinguished if the wavelength shift arises from a temperature or a strain variation. Similar to electric strain sensors, the sensor transducer needs to be designed such that unambiguity of measurement results is given. Transducers for temperature sensors for example have to decouple the sensor from structural strain.

5.3. FBG Interrogation Systems

Three well known configurations of fiber optic interrogation systems are considered: Spectrometer based systems utilize a broadband illumination and detect the actual wavelength of the sensor by wavelength division multiplexing. A second principle uses edge filters to "cut" the sensor response and determine the

measurement value by the ratio of the two resulting intensity signals. Systems based on tunable lasers, which are in the focus of this work, sweep through the wavelength spectrum and evaluate the magnitudes of the reflected (or transmitted) intensities.

Spectrometer Based Systems

This design uses a broadband light source such as super-luminescent diodes (SLD) in order to illuminate FBG sensors within the sensor channels. The different sensors reflect light at different wavelengths. The reflected signals are spectrally encoded by a spectrometer consisting of e.g. a diffraction grating and a CCD sensor. An evaluation electronics evaluates the CCD image whereof the mean wavelengths of all sensors are determined by centroid algorithms.

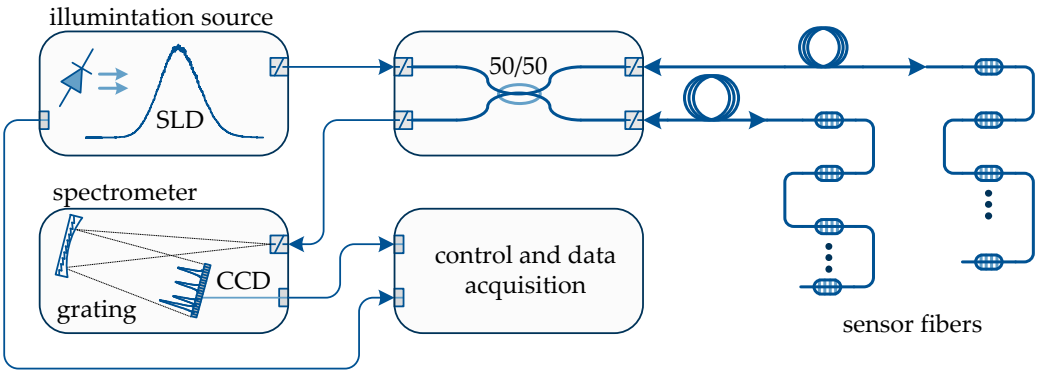

Fig. 5.3.: Spectrometer based interrogation unit. A broadband light source illuminates the FBG sensors, the responses are determined by a spectrometer.

This kind of interrogator concept has the highest maturity; all components are commercially available as standard industrial components. By enhanced design of the spectrometer, multiple sensor channels can be imaged to a two-dimensional CCD array in parallel. Because the wavelength of the signal is transformed in one spatial dimension, different channels can be mapped to different lines of the CCD array.

Edge Filter Based Systems

This design uses a broadband unpolarized light source (e.g. [127]) in order

to illuminate the sensor fiber. Light that is reflected by a FBG sensor enters two optical edge-filters that overlap spectrally. The two resulting intensities are measured with photo detectors at the edge-filter outputs. Determining the intensity ratio of the photo currents yields the spectral response of the FBG sensor.

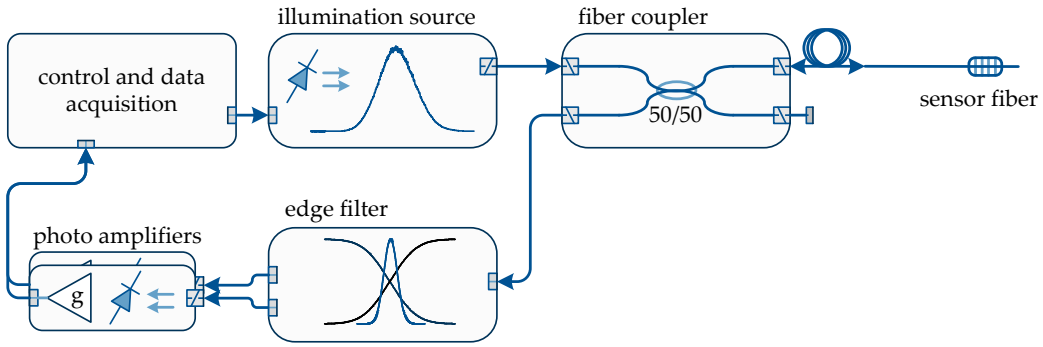

Fig. 5.4.: Edge filter based interrogator. A broadband illumination source illuminates the sensors, edge-filtering determines the sensor response.

Compared to spectrometer and tunable laser approaches, where the bandwidth of the systems is limited by the rates of CCD read-out respectively wavelength tuning, this measurement principle shows a higher bandwidth since the sensor response (ratio of two intensities) can be evaluated by means of analog hardware. Thereby sampling only occurs when the evaluated response is digitized and stored.

Tuning Laser Based Systems

This design uses a narrow band laser as light source that scans through the optical spectrum. Laser pulses at ascending wavelengths are sent to the FBG sensors. The intensities of light pulses that are reflected by the sensors are measured by a photo detector. Since the wavelength of the pulses is known, just the intensity magnitude of the reflected light is of interest. The sensor responses are determined by centroid calculation of the reflected intensities.

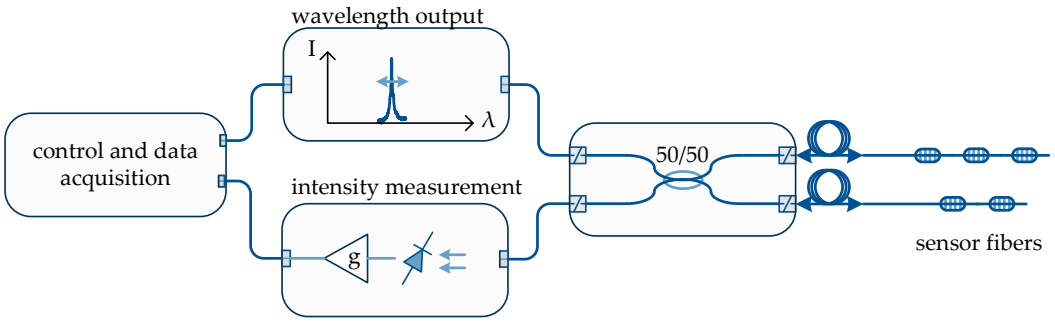

Fig. 5.5.: Tuning laser based interrogator. The output wavelength of the laser is tuned, thereby the spectral sensor response is scanned.

5.4. MG-Y Tunable Laser Technology

The tuning laser, which is the core element of the scanning laser interrogator that is developed within this work, is a monolithic diode laser of which the wavelength can be controlled electronically. Basically two resonators are combined within the structure of this laser diode. Both resonators share the same partially transmissive end mirror at one end. At the other end, a grating structure acts as second reflector as shown in figure 5.6.

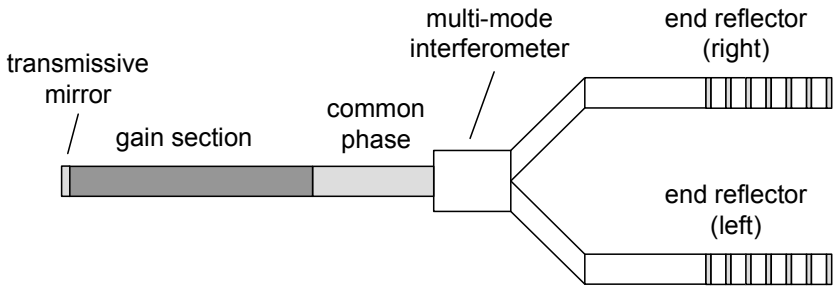

Fig. 5.6.: Structure of the modulated grating laser diode. The resonator is split into two arms, the vernier-effect is used for wavelength generation [189].

The MG-Y laser diode emits light at a wavelength where modes of each resonator overlap, as schematically shown in figure 5.7. The grating structures can be modulated by carrier injection allowing for refractive index modulation of

the grating material. Electric currents supplied to the grating reflectors adjust the free spectral ranges (FSR) of the resonators which originally are 630 GHz (5.05 nm) and 700 GHz (5.61 nm) [189]. Thereby the spectra of both resonators can be shifted against each other which allows to bring different modes of the resonators to overlap. By this so-called vernier effect [175] wavelength tuning is achieved. This kind of laser is called MG-Y laser, which is an abbreviation for its modulated-grating Y-structure.

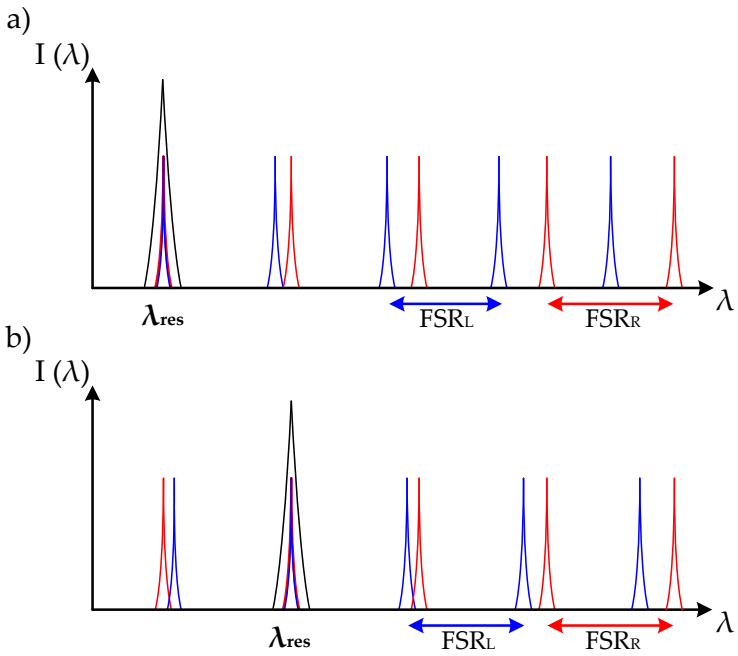

Fig. 5.7.: Additive Vernier effect. a) An output wavelength λ_{res} is generated at the spectral position where peaks of left and right resonator overlap. b) By increasing FSR_R, two other modes overlap and a different output wavelength λ_{res} occurs.

Contrary to sweeping laser sources [1] like external cavity diode lasers [73], the vernier effect does not support continuous tuning. A set of control currents may or may not yield one single stable output wavelength. Since both resonators show discrete spectra, the output wavelength jumps arbitrary when the control currents are changed. In order to use the MG-Y laser diode for spectral sampling of FBG sensors, it has to be characterized for all combinations of control currents (see section 8.4).

6. Development of Space Borne Systems

This chapter outlines specific characteristics that need to be taken into account when systems for space use are developed. In section 6.1, mission dependent constraints that affect system design and development are summarized and common engineering techniques required to develop space-borne systems are explained. The various environmental conditions in space are introduced in sections 6.2 (radiation), 6.3 (microgravity and vacuum) and 6.4 (shock and vibration).

6.1. Space Engineering

The term space engineering refers to the design, development and manufacturing of systems intended to be used in space. Several boundary conditions have to be taken into account and are therefore outlined in this sections.

6.1.1. Design Constraints

When a space mission is planned, the requirements for the systems on board the spacecraft have to be determined at first. This is done by comparing the mission parameters (e.g. launcher, platform, orbit altitude, lifetime, ...) with former successful missions. Furthermore, analysis and simulations concerning the new or changed boundary conditions are carried out. The requirements are thereafter derived from the obtained results.

When systems and subsystems are designed and developed, it has to be ensured that all requirements are fulfilled. Therefore the functionality of the system is tested under relevant environment by means of e.g. thermal-vacuum and radiation tests. Different models of the system (e.g. breadboard, engineering,

qualification and flight model) are built for consecutive stages of development according to [41]. In the case of complex mission scenarios, flight demonstration of critical subsystems is accomplished. The Laser Interferometer Space Antenna (LISA) mission for example utilizes the technology demonstrator LISA Technology Pathfinder (LTP) as forerunner mission wherein key technologies shall be verified [117].

The maturity of a system is characterized by the technology readiness level (TRL), a classification of systems and components given by ESA and NASA [45][110]:

TRL	Definition
1	Basic principles observed and reported (scientific research)
2	Technology concept and/or application formulated (applied research)
3	Analytical and experimental critical function and/or characteristic proof-of concept (laboratory experiment)
4	Validation in laboratory environment (laboratory testing)
5	Validation in relevant environment (environmental testing)
6	System/subsystem model or prototype demonstration in a relevant environment (ground or space)
7	System prototype demonstration in a space environment
8	Actual system completed and "flight qualified" through test and demonstration (ground or space)
9	Actual system "flight proven" through successful mission operation

A system is space qualified and therefore allowed to be implemented on board the spacecraft after it has been verified that a TRL of eight is achieved. Contrary to the development of ground based systems, engineering of space borne systems has to take into account special boundary conditions. Some aspects that have to be considered during development are outlined in the following list.

- **Compatibility with environment**
  The development of systems that operate on a spacecraft is mainly driven by the environmental conditions that the system is faced with during its lifetime. The environment, a space borne system has to be designed for, depends on the mission parameters, whereby the altitude mainly determines the in-orbit requirements for the system [101]. Only missions

based on earth orbiting spacecrafts (in contrast to deep-space missions) are in the view of this work. A space borne system has to cope with several different environments that occur sequentially:

1. **Transportation from development site to launching base:**
   Expected conditions are temperature ranges from $-15°C$ to $+40°C$, humidity, shock and vibrational loads during vehicle based transfer and possible solar radiation. Usually the system is not harmed by this environment since it can be thermally controlled and appropriately packed into protection covers.

2. **Launch, transportation and in-orbit operation during mission:**
   Radiation, vacuum and micro-gravity during operation of the system in space (sections 6.2, 6.3) and high shock and vibration loads during launch (section 6.4) are the main design drivers. The harsh environment in space which depends on the orbit, the kind of spacecraft that accommodates the system and mission specific parameters affect the system during the mission. The system has to be designed and developed such that it withstands the environmental loads.

3. **Transportation from mission orbit back to earth:**
   Missions where the system is sent back to earth after its mission lifetime, e.g. for data evaluation, are possible but are not elaborated in this document.

- **Autonomous work**
  Unlike devices deployed in laboratories, systems working in space must be stand-alone operable. One way is to design the system intrinsically stable so that readjustment is not necessary. If intervention is unavoidable, monitoring and adequate control mechanisms have to be implemented in order to either automatically or by remote control re-adjust the system.

- **Lifetime assessment**
  It has to be ensured that the entire system with all subsystems and components operates failure tolerant within the expected lifetime. Methods like derating [40] of components or implementation of system redundancy by e.g. parallel circuiting of electronics can be used.

- **Power efficiency**
  Because of the reduced energy disposition high efficiency and low power consumption is required. Also in view of thermal controlling inside the spacecraft, a minimized waste heat is desired.

- **Dimensions and weight**
  The reduced dimension of the satellites require compact system design to achieve low volume and weight.

- **Electromagnetic compatibility**
  All electronic and opto-electronic equipment has to be EMC-safe which requires special design [58]. Furthermore the system itself must not harm surrounding equipment by generating electromagnetic radiation.

- **Safety margins**
  In order to ensure correct system operation even if there are deviations between expected and actual operation conditions (e.g. unforeseen solar flares that result in enhanced radiation exposure), safety margins have to be applied to all requirements. Compliance with increased requirements is guaranteed by enhanced qualification testing [39].

6.1.2. Development Guidelines

In former days no uniform system of space standards was available [93]. Therefore different companies used different standards. Divergences between the standards resulted in misunderstandings between companies and thereby in failures of developed systems. Additional effort was necessary to compare the standards among each other which yielded higher development costs.

The European Cooperation for Space Standardization (ECSS) was founded in 1993. ECSS is an association of ESA, national space agencies and a consortium of companies from the industrial sector. These partners singed a contract for development of a common framework of standardization. It aims to create and maintain common standards for space related development. Thereby cost efficiency, performance enhancement and competitiveness of the European space industry on the world market shall be achieved and enhanced.

The policy of ECSS was defined in one separate document and arranged the principles of the new system. Key points of ECSS policy are:

- ECSS standards have to be made applicable to a project by contract, they are not legal by itself. The contracting party that introduces an ECSS standard as requirement document is responsible for control of compliance of the development with the standard.
- Requirements shall be defined target-oriented rather than task-oriented: The performance that has to be achieved rather than the description of the way to achieve it is the objective of a standard. This leaves the way open for new technological developments.
- ECSS standards shall not duplicate other norms e.g. ISO or EN standards. Instead links to already existing and complementary standards shall be included.

From the very beginning of ECSS, this standardization was intended to stay in motion since it is continuously adapted to changes in technology. The ECSS system has been established as common guideline to all space-related development within Europe since its beginning. It is divided into three main branches:

- **Space Project Management**
  All standards necessary for successful project execution in terms of cost, schedule and performance.
- **Space Engineering**
  All standards covering the engineering aspects of the project, e.g. requirements for the development of electrical, mechanical and optical systems as well as overall system engineering.
- **Space Product Assurance**
  All standards to assure that all products and systems fulfill the requirements. Support of risk management by the early identification of risks is covered by these standards.

A four level system was taken as basis for the architecture of ECSS in 1993 [93] which has been reduced to three levels in 2003 [47]. The first level standard (ECSS-S-ST-00C [46]) describes the objectives, policy, architecture and the

strategy (former a separate level) of every specific branch of the ECSS system. Second level standards are all standards within one of the three ECSS branches (ECSS-M-ST-xx-yyy, ECSS-E-ST-xx-yyy, ECSS-Q-ST-xx-yyy). They describe the requirements and functions for all aspects in the respective domain. Third level documents are additional non-normative guidelines that describe methods, processes or procedures to achieve the requirements of level-2 standards. Level-3 documents are available as handbooks or technical memoranda and can be adapted to the project if necessary [46].

6.2. Space Radiation

Radiation is of major concern for systems operating in space. Properties of electronic and optic equipment are altered when irradiated with particles (e.g. protons, electrons, heavy ions) or with electromagnetic waves (e.g. x- or Gamma rays, light). Even system failure due to radiation occurred in former missions. A latch-up damage (section 6.2.2) of a random access memory chip on board the Precision Range and Range-rate Equipment (PRARE) satellite due to proton impact for example lead to the loss of the satellite five days after launch [71]. Implementation of a latch up detection circuit during development and controlled reset of the system may have resulted in an failure tolerant operation of the satellite.

6.2.1. Space Radiation Environment

The Earth is subjected to a nearly isotropic flux of charged particles, beta and gamma rays. The radiation flux is mainly generated by solar flares of the sun, but also by omni-directional galactic cosmic radiation originated outside the solar system. The flux of the charged particles consists of about 85% protons (hydrogen nuclei), 14% alpha-particles (helium nuclei) and 1% heavier ions (e.g. iron and carbon nuclei) [36].

A particle is only able to pass the magnetic field of Earth by having a certain energy level (below 1 GeV at the poles, up to 17 GeV at the equator). Incoming particles of lower energy are deflected toroidal round the earth by Lorentz

forces. Research lead by James Van Allan revealed that two radiation-belts with high concentration of trapped particles exist around Earth. The inner belt at an altitude around 3000 km mainly consists of protons and electrons at fluxes of $2 \cdot 10^5 \frac{particles}{cm^2 \cdot s}$ and $3 \cdot 10^6 \frac{particles}{cm^2 \cdot s}$ for energies above 10 MeV and 1 MeV respectively. The outer belt at an altitude of approximately 25000 km consists of electrons at a flux of $2 \cdot 10^6 \frac{particles}{cm^2 \cdot s}$ (energy > 1 MeV) [13][78].

6.2.2. Radiation Effects

When matter is exposed to radiation, the effects of interaction depend on several parameters: mass, charge, kinetic energy, incidence angle of the particle or ray, type and density of the targeted matter. Degradation that occurs in electronic or optical components is due to either ionizing or atomic displacement effects dependent on the type of particle or ray.

- **Ionization**
  Charged particles interact primarily by Rutherford scattering (Coulomb scattering). This interaction can cause excitation or ionization of atomic electrons (electron-hole pair generation) [30]. Total ionizing dose (TID) is the measure of ionizing radiation. The unit of TID is rad or Gy (Gray) whereby $1\ Gy = 100\ rad$.

- **Atomic displacement**
  If sufficient energy is transferred to atoms, they are displaced from their normal lattice positions. Heavy charged particles can cause elastic or inelastic scattering. In an elastic collision, the bombarding particle transfers a portion of its energy to an atom of the target material, and can dislodge the atom from its lattice position [168]. Non-ionizing energy loss (NIEL) is the measure of non-ionizing radiation effects. The unit of NIEL is MeV/g.

Charged particles e.g. heavy ions which incident on matter can cause both, ionizing and displacement effects.

Radiation Effects on Semiconductors

Ionizing radiation results in cumulative energy deposited in a given volume. Most of the converted energy of an incident particle creates electron-hole pairs. At this ionization, the valence band electrons in the solid are excited to the conductor band, thereby enabling n-type conduction in the conductor and p-type in the valence band. This produces a variety of device effects like energy band shifts or leakage currents which can for example yield gate threshold voltage shifts in CMOS devices [125]. Furthermore, high energies of radiation lead to internal charging of conducting layers in electronic devices. If high potential differences between layers separated by insulators are reached, electrical breakdowns and damage are caused. Sources that ionize the material are electrons, protons and Bremsstrahlung, which is a secondary radiation due to slow down of incoming particles like heavy ions.

Ionizing based damage of electronic devices show the following characteristics [48][137][125]:

- Biasing of semiconductor devices leads to higher radiation damage compared to unbiased operation.
- Trapped charge reduces after irradiation dependent on the temperature and applied electric field, whereby the damage is partially or completely cured.
- Although some devices are no longer sensitive to dose-rate effects below approximately 1 rad(Si)/s, other devices continue to be affected even at dose rates of 0.002 to 0.005 rad(Si)/s [82]. In linear devices with junction isolated bipolar transistors enhanced low dose rate sensitivity yields higher damage at low dose rates [82] [83][183][54].

Atomic displacement (AD) is caused by incoming high mass particles such as protons and heavy ions. Atoms are thereby displaced from their crystal lattice position leading to stable defects created within the bandgap. AD is of major concern for bipolar transistors because these devices are based on minority carrier conduction [163]. Since AD leads to a reduction of minority carrier lifetime, the transistor gain reduces significantly [167][145][192][137].

The following damages can occur due to AD radiation effects [36]:

- Trapping of carriers at lattice defects leading to losses in charge transfer efficiency (minority carrier trapping) or carrier removal (majority carrier trapping).

- Compensation of donors or acceptors and recombination of electron-hole pairs leading to carrier removal.

- Tunneling of carriers leading to increased current in reverse biased junctions - particularly for materials with small bandgap and high applied electric fields.

Single event effects (SEE) are caused by single energetic particles (e.g. protons, neutrons or heavy ions) or high energy cosmic rays. Single strikes of these particles, when passing through the material, cause ionized tunnels with diameters of a few micrometers. Inside electronic devices like transistors, a variety of different SEEs may occur [123][36][78]:

- Single event upset (SEU) is a transient effect, a so called soft error. Mainly affected are memories and all kinds of logic state devices as well as processor chips. The hitting particle leads to a change of stored information also called bit-flip. The effect is nondestructive and may be corrected by overwriting of the affected element. Also resetting of the device results in normal behavior.

- Single event latch-up (SEL) can lead to demolition of the device. In CMOS circuits, for example, SEL occurs when both complementary transistors are conducting at the same time. SELs are hard errors and may remain even after restarting of the device. A SEL can be cleared by a power off-on reset. To protect the device either the power has to be removed very quickly or an upper current limit has to be ensured which is lower than the damage threshold of the device.

- Single event transients (SET) in linear circuits are current transient which can be interpreted as signal edge in combinational logic and thereby cause a logical error.

Radiation Effects on Optical Components

Physical effects, that occur when optical components are irradiated, are not understood completely [180]. During irradiation of optical components fluorescence can occur and influence surrounding equipment [78]. Long term degradations in transparent materials are transmission losses. These losses are due to the presence of crystalline defects, so called color or F-centers (from the German word "Farbe") [43][121]. Exposing optical material to radiation results in the displacement of lattice ions and thereby in the creation of lattice vacancies. In particular irradiation with heavy particles alters the lattice structure. If an electron from the valence band is excited into this vacancy it gets trapped and a F-center is created. In terms of the energy levels, a F-center lies within the bandgap of the optical material between the valence and conduction bands [191]. Electrons in such a vacancy absorb photons in the visible spectrum such that the transparent optical material becomes colored. If occurring radiation e.g. light has a very high energy or intensity, the electron may be released from the vacancy. Thereby the material gets (photo-) bleached and loses its color.

Radiation Damage in Optical Fibers

At NASA, databases of radiation test results on several types and brands of optical fibers are available [133][131]. In general, optical fibers have been used for space applications for more than 30 years [132] without failures. Rare-earth doped optical fibers however are well known to be highly radiation sensitive [130][25][64]. In other areas of research, e.g. for nuclear power plants, the radiation sensitivity of rare-earth doped fibers is used for dosimetry [21][23][19]. Guiding high-intense light through attenuated fibers allows to cure the defects by photo-bleaching [22]. This photo bleaching effect is confirmed by the radiation tests carried out in this work (see section 7.5).

Preliminary examinations performed by the Max-Planck-Institute of Quantum Optics in cooperation with Kayser-Threde GmbH evaluated all types of fibers implemented in an Erbium doped optical frequency comb [84]. Several tests with different radiation sources have been conducted whereby the transmission loss at the wavelength 1310 nm was measured. Standard telecommunication single mode-fibers and highly nonlinear fibers (see chapter 4.5) showed trans-

mission losses of less than 0.01 dB/m after irradiation with a total dose of 955 Gy. The Er doped fiber showed transmission losses of 3 dB/m after a total dose of only 190 Gy and 10 dB/m after 380 Gy. During the irradiation with 20 MeV protons an Yb doped fiber was tested additionally. After irradiation of both rare-earth doped fibers with $12 \cdot 10^{13}\ \mathrm{protons/cm^2}$, the transmitted intensities were reduced by 1.55 dB for the Er and 0.65 dB for the Yb doped fiber for lengths used in fiber combs.

Radiation exposure causes F-centers which degrade the performance of the fibers by attenuation. Several radiation test results on rare-earth-doped optical fibers are available in literature e.g. [59][74][179], but test conditions like dose rates, total dose and dopants of the fiber vary for each experiment. Ytterbium doped fibers are known to be less sensitive to radiation than Erbium doped ones [55].This allows only qualitative comparison of the results [130]. Not the doping concentration levels of the rare-earth material but of the co-dopants e.g. aluminum increase or decrease the radiation sensitivity[74].

Up to now it has not been clarified, which doping composition is best suited for low radiation sensitivity but hydrogen loading is a technique for radiation hardening [75][198][76]. Fibers are therefore coated with metal or carbon and loaded with hydrogen under high temperature and pressure. The coating prevents the hydrogen from outgassing. It has been shown by the Fiber Optic Research Center (FORC) in Moscow that hydrogen loading of hermetically coated Er doped fibers extends their lifetime in space by more than five times. Exposing the fibers to Gamma radiation from a Cobalt-60 source (0.028 Gy/s) to an accumulated TID of 2 kGy only reduced the lasing efficiency at 980 nm by 1 dB. Pumping the fiber at a wavelength of 980 nm enhances photo-bleaching effects which supports the radiation hardness of the fiber [199]. FORC kindly provided several meters of Erbium doped hydrogen-loaded fiber that where tested in the frame of this work (see chapter 7.5).

Radiation Effects on Fiber Bragg Gratings

Irradiation of fiber Bragg gratings (FBG) in optical fibers results in a shift of the spectral response of the sensor due to a change of the refractive indexes n_1, n_2 and n_3 of the fiber (see figure 5.1). Spectral shifts around 25 pm for total

doses up to several hundred krad have been observed [14][67]. Recovery of the FBG spectral shifts are possible after several hours [178] of annealing or by applying even higher doses of several Mrad [70]. Writing FBGs by femtosecond pulsed UV lasers makes the spectral shift of the sensor independent from the fiber material [66]. Width and amplitude of the FBG spectrum are not altered by radiation. Furthermore the fiber coating has an influence on the wavelength shift, when the fiber is stressed by e.g. shrinking of the coating due to radiation [65]. Long-term irradiation of FBG sensors over a period of 40 month in a nuclear reactor revealed suitability of FBG sensors [52]. The selection of the fiber material and the fabrication technique of the FBG enables to produce sensors that are less sensitive to radiation [69]. Contrary to rare-earth doped fibers, where hydrogen loading decreases radiation sensitivity, FBG sensors should be written in photo-sensitive fibers with a high Germanium concentration [68].

6.2.3. Simulation of Radiation Exposure for Orbital Missions

In order to design and develop a satellite system, the expected radiation environment of the planned mission has to be identified. This can be done using the online simulation software SPENVIS (Space Environment Information System) provided by ESA [44].

Tab. 6.1.: The Earth orbit is usually divided into three regions: LEO, MEO and GEO. The simulation parameters given are used for achieving the results of figures 6.1 and 6.2.

Earth Orbit	**Low**	**Medium**	**Geostationary**
Altitude [km]	200 – 1200	2000 – 35000	35786
Typical mission	Earth observation	GNSS	Telecom
Simulation parameters			
Altitude:	820 km	23600 km	36000 km
Inclination:	98.8°	56°	0°

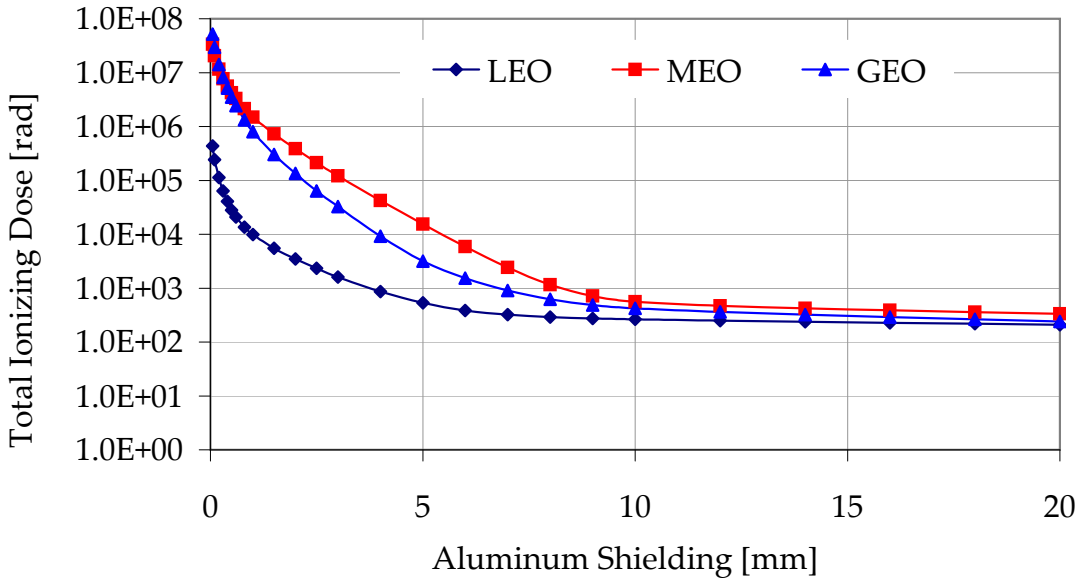

Fig. 6.1.: Accumulated total ionizing dose within a mission duration of one year according to the orbit parameters given in table 6.1 simulated with SPENVIS [44].

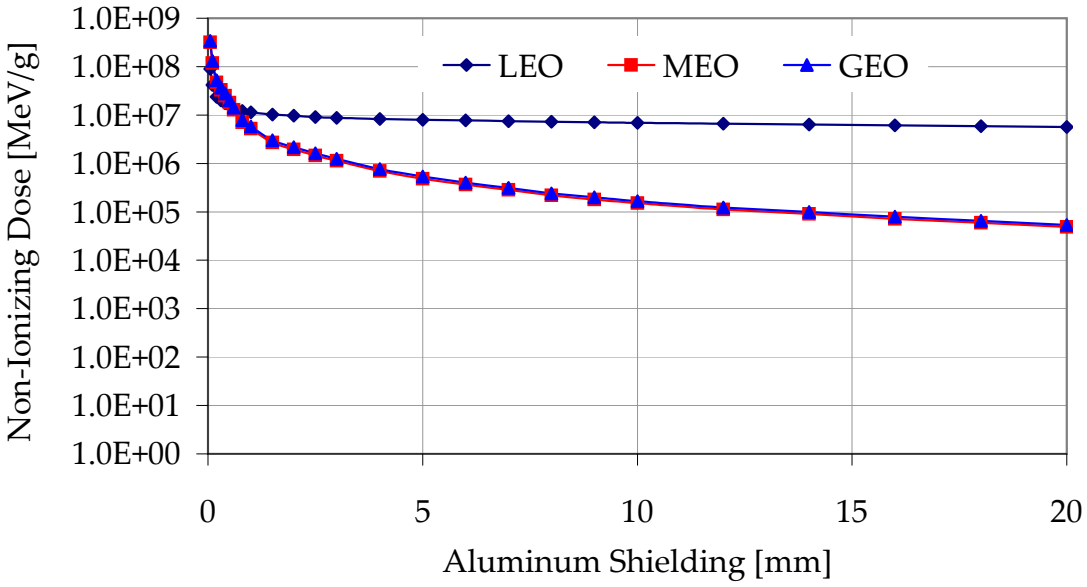

Fig. 6.2.: Accumulated non-ionizing dose within a mission duration of one year according to the orbit parameters given in table 6.1 simulated with SPENVIS [44].

Different simulators can be used to determine the accumulated dose of electromagnetic and particle radiation for user defined orbits in dependence of shielding. Figures 6.1 and 6.2 show the simulation results for the three main orbit types LEO (low Earth orbit), MEO (medium Earth orbit) and GEO (geostationary Earth orbit) according to Table 6.1. The total ionizing dose (see figure 6.1) in MEO is higher than in GEO due to the outer Van Allan radiation belt. Therefore most of MEO's total dose is due to electron irradiation. Because of the inner belt, that consists mainly of protons, the non-ionizing dose is highest for LEO.

A radiation sensor onboard the GIOVE (Galileo in-orbit verification) satellite verified SPENVIS simulations carried out prior to the GIOVE mission, although with divergences within measurement accuracy [149].

6.3. Microgravity and Vacuum

Thermal effects on space-borne systems occur due to microgravity and due to vacuum. Therefore descriptions of both environmental effects are combined within this section. During lift, earth's atmosphere is left whereby the outside pressure of the spacecraft reduces. If gas inside the system has to be released, some kind of vents are necessary to ensure that the housing of the system is not harmed by forces due to remaining pressure differences.

6.3.1. Thermal Issues

Due to vacuum and the absence of gravitation, thermal convection is not available for heat transfer (unless pressurized housings and fans are used). Therefore only thermal radiation and thermal conduction can be used for waste heat dissipation. Thermal radiation only works, if the surrounding equipment serves as heat sink at a lower temperature than the system that dissipates heat. If this is not the case in a spacecraft, copper bands connect the heat source inside the spacecraft with a heat sink that is located outside and points to deep space. The design of the heat conductor takes into account the required operation temperature and amount of waste heat of the system. Adequate design of the thermal

interface can be challenging, if the system has different operation modes that produce different amounts of waste heat. Thereby the heat conductor has to be designed such that the system keeps its operating temperature within the range from minimum to maximum produced waste heat. If this is not possible either an active temperature control, e.g. heat pipes or electric heaters have to be used. Another approach can make use of a pressurized housing where the system is encapsulated. Due to the absence of gravity, ventilators have to be used to enable heat exchange by thermal convection inside the housing. This solution is only possible, if the housing is colder than the heat source.

Temperature control and dissipation of waste heat by conduction result in enhanced complexity of the system. This goes along with higher development and production costs and reduced overall efficiency of the system. Therefore the development of space borne systems aspires to an enhanced temperature range the system can cope with, or to internal heat exchange mechanisms whereby external heat transport is minimized.

6.3.2. Outgassing Issues

Synthetic materials, e.g. polymers or lubricants, can include plasticizers that diffuse out of the material under vacuum conditions. One negative effect thereof is reduced flexibility or altered characteristics of the material. If for example the material is used as a seal, the closeness of the system may disappear. Moreover the freed molecules can cause problems if they contaminate surfaces from e.g. free space optical components. Outgassing strongly depends on temperature, the higher the temperature, the faster the outgassing progresses. Thus procedures like thermal cycling or out-baking of materials can be carried out to intentionally cause outgassing of materials prior to their use as components in the system.

Outgassing is attended by mass loss due to the freed molecules. ESA and NASA hold data bases with qualified materials that show a tolerable total mass loss (TML) [165]. The lower the TML, the better the material is suited for space applications.

6.4. Shock and Vibration

High vibrational loads with accelerations up to several hundred g dependent on the launcher that is used (e.g. Ariane, Sojus or Vega) affect the system during launch. Usually the launcher has several stages that are ignited consecutively. Every time one stage is burnt-out, it is separated from the launcher by explosive charges. Thereby shock loads up to several thousand g appear. Within the user manual of the Ariane 5 launcher [139], shock values up to several thousand g are given as worst case assumption. This has to be taken into account, when a system is design for a mission that is launched by Ariane. The shock and vibration loads that penetrate the instrument e.g. an OAC or OFC inside the satellite housing are lower due to damping of spacecraft and instrument mountings. If, however, a sensitive or alignment critical part of an instrument has to cope with such requirements, either the mounting has to be mechanical robust enough or additional locking mechanisms have to be implemented. Special devices are available that lock e.g. moving parts of a system to a save position during launch. As soon as the satellite is in orbit, the mechanism releases and normal operation can start. The challenge is not to construct a locking mechanism that withstands the shock load, but to make sure that it is able to release by all means even after high loads have been applied to the mechanism. Therefore mature technologies have to be used, some of which are commercially available [182].

7. Development Tests of Optical Frequency Combs for Space Applications

This chapter summarizes the optical frequency comb development for applications in space carried out in this work. First, in section 7.1, two promising laser sources are selected for further development. Their characteristics are described in section 7.2. Test planning and considerations concerning the test facilities are shown in section 7.3. Thermal-vacuum and Gamma-radiation tests and corresponding test result evaluation are summarized in sections 7.4 and 7.5.

7.1. Selection of OFC Technology for Further Development

Various OFC setups, based on different laser technologies, are under investigation throughout the scientific laboratories and national metrology institutes. Therefore an inquiry was performed taking into account mainly space compatibility issues of the various OFC technologies. Several other schemes than the examined Titanium-sapphire and fiber based lasers exist [51]. A promising candidate is an OFCs based on microresonators [31][28][7]. Since this technology is still under development and has not lead to a commercial product (TRL < 4 [110]) it has not been taken under consideration for development of a space-borne system within this work.

Table 7.1 shows a qualitative evaluation of the studied OFCG technologies. The field of OFCG technologies was divided into fiber and bulk lasers. Thereby a trade-off between technologies that are compatible with space environment and that show high performances has been carried out. The result is that fiber

based OFCG technologies based on Erbium and Ytterbium doped fibers are promising candidates for a later operation in a space-borne system.

Tab. 7.1.: Trade-off between fiber based and bulk laser sources. Although the measurement performance of fiber based systems is moderate compared to the high performance of e.g. bulk lasers, their overall applicability for space-borne systems is high.

Requirement \ Laser technology	Fiber Lasers (e.g. Er and Yb doped)	Solid State Laser (e.g. Titanium-Sapphire)
Technological maturity	High	High
Robustness of setup	High	Low
Compactness of setup	High	Low
Service-free operating time	High	Low
Operational lifetime	High	Medium
Power efficiency	High	Low
Measurement performance of OFC	Medium	High

Most of the complexity of an OFC lies in the femtosecond laser source also called optical frequency comb generator (OFCG). Two fiber-based OFCGs have been selected for further development within this work. In particular thermal-vacuum and Gamma-radiation tests have been carried out in order to evaluate space compatibility of the lasers. Fiber based OFCs have already demonstrated long-term and stand-alone operability [99][32].

7.2. Description of OFCG Systems

Two ultra-short pulsed laser systems have been tested. The main characteristics of both systems are listed in table 7.2. Laser-1 is completely equipped with

control actuating mechanisms that would allow to use it as OFCG in a stabilized OFC setup. Laser-2 does not support OFC generation because of its long pulse duration and missing control mechanisms for OFC stabilization. However, the technology of Laser-2 can be further developed to a space-borne OFC because of its stable pulse generation based on SESAM soliton mode-locking [172].

Although Laser-1 and Laser-2 are not comparable in terms of their performance because of their different characteristics, they allow evaluation and comparison in terms of space compatibility.

Tab. 7.2.: Key parameters of the two OFCG systems based on Erbium and Ytterbium doped fibers.

	Laser-1	**Laser-2**
Mode-locking principle	NLPR	SESAM-soliton
Gain fiber	Erbium doped	Ytterbium doped
Fiber type	Single-mode	Polarization maintaining
Output wavelength	1550 nm	1030 nm
Mean output power	45 mW	10 mW
Pulse duration	≈ 100 fs	≈ 6 ps
Repetition rate	100 MHz	30 MHz
Control mechanisms for OFC stabilization	Yes	No

7.3. Test Plan and Test Environment

The intention of the accomplished environmental test sequences was to identify the ranges within the OFCG operates normally rather than to test the OFCG within a given temperature range or up to certain level of radiation dose. Therefore two environmental tests have been carried out successively:

1. Thermal Vacuum Test
   This test simulates the temperature range inside a typical spacecraft under vacuum condition. Only thermal radiation at the surface and thermal conduction through the mounting of the OFCG is available for heat transfer. In order to verify the measurement results, thermal simulations have been conducted prior to the TV test.

2. Gamma Radiation Test
   Space radiation is a serious issue especially for optical and electronic components (see also chapter 6). Therefore the optical gain fibers of both OFCGs and the SESAM, which have been identified to be most sensitive to radiation, were exposed to Gamma radiation.

In order to enable identification of a possible error source during environmental testing, only the most critical parts of the OFCG were subjected to the relevant environment. During thermal-vacuum (TV) tests only the optical laser-head resided inside the thermal vacuum chamber and during Gamma-radiation tests, the critical elements (gain fibers and SESAM) were tested sequentially. Irreversibly damaged components were exchanged after each test. During all tests the output parameters were monitored on-line.

7.3.1. Measurement Setup

A computer controlled test system has been set up to perform all tests automatically. Both subsystems of the OFCG, the laser head and the control unit, are connected to a set of measurement instruments during the test series similarly to figure 7.1.

All measurement instruments as well as the OFCG itself are controlled by a host platform based on a PXI system of National Instruments®. Also data acquisition of measurement data of all instruments is performed by this host using LabVIEW® software. Therefore control panels of the instruments are emulated in order to allow instrument remote control which is similar to nominal operation of the single devices. Settings of all instruments are stored as header information within each single measurement file [60]. This ensures

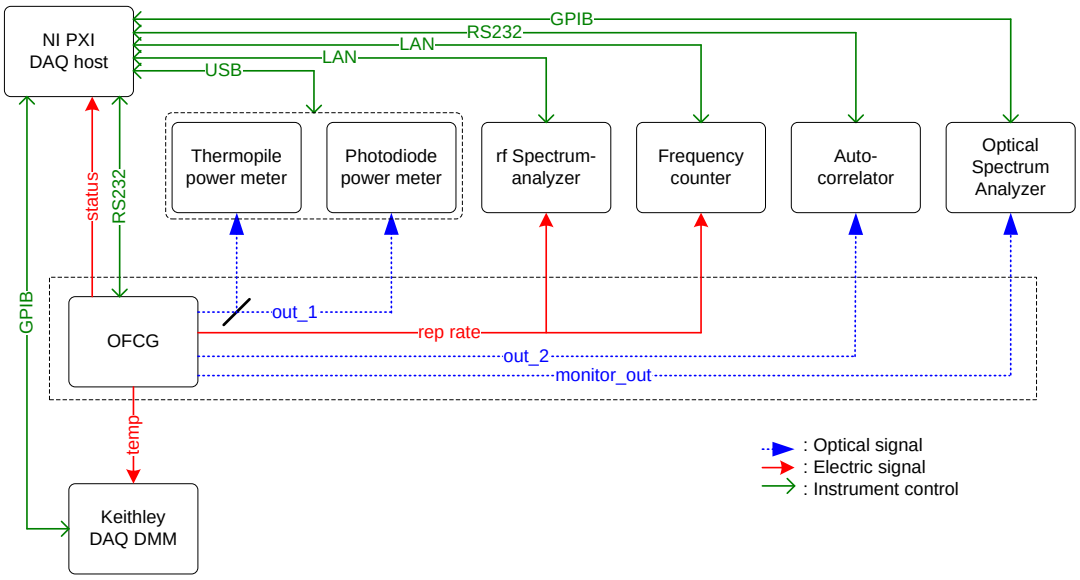

Fig. 7.1.: All measurement instruments are controlled by a central host PXI computer from National Instruments®. Measurement data of all instruments are sent to the host for storage.

that measurement results are repeatable and error calculations, which usually depend on the instrument settings, can be carried out after the test series. The OFCG electronics is powered by an UPS (Un-interruptible Power Supply) in order to eliminate external power disturbances. This precaution is of particular importance since the OFCG electronics is equipped with sensitive auto shut-off features that can be triggered by voltage spikes. Since the measurement system carries out all tests in stand-alone condition, it becomes of special importance that tests, which are not continuously supervised by an operator, are not interrupted. Part of the measurement equipment (e.g. autocorrelator) is connected to the laser head via free space optics. Where necessary, care has been taken to optimize the polarization orientation of the OFCG output signal relative to the required instrument input.

7.3.2. Test Parameters

The following parameters have been selected for monitoring throughout the test series:

- Temperature data from thermal sensors inside the laser head.
  Up to 16 temperature sensors have been distributed inside the Er and Yb laser heads. Thereby temperature gradients inside the laser head are measured during TV testing and are compared to thermal simulation results.
- Spectral width of the laser pulse
  An optical spectrum analyzer (OSA) was used to measure the spectral width of the output pulses of the lasers.
- Repetition rate
  A photo detector in combination with a frequency counter was used to continuously log the repetition frequency of the laser.
- Optical output power
  Optical power meters continuously log the output power of the lasers under test.
- Temporal width of emitted pulses
  An optical autocorrelator is used to measure the temporal width of the emitted pulses.

7.3.3. Test Facilities

Thermal Vacuum Chamber This test environment supports a pressure of less than 10^{-5} mbar. Within the TV chamber a thermal shroud accommodates the OFCG laser head. Temperatures from 113 K to 433 K can be applied to the DUT. The temperature of the thermal shroud is actively controlled by electric heaters and nitrogen cooling with a maximum temperature gradient of $1°C$ per minute. By placing the OFCG on thermal insulation posts, only heat transfer based on thermal radiation was available. The inner sides of the walls of the thermal shroud are the only heat source and sink for the OFCG.

Radiation Source This test environment is based on the radioactive isotope Cobalt-60 ($^{60}_{27}Co$). The test facility provides a dose rate of up to 45 Gray per hour. $^{60}_{27}Co$ decays into an excited state of Nickel by emission of electrons at

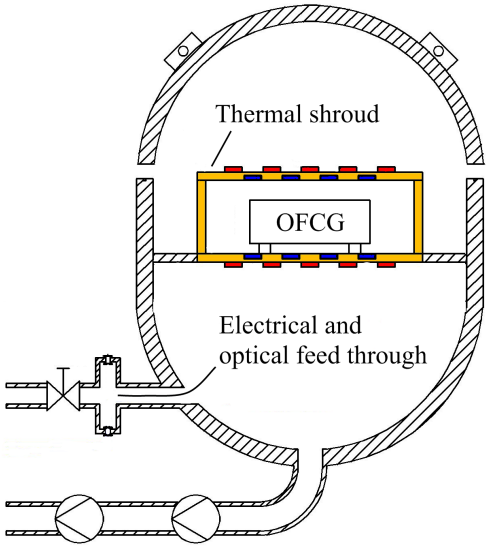

Fig. 7.2.: Overview of the thermal vacuum setup which accommodates a thermal shroud for temperature control. The OFCG is installed inside.

energies of either $0.31MeV$ or $1.48MeV$. Afterwards the excited Nickel sends out gamma rays with energies of $1.17MeV$ and $1.33MeV$ in order to reach its ground state $^{60}_{28}Ni$. Figure 7.3 shows the decay scheme of Cobalt-60.

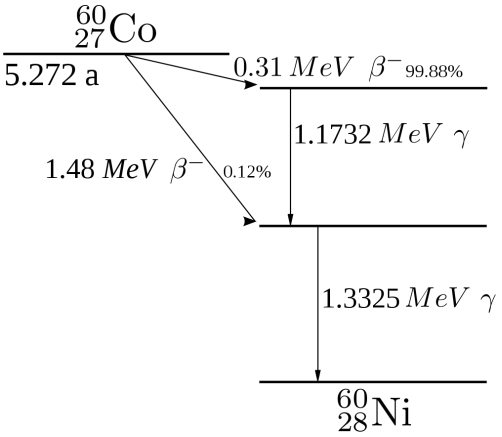

Fig. 7.3.: Cobalt-60 decays into Nickel-60 by sending out electrons and gamma rays [95].

In order not to distort the radiation test results by the appearance of beta radiation, an acrylic glass plate with a thickness of 5 mm was placed between the radiation source an the OFCG. Thereby electrons are efficiently blocked [78].

7.4. Thermal-Vacuum Testing

This section summarizes the TV test results. Prior to the TV tests a thermal model of the OFCG has been created in order to verify the measurement results. Experiences with the systems are interpreted with regard to operation of the OFCG in a later space environment.

7.4.1. Thermal Simulation

Integrating a standalone OFCG inside a satellite requires appropriate thermal management. The OFCG itself dissipates electric energy and therefore builds a heat source. Surrounding heat sinks like other systems or the satellite housing itself enable heat exchange between the OFCG and its environment. Mounting interfaces of the OFCG that are used to conduct the produced heat to e.g. external radiators need to be defined in terms of size, thermal conductivity and temperature in order to act as a thermal sink. This is necessary in order to reach a balance between the heat that is generated by the OFCG due to electric energy dissipation and the heat that is radiated or lead off the OFCG housing without exceeding the allowed temperature range of the OFCG.

As a first step a steady state analysis was performed. Therefore a simulation tool was programmed based on Stefan-Boltzmann's law of thermal radiation [140]

$$P_{rad} = \frac{\sigma}{\frac{1}{\varepsilon_{OFCG} A_{OFCG}} + \frac{1}{A_{housing}} \cdot \left(\frac{1}{\varepsilon_{housing}} - 1\right)} \left(T_{OFCG}^4 - T_{housing}^4\right) \tag{7.1}$$

and on thermal conduction via the mounting interfaces [100]

$$P_{cond} = \frac{\lambda n A_{mounting} \left(T_{OFCG} - T_{housing}\right)}{l}. \tag{7.2}$$

The surface area of the OFCG A_{OFCG}, the satellite housing $A_{mounting}$ and a number of n mounting interfaces with a footprint of $A_{mounting}$ and a length of l as well as the thermal parameters conductivity λ and emittances ε_{OFCG} and $\varepsilon_{housing}$ are entered by the user. A root-finding algorithm based on the regula-falsi method [143] is then used to find the point of thermal equilibrium.

Thereby it is assumed, that the power difference ΔP between the supplied electric power P_{el} and the optical output power P_{out} of the OFCG equals the waste heat power: $\Delta P = P_{el,in} - P_{opt,out} = P_{cond} + P_{rad}$. After several cycles of the numerical algorithm the steady state temperature of the OFCG within a given maximum error range of 5 mK is found and displayed. Figure 7.4 shows the GUI of the simulation tool where the parameters can be entered and the steady-state result is displayed.

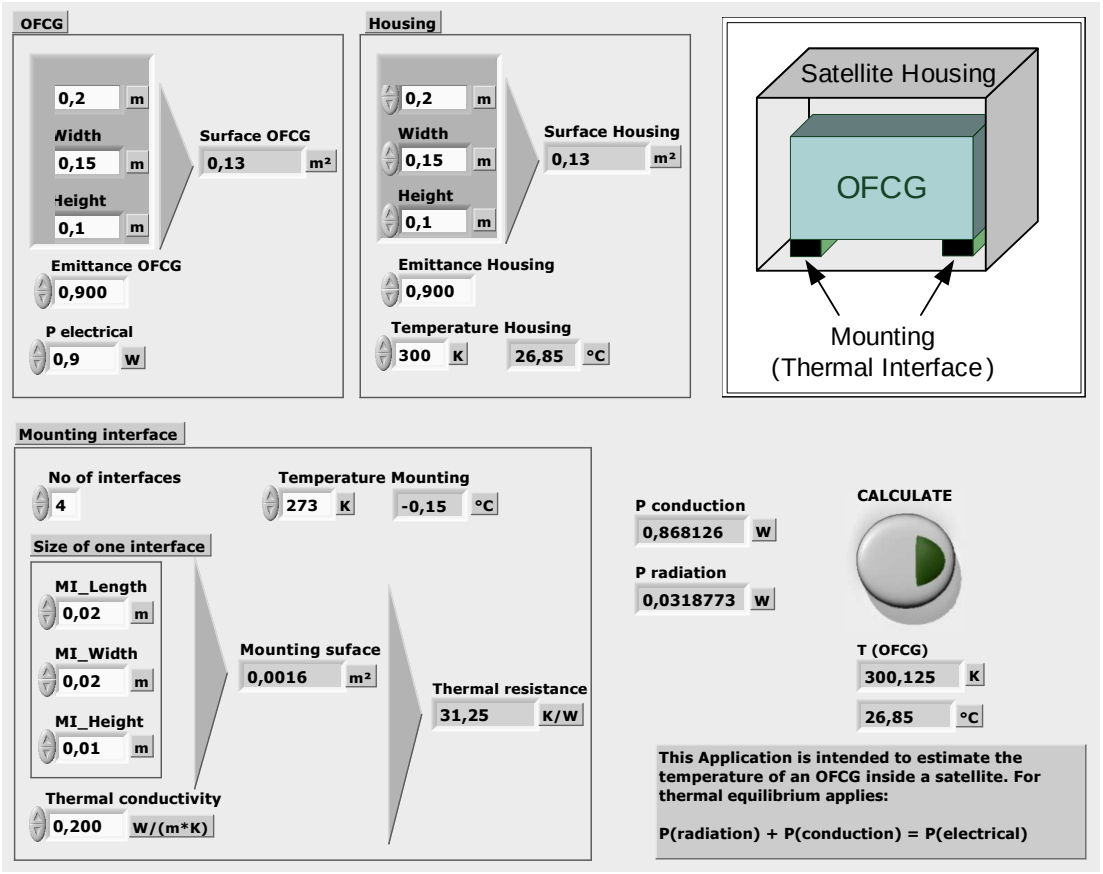

Fig. 7.4.: This simulation tool has been developed in order to calculate the thermal equilibrium of an OFCG inside a satellite. The thermal equilibrium is calculated using a numerical method that takes into account heat transfer by means of conduction and radiation.

This simulation is a first estimation where the OFCG is assumed to be a homogeneous block without internal temperature gradients. Also the obtained results are only true for infinite settling time with constant conditions. As a

starting point for the dimensioning of mounting interfaces to the satellite bus, however, the results of this simulation software have been proven to be realistic.

As a second step the internal temperature distribution was simulated using FeMap® finite element simulation software. Therefore thermal models of OFCG and TV chamber were created and a simulation was performed that revealed the internal temperature distribution. Therefore it was assumed that the difference between optical pump and optical output power is equal to the waste heat that is produced by the optical gain fiber inside the laser head. Furthermore, mean values for the rejected heat of the electric actuators have been assumed. Since the position of the gain fiber and all actuators are known, a precise model could be established (see figure 7.5).

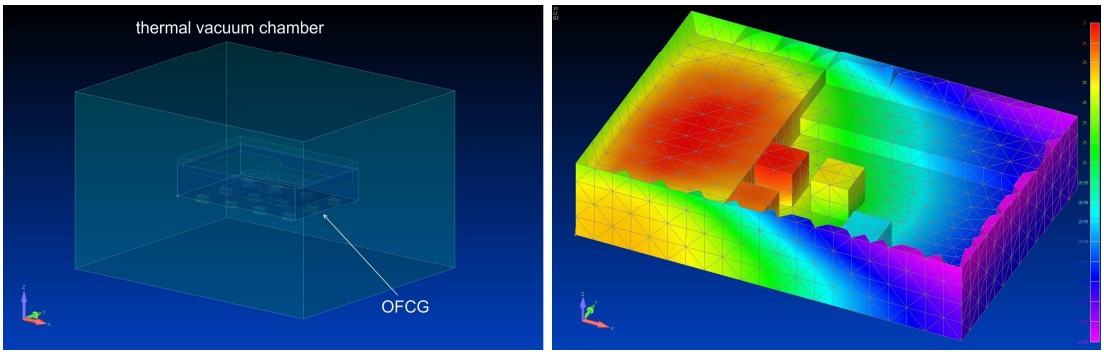

Fig. 7.5.: A thermal model of the OFCG was developed in order to verify measurement results. The OFCG inside the TV chamber was modeled (left hand side) and the temperature distribution was simulated (right hand side).

Simulation and measurement results are compared in figure 7.10.

7.4.2. Thermal-Vacuum Test Results

In order to maximize thermal coupling by radiation, the OFCG was coated with *Nextel® Velvet Cording 811*, a matte black paint that is vacuum proven with an emission coefficient of 0.9 [107]. The control unit and the measurement equipment are located outside the TV chamber, because only the laser head is under test. All electric cables and optical fibres are connected to the control unit

by means of dedicated vacuum tight feed throughs.

Repetition Rate Several thermal cycles in the temperature range between 280 K and 320 K are performed. This thermal cycling is not carried out according to the definition in the ECSS standard (see also 6.1.2) because it is not aimed for qualification of the OFCG. The idea of these test series is to identify the sensitivity of the OFCG's repetition rate due to variation of the temperature inside the chamber. During thermal cycling, the repetition rate of the OFCG output changes due to:

- Refractive index change of the optical fiber,
- Length change of the optical fiber,
- Length change of the free-space optical path length due to length change of the aluminum housing.

All three effects result in an indirect proportionality of repetition rate f_{rep} and temperature T. The measured gradient of the repetition rate of Laser-1 in figure 7.6 has been linearly interpolated to

$$\frac{dfrep}{dT} = -937\frac{Hz}{K}. \tag{7.3}$$

For calculating the repetition rate, following formula has been derived:

$$f = \frac{1}{T} = \frac{1}{T_{fiber} + T_{free}} = \frac{c}{n_T \cdot s_{fiber} + n_T \cdot s_{free}} \tag{7.4}$$

wherein s_{fiber} and s_{free} are the lengths of the resonator fiber and the free space optics respectively. The temperature dependent refractive index of the fiber is

$$n_T = n_{fiber,0} \cdot (1 + \alpha_n (T - 293K)), \tag{7.5}$$

wherein α_n stands for the thermal expansion coefficient of the optical fiber. Linear Taylor approximation [143] yields the final equation of temperature dependent repetition rate:

$$f_{rep}(T) = f_{rep,0} - c\frac{\left(n_{fiber,0}s_{fiber,0}\left(\alpha_n + \alpha_{fiber}\right) + n_{air}s_{free,0}\alpha_{alu}\right)}{\left(n_{fiber,0}s_{fiber,0} + n_{air}s_{free,0}\right)^2}(T - T_0) + \mathrm{O}\left(T^2\right)$$

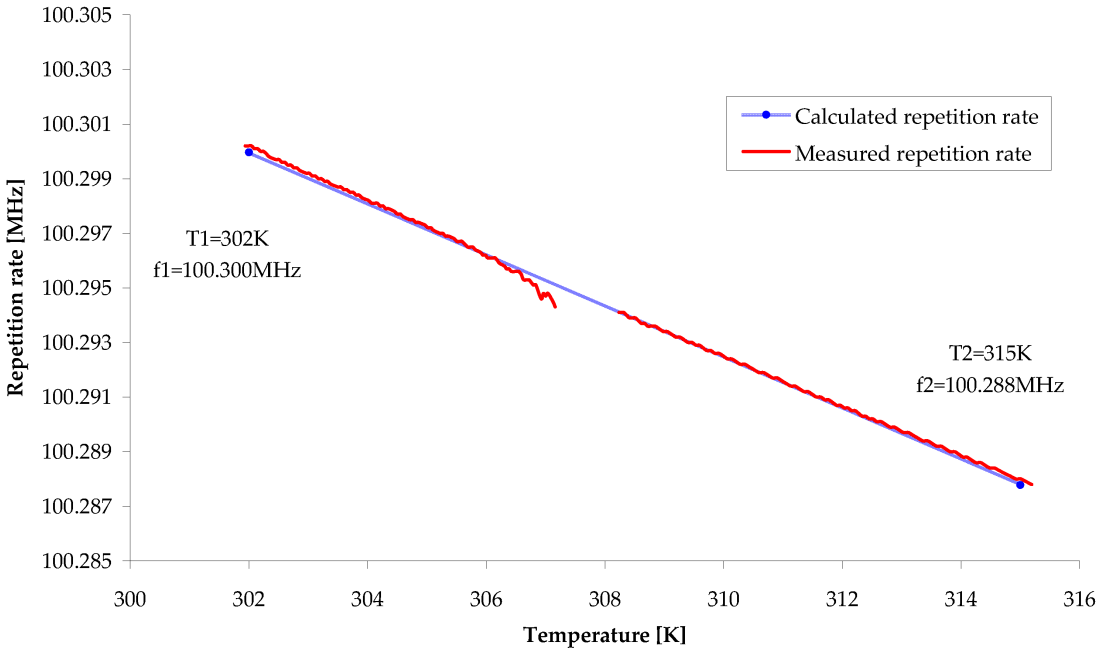

Fig. 7.6.: Variation of repetition rate during thermal cycling. At a temperature around 307.5 K, the laser lost its mode-lock state which results in a lack of measurement points for the repetition rate. After a certain time, a new mode-lock state was found.

(7.6)

An error estimation of the higher order residual term results in

$$\sigma\left(\mathrm{O}\left(T^2\right)\right) = \frac{1}{2!}\left(\frac{\partial^2 f(T)}{\partial T^2}\right)_{T=\xi}(T-293K) < 1\cdot 10^{-2}\frac{Hz}{K} \quad for \quad (T_0 < \xi < T)\,. \tag{7.7}$$

Inserting all measurement values allows the calculation of the repetition rate to

$$\frac{\Delta f(T)}{\Delta T} = 937\frac{Hz}{K} \pm 1\frac{Hz}{K} \tag{7.8}$$

which lies within the measurement accuracy.

Equation 7.6 allows to calculate the repetition rate change for a occurring temperature deviation. Thereby an OFC can be designed with a suitable control actuator that is able to control f_{rep} within a given temperature range.

Optical Output Spectrum During thermal cycling in the thermal vacuum chamber, the optical output spectrum of Laser-1 alters as shown in figure 7.7. A continuous-wave (cw) peak occurs in the spectrum that is temperature dependent. Since mode-locking is based on non-linear polarization rotation, a change of the refractive index of the fiber due to temperature variations results in a degradation of mode-locking performance. The position of all waveplates (see also section 4.4.2) stays constant although the linear polarization angle rotates due to the Kerr effect. This gives rise to cw light passing the artificial saturable absorber.

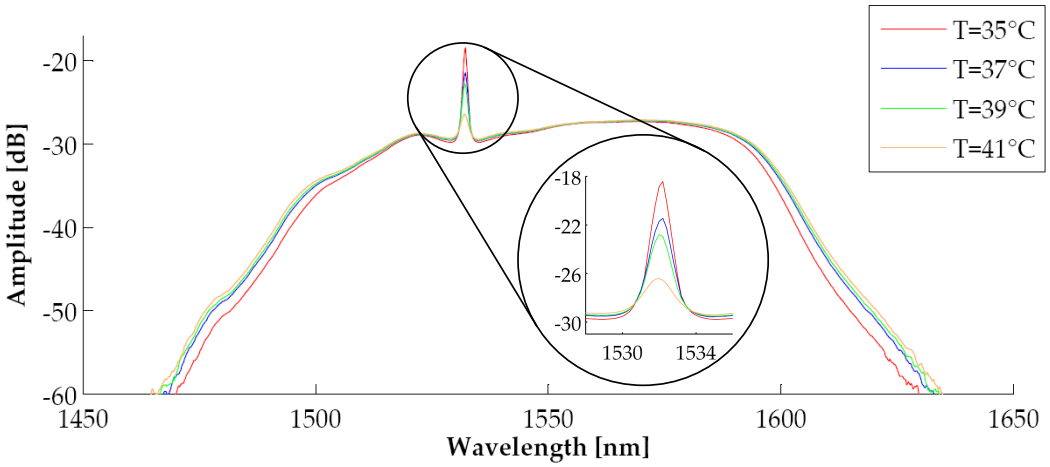

Fig. 7.7.: Optical output spectrum of Laser-1 during thermal cycling. A cw-peak occurs due to changes of the refractive index of the fiber.

The output spectrum of Laser-2 remains unchanged in terms of spectral shape but shifts to higher wavelengths as the temperature rises. According to the manufacturer of Laser-2, an internal power stabilization loop is responsible for this behavior. The absence of cw-peaks demonstrates the suitability of SESAM based mode-locking for environments with varying temperature.

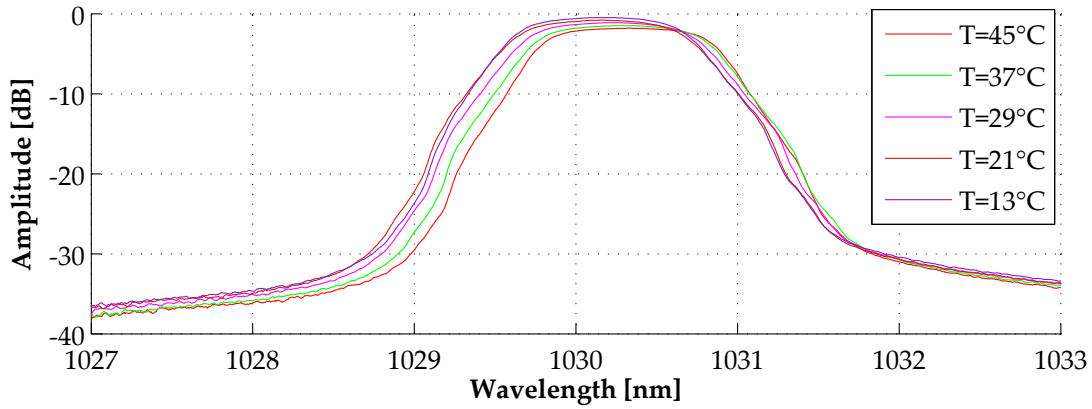

Fig. 7.8.: Optical output spectrum of Laser-2 during thermal cycling. The shift is due to an internal optical output power stabilization.

Optical Autocorrelation Function In order to determine the pulse duration in the time domain, an optical autocorrelator was used. Figure 7.9 shows the measured ACF for different temperatures according to figure 7.7. Corresponding cw-peaks yield a pulse broadening as expected.

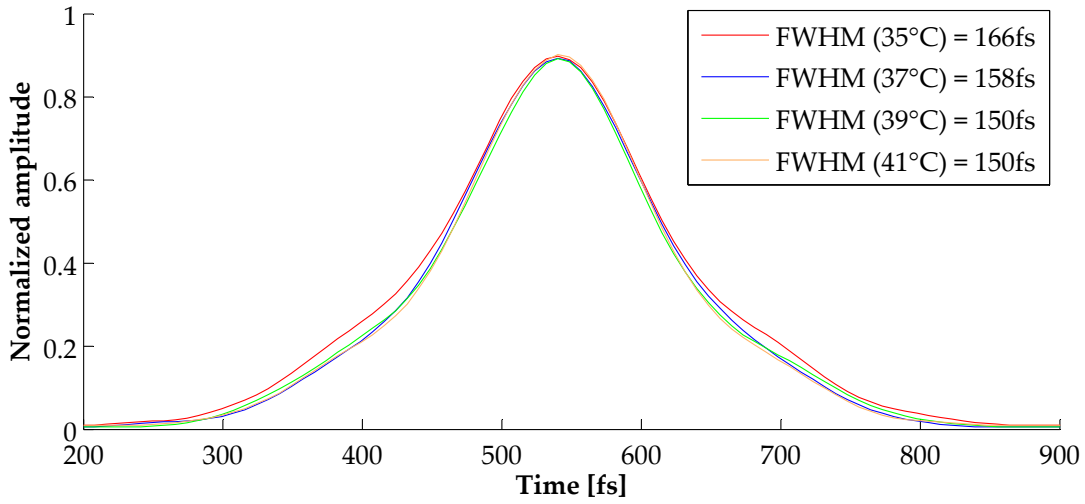

Fig. 7.9.: Duration of optical output pulses of Laser-1 during thermal cycling.

7.4.3. Thermal-Vacuum Test Evaluation

The TV-tests revealed that the NLPR mode-locking is more sensitive to temperature varying environments than SESAM soliton mode-locking. An overall agreement between simulation and measurement results below ±0.2 K was achieved as shown in Figure 7.10.

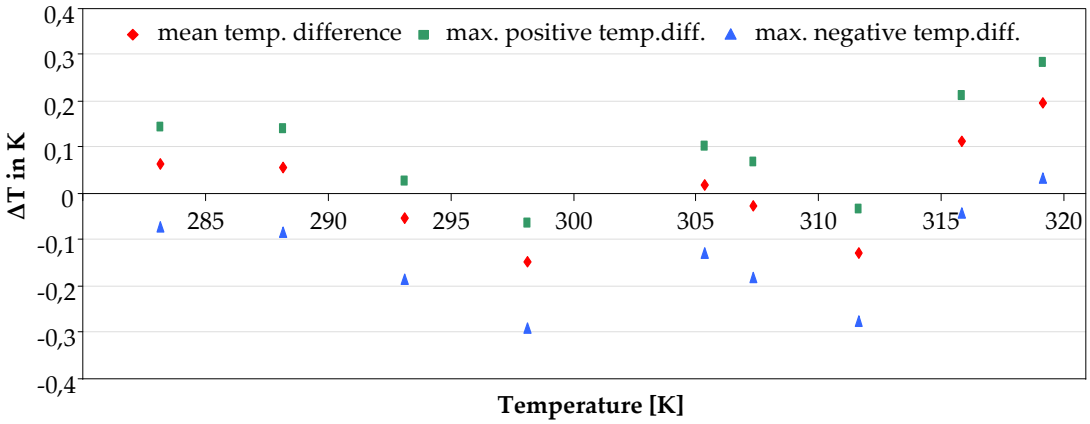

Fig. 7.10.: Simulation and measurement results of TV-tests agree within a temperature difference of ±0.2 K.

7.5. Gamma Radiation Testing

In order to identify the sensitivity of the most critical optical components inside the OFCG [129], a radiation test series was performed using a Cobalt-60 gamma radiation source. The dose rate was constant at a value of 0.01 Gy/s throughout the tests, whereby 3.6 krad of total dose are applied to the devices under test (DUT) within one hour. Lead blocks were used to shield the surrounding equipment; thereby it was made sure that radiation damage only occurs in the DUT. Four different types of fibers were used throughout the tests:

- **Er**
  This type of Erbium doped fiber is the same that is implement within Laser-1.

- **Er-2**
  This type of Erbium doped fiber is hydrogen loaded. It was provided by the fiber optic research center (FORC) in Moscow [198].

- **Er-3**
  This is the same type of Erbium doped fiber as Er-2 but without hydrogen loading. It was also provided by FORC and allows to identify the effect of hydrogen loading by comparing the results gained with Er-2 results.

- **Yb**
  This type of Ytterbium doped fiber is the same that is implement within Laser-2.

For every test a new fiber of each type was implemented in the corresponding test setup. The lengths of the fibers were made equal to lengths used inside the lasers to approximately 0.8 m. Furthermore, verification measurements before and after each test were carried out in order to make sure that the measurement setup remained unaltered.

7.5.1. Amplified Spontaneous Emission Test

Amplified spontaneous emission (ASE) is generated when a laser gain medium is pumped to produce population inversion [151]. In these tests, the pump diode emitted light at 980 nm. The rare-earth doped fibers were used as gain media. Since ASE, in contrast to stimulated emission, does not show a preferred direction, its power is measured in backward direction (see Figure 7.11). The spectrum of the transmission is measured by an optical spectrum analyzer at the fiber output. Figures 7.12 and 7.13 show the ASE test results of the Er and Yb doped fibers. A detailed ASE test result summary is given in table 7.3.

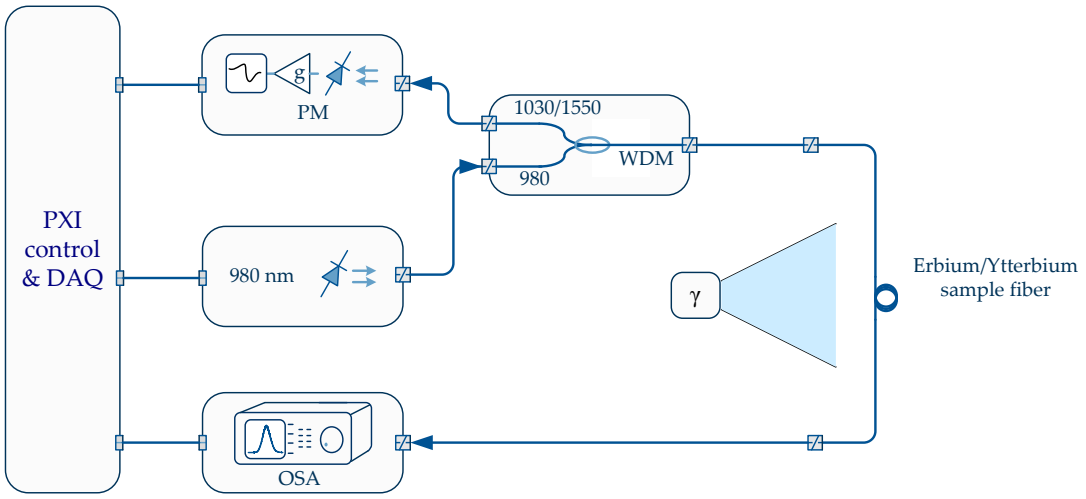

Fig. 7.11.: ASE setup for radiation test of fibers. The gain fibers are pumped by a 980 nm single-mode laser diode. The ASE is measured in backward direction with a power meter, an OSA measures the output spectrum.

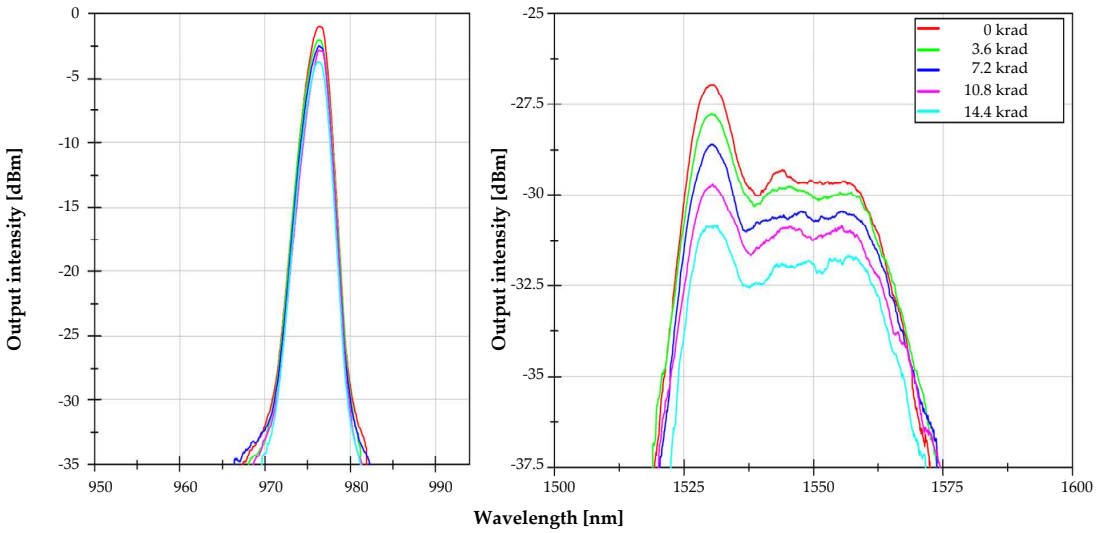

Fig. 7.12.: Measurement of output spectrum during irradiation of the Er fiber. The unconverted pump power at 980 nm and the lasing wavelength at 1550 nm are shown.

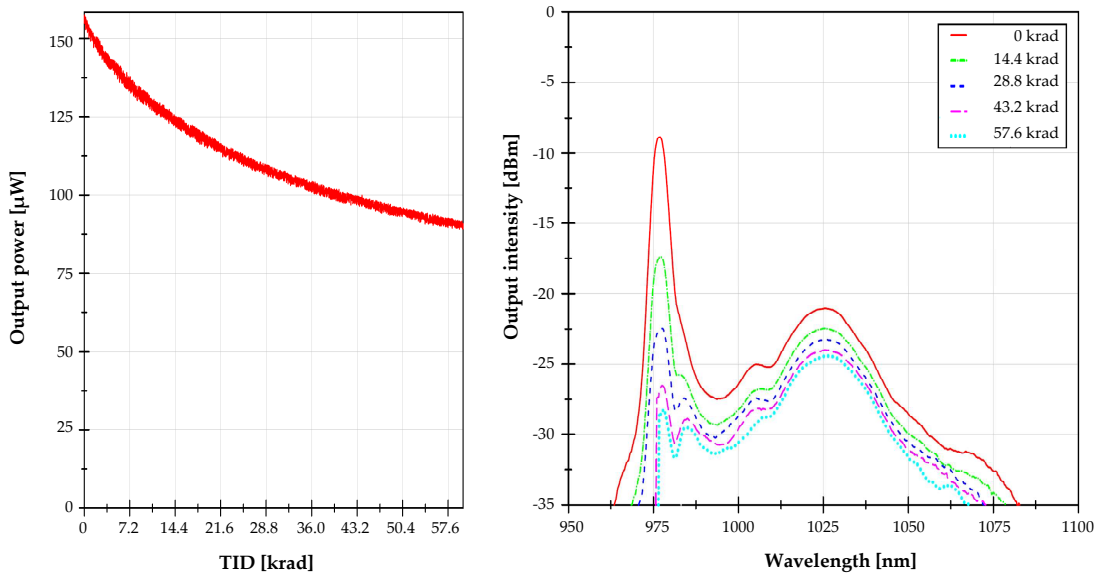

Fig. 7.13.: Measurement of output power and spectrum during irradiation of the Yb fiber.

The Er fiber of Laser-1 shows the highest degradation of 2.5% per krad of total dose. The results for Er-2 and Er-3 fibers prove the radiation hardening due to hydrogen loading. The Yb fiber shows losses that are by a factor of three lower than for the Er fiber.

Tab. 7.3.: Summary of fiber radiation test results using the ASE setup.

Fiber	Power Start	Power Stop	Irradiation time	Total dose	Degradation
Er	125 µW	86.00 µW	4h	14.52 krad	2.15 %/krad
Er-2, H_2-loaded	28.40 µW	25.50 µW	16h	57.60 krad	0.2 %/krad
Er-3, Unloaded	71.8 µW	7.70 µW	16h	57.60 krad	1.5 %/krad
Yb	157 µW	89.0 µW	3h	59.45 krad	0.72 %/krad

7.5.2. Amplifier Radiation Test

A setup shown in figure 7.14 was used to identify if there are radiation effect differences between pulsed and cw operation (ASE test). Laser-1 and Laser-2

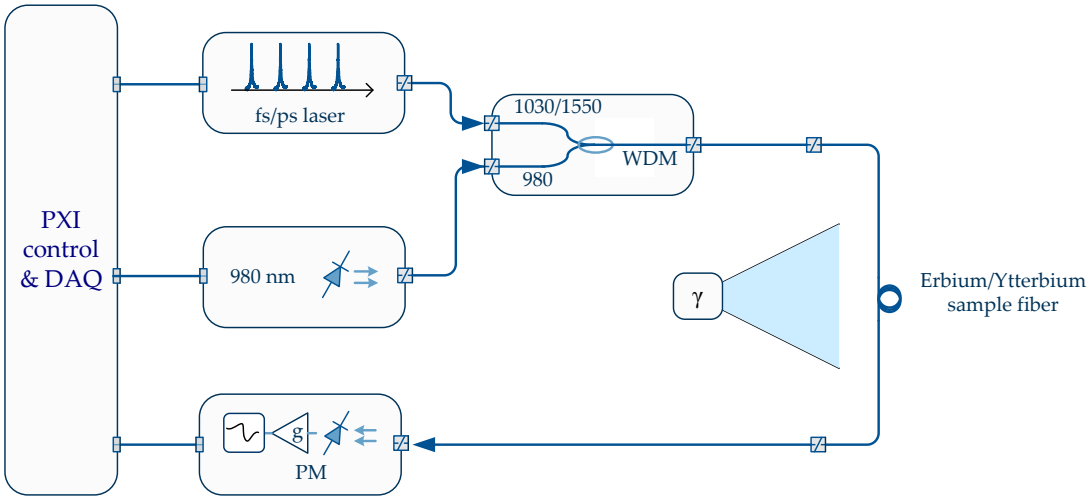

Fig. 7.14.: Amplifier setup for radiation test of fibers. The gain fibers are pumped by a 980 nm single-mode laser diode and seeded by the wavelength corresponding ultra-short pulsed laser.

where used as seeders during the respective radiation tests.

Figure 7.15 shows the powermeter measurement results in dependence of the dose rate. Fibers Er and Er-3 show higher degradation gradients than the Yb fiber. The hydrogen loaded Er-2 fiber shows a low degradation of 0.15% per krad.

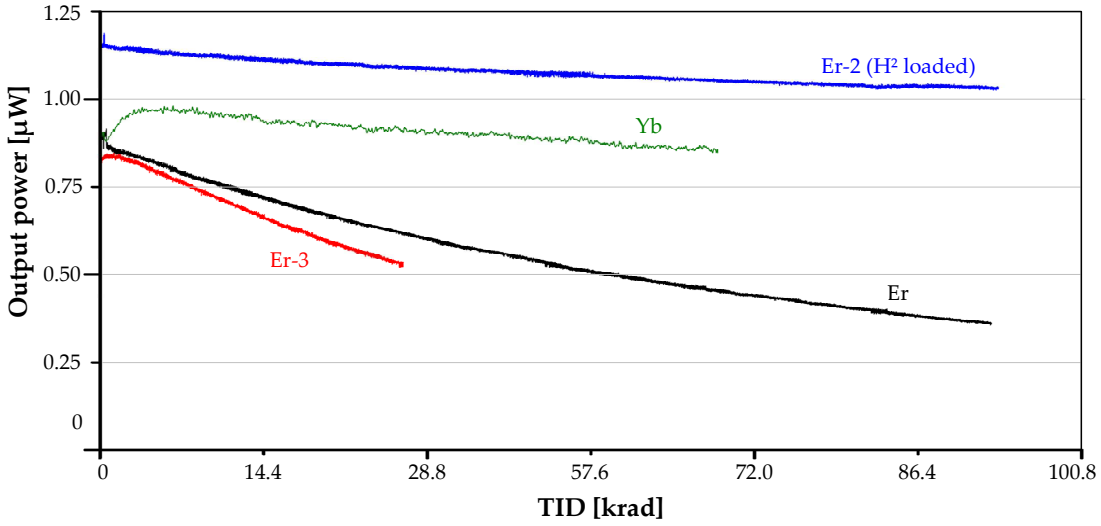

Fig. 7.15.: Optical output power of the different tested fiber samples during irradiation.

Tab. 7.4.: Summary of fiber radiation test results using the amplifier setup.

Fiber	Power start	Power stop	Irradiation time	Total dose	Degradation
Er	870 µW	357 µW	22.5 h	81 krad	0.72 %/krad
Er-2, H_2-loaded	1.17 mW	1.03 mW	22.75 h	81.8 krad	0.15 %/krad
Er-3, Unloaded	830 µW	597 µW	7.6 h	27.6 krad	1.02 %/krad
Yb	978 µW	875 µW	15.35 h	48.1 krad	0.23 %/krad

The Er fiber shows by a factor of three higher radiation damage than the Yb fiber. The unloaded fiber Er-3 shows the highest losses (1.02% per krad).

7.5.3. Laser Radiation Test

The laser gain fibers Er and Yb are radiation tested during operation of the OFCG. Figure 7.16 shows the measurement setups for Laser-1 and Laser-2. Additionally the SESAM of Laser-2 was tested in a separate test sequence in

order to determine its behavior under irradiation. The test results of this setup directly simulate the application of an OFCG under radiation environment.

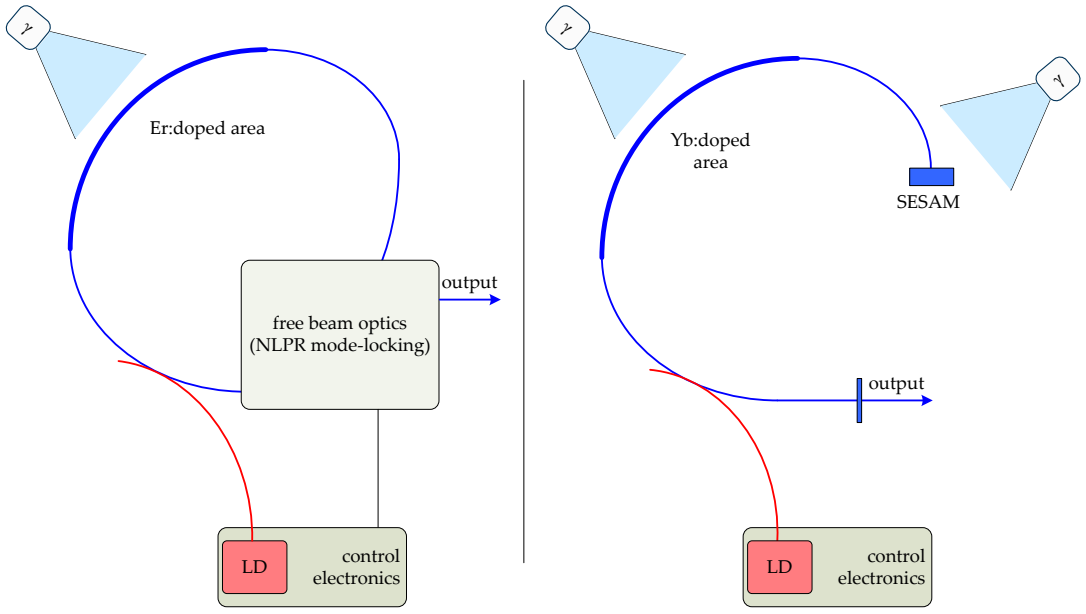

Fig. 7.16.: Laser tests. The Erbium and Ytterbium gain fibers of the lasers as well as the SESAM was irradiated during operation of the lasers.

Figures 7.17 and 7.18 show the test results for the Er fiber in Laser-1 and the Yb fiber in Laser-2 respectively. Occurrence of cw-peaks under irradiation in the spectrum of Laser-1 indicates a refractive index change of the Er fiber. The Yb fiber of Laser-2 shows moderate losses of 0.082% per krad for a total dose of more than 156 krad.

After the Er fiber of Laser-1 was uncovered, the laser started a 20 minutes mode-lock search until a stable state was found. After a total dose of approximately 28.8 krad, Laser-1 lost its mode-locked state and started to search for a new one. Since the optical output power had decreased, a new mode-lock state with the parameters set in the control software was not found.

Figure 7.19 shows the results for the SESAM. After several krad of total dose the SESAM improved its behavior but lost this improvement again after approximately 20 krad. At the end of the test, the SESAM achieved its initial

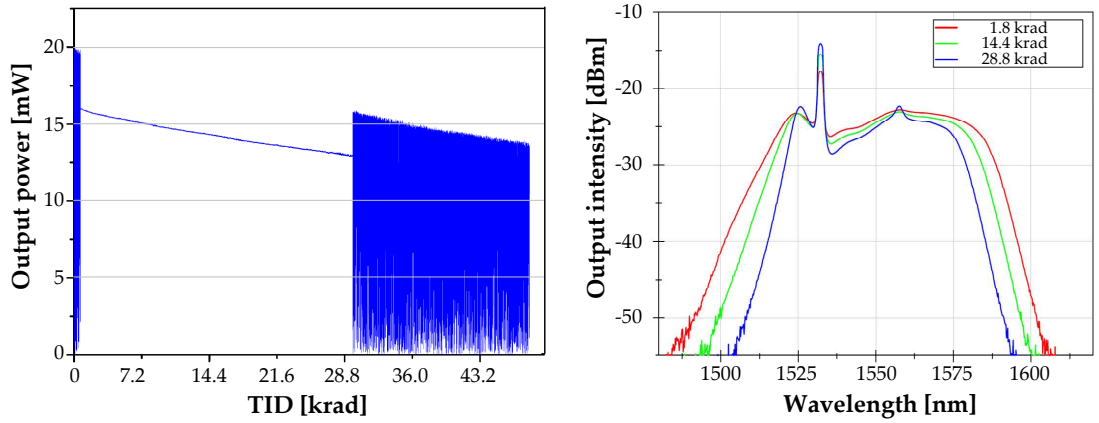

Fig. 7.17.: Irradiation of the Erbium fiber mounted in Laser-1 results in a degradation of approximately 0.7 %/krad optical output power and narrowing of the output spectrum.

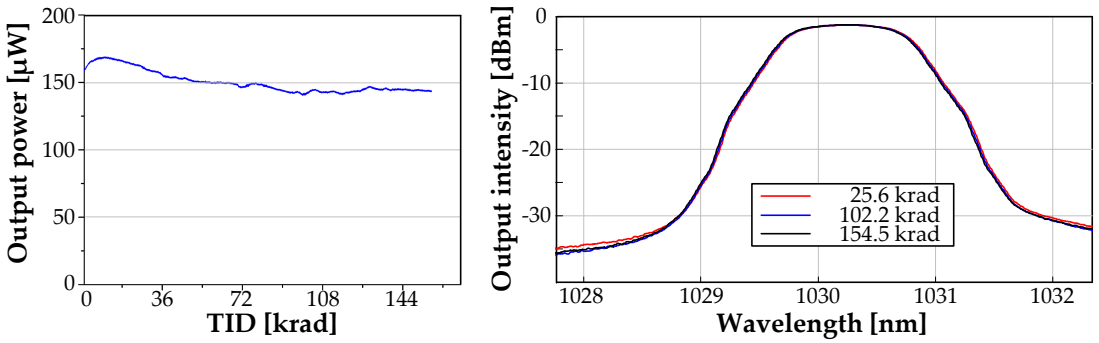

Fig. 7.18.: Irradiation of the Ytterbium fiber mounted in Laser-2 shows a degradation of 0.08 %/krad of output power, the spectrum stays constant.

performance.

The laser test results are summarized in table 7.5.

7.5.4. Radiation Test Summary and Evaluation

Varying degradations between the different tests suggest the occurrence of photo-bleaching [81]. As soon as high intense light pulses propagate through the fiber under irradiation, the degradation of transmission loss is decreased by a factor of three compared to cw-light ASE test. High intense light of ultra-short

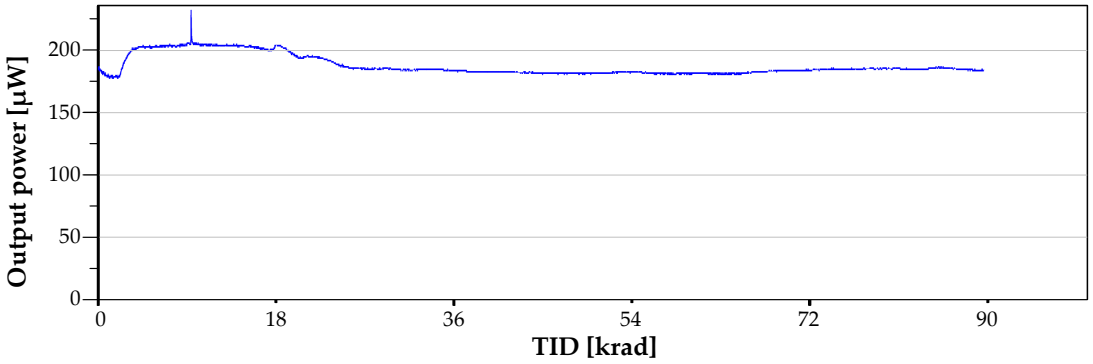

Fig. 7.19.: Irradiation of the SESAM mounted in OFCG-2 shows no overall degradation of output power.

Tab. 7.5.: Summary of fiber and SESAM radiation test results using the laser setup.

Irradiation sample	Power start	Power stop	Irradiation time	Total dose	Degradation
Er	15.97 mW	12.93 mW	7.8 h	28.5 krad	0.67 %/krad
Yb	170 µW	148 µW	43.4 h	156.2 krad	0.082 %/krad
SESAM	184 µW	184 µW	24.9	89.6 krad	0 %/krad

pulses thereby cures the F-center defects.

The Ytterbium doped fiber of Laser-2 is by a factor of three more radiation insensitive than the Erbium doped fiber of Laser-1. The lowest radiation sensitivity is achieved by hydrogen loading of Erbium fibers which is demonstrated by comparison of Er-2 and Er-3 results. This type of fiber treatment should be used for further development of a space-borne OFCG.

8. Development of Optical Fiber Sensing for Space Applications

Within this chapter the development of optical fiber sensing for applications in space is summarized. A trade-off between different interrogation principles is carried out in section 8.1. The interrogation principle of the selected scanning laser technology is described in section 8.2. The architecture of the interrogator hardware is illustrated in section 8.3. Characterization of the scanning laser interrogator which needs to be performed prior to the operation of the system is explained in 8.4. The development of the soft- and firmware of the sensing system is summarized in section 8.5 and test results are outlined in section 8.6.

8.1. OFS Interrogation Technology for Space Applications

Fiber optic sensing is on the way towards its utilization for space applications. The advantages of optical sensors like Fiber-Bragg Gratings (FBG) are desired in space applications: Lightweight, insensitivity to electro-magnetic disturbances, ease of distribution and scalability are natural properties of fiber optic sensing and requirements to a sensor system of a space craft. The possibility to implement several FBG sensors in one single sensor fiber without influencing each other and to install such fibers in composite materials during their fabrication are also desirable for space systems.

Launchers (e.g. Ariane) and satellites are currently monitored by hundreds of electric sensors during test and qualification. Fiber optic sensing is regarded as a potential technique to overcome limitations of recent monitoring systems.

Instruments based on tunable lasers are established devices for demodulation of

fiber optic sensors. These state-of-the-art systems built on tunable laser sources often use free beam setups for wavelength tuning. Thus they are sensitive to environmental influences like vibration or temperature impacts. The sensor interrogation system developed in this work is based on an electro-optically tunable laser diode. This is a monolithic device and therefore insensitive to vibration loads. By using fiber coupled photo detectors for input intensity measurement, none of the subcomponents is sensitive to environmental disturbances, provided that the laser diode is adequately temperature controlled.

Regarding their implementation on-board spacecrafts, the interrogation techniques summarized in table 8.1 show different advantages and drawbacks. A spectrometer based system has already been developed in an ESA funded project (see Annex A.1) and therefore shows the highest technological maturity among the alternative designs. The edge-filter system is the most promising candidate when high measurement rate for e.g. vibration sensing is required. The disadvantage of the edge-filter approach is the fact that the design wavelength of the sensor must match the crossing point of the edge filters. This also implies that for every sensor a pair of edge-filters combined with two photo detectors is required which results in a complex setup.

The scanning laser (SL) approach features the most compact and robust setup. This all-in-fiber setup is robust against vibrational influences and thereby alignment free. The overall number of sensors does not influence the interrogator design as long as the number of measurement channels stays constant. Furthermore, the system is scalable to high numbers of sensors by keeping the system complexity low. Although the overall measurement rate decreases with rising number of sensors (see formula 8.11), the achievable measurement rate due to the developed peak-tracking algorithm is still compliant to the requirements on-board spacecrafts (see section 8.5.2).

Tab. 8.1.: Trade-off between OFS interrogation technologies. The majority of requirements for sensing on-board a spacecraft is fulfilled by the scanning laser interrogation technology.

Requirement	Spectrometer Interrogator	Edge Filter Interrogator	Scanning Laser Interrogator
Technological maturity	High	Medium	Medium
Robustness of setup	Medium	High	High
Compactness of setup	Low	Medium	High
Service-free operating time	High	High	High
Operational lifetime	High	High	High
Power efficiency	Medium	Medium	High
Measurement performance (accuracy and rate)	Low	High (suitable for strain sensing)	Medium
Number of sensors / complexity of system	Medium	Low	High

8.2. Scanning Laser Interrogation Principle

During this work an interrogator based on a tunable laser diode has been developed where laser pulses at rising wavelengths are emitted as pulse train. Reflected intensities are recorded and similar to spectrometer based interrogators, a centroid algorithm is used to calculate the mean wavelength of the sensor response. Figure 8.1 outlines the measurement principle of the scanning laser interrogation system.

The SL interrogator is based on a tunable laser that is capable of providing discrete wavelengths within its available spectrum from 1528 nm to 1571 nm as described in section 5.4. The hardware architecture (section 8.3) of the SL interrogator results in a very flexible and adaptable system. The main advantage is the wavelength switching capability compared to standard interrogators of

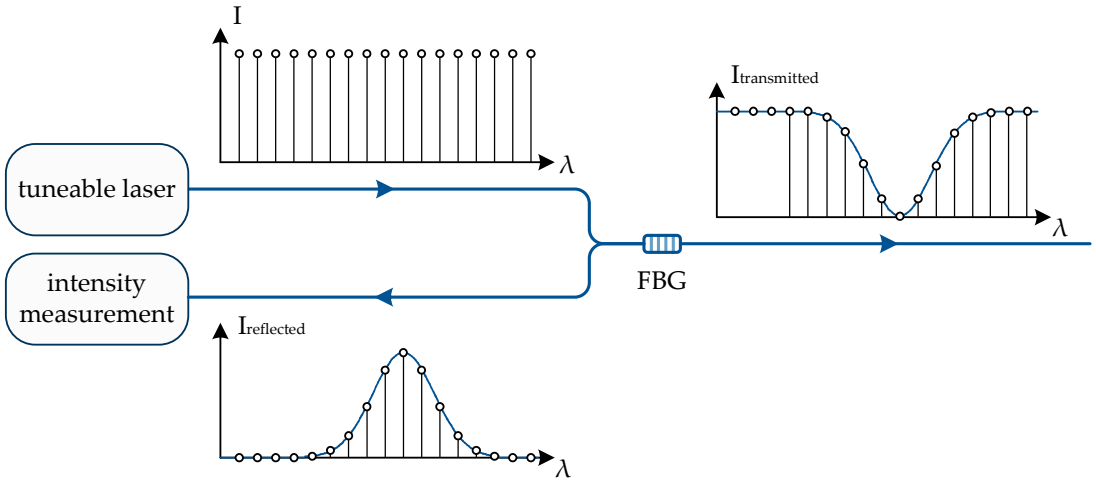

Fig. 8.1.: The scanning laser system emits laser pulses at ascending wavelengths. Pulses of which the output wavelengths match the design wavelength of the FBG sensor are partially reflected. The sensor response is determined by measurement of the reflected intensities.

the same measurement principle [50]. Since every wavelength within the output spectrum of the MG-Y laser diode is accessible within the same switching time on microsecond timescale, spectral areas without information can be omitted during standard operation (see section 8.5.2) and each sensor can be measured individually. Spectral gaps between two consecutive sensors can thereby be skipped and overall measurement rate is increased. Further possibilities are the adaption of measurement rate in order to implement priority to the sensor read-out order. Important sensors that detect fast varying strain could for example be read out more often than sensors that measure slowly varying temperatures.

In order to detect the peak wavelength of fiber Bragg grating (FBG) sensors, the SL is able to scan through a spectrum in the infrared region with a width of more than 40 nm. A sensor array can be connected to one measurement channel by implementing several sensors with different design wavelengths inside one sensor fiber. The SL interrogator searches for the sensor responses and is then able to interrogate user chosen sensors sequentially. The magnitudes of the reflected intensities depend on the actual sensor position that is determined by the measurand (e.g. temperature). One single sensor is scanned by a variable number of spectral sampling points and the spectral answer of the sensor is then calculated by centroid algorithms. Depending on the spectral width of one

sensor, the number of sensors that shall be interrogated and the required sampling points per sensor, a maximum sampling frequency of 10 kHz is achievable with the SL interrogator .

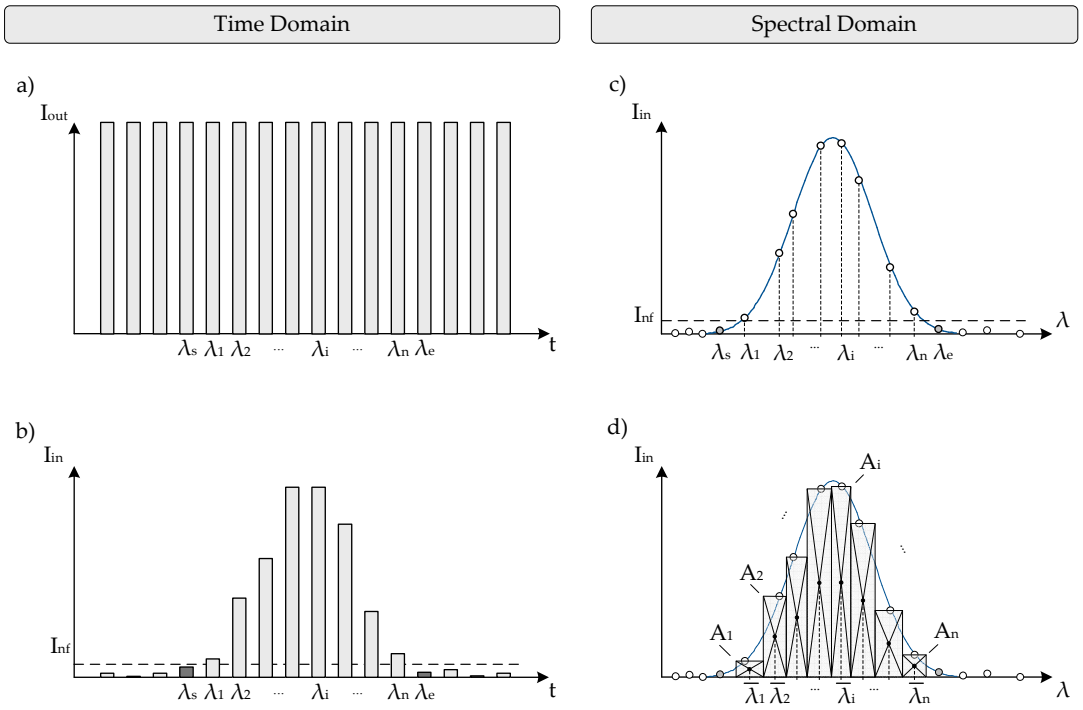

Fig. 8.2.: Time and wavelength domain of one FBG sampled by a variable number of sampling wavelengths. Due to a measurand change, the sensor answer is spectrally moving to higher or lower wavelengths. The special centroid algorithm (SCA) determines the mean wavelength of the sensor response.

In order to determine the current spectral position of a FBG sensor, the spectrum is scanned with laser pulses generated by the MG-Y laser diode. Therefore the SL generates a sequence of output laser pulses according to the DAC values stored in the LUT. This results in a train of laser pulses (Figure 8.2-a), wherein succeeding pulses show rising wavelengths. Actually, the laser emits light continuously and not as pulses, but in terms of laser wavelengths a pulse train occurs. When the wavelength matches the design wavelength of a FBG sensor, the emitted light is partially reflected by the FBG and guided back to the photo detector of the corresponding channel. The FPGA that evaluates these input

intensities compares measured intensities with a user defined noise floor level in order to distinguish between sensor responses ($I_{in} > I_{nf}$) and noise coming from background light or from the electronics of the photo amplifiers ($I_{in} < I_{nf}$). Figure 8.2-b shows a typical sensor response. The two intensities lower than the noise floor at the edges of the sensor response enframe the spectrum of the sensor peak. The wavelengths corresponding to these two intensities are entitled λ_s and λ_e as they are used as start and end point for sensor sampling by the Peak-Tracking algorithm explained in section 8.5.2.

The respective sensor response in the wavelength domain is shown in figure 8.2-c. Since the wavelength are non-equidistantly distributed in the spectrum (see also section 8.4), the number of sample points per sensors may vary, when the sensor shifts spectrally due to measurand changes.

Sensor Evaluation by Centroid Calculation

The mean value of the sensor response can be evaluated in many ways. The wavelength of the maximum or the start and end intensities (see figure 8.2) could for example be defined as mean value of the sensor response. Gaussian fitting can also be used for determination of the sensing value. In the case of the SL interrogator, a special centroid algorithm (SCA) is implemented that evaluates the center of the area beneath the envelope of the sampling points. This algorithm has been developed for the SL interrogator and takes into account the issue of non-equidistant sampling. Comparable to the standard centroid algorithm, squares are generated for approximation of the areas. The difference is that the width of the squares are adapted to the different wavelength distances. Thereby the area is fit more accurately (see also figure 8.34).

Interim wavelengths in the middle between two consecutive sampling wavelengths are introduced for generation of squares to apply the SCA. The centers of these squares A_i determine the virtual sampling wavelengths $\bar{\lambda}_i$ that are weighted by the size of the corresponding squares (figure 8.2-d). Using the notation given in figure 8.2, the virtual sample wavelengths $\bar{\lambda}_i$ result in

$$\bar{\lambda}_i = \frac{\lambda_{i-1} + 2\lambda_i + \lambda_{i+1}}{4}. \tag{8.1}$$

The areas A_i of the squares are given by

$$A_i = \frac{\lambda_{i+1} - \lambda_{i-1}}{2} I_i. \tag{8.2}$$

This results in the centroid wavelength λ_S of the evaluated sensor of

$$\lambda_S = \frac{\sum_{i=1}^{n} \bar{\lambda}_i A_i}{\sum_{i=1}^{n} A_i}. \tag{8.3}$$

The indexes $i-1$ and $i+1$ of formulas 8.1, 8.2 and 8.3 have to be replaced by s respective e if the first and the last values of the sensor response have to be determined.

8.3. Hardware Architecture of Scanning Laser Interrogator

The scanning laser (SL) interrogation system consists of several subsystems according to Fig. 8.3. An embedded box PC controls the scanning laser that itself is comprised of three sub-elements: Control and data acquisition unit (CDU), laser and detection unit (LDU) and fiber coupler unit (FCU). Optical fiber connectors allow to adapt the system to different optical sensor networks. The embedded box PC accommodates all other scanning laser hardware, thereby the overall system has only a volume of 30 x 20 x 12 cm^3.

The CDU is in charge of the generation and adjustment of three laser control voltages that are necessary for tuning of the output wavelength. The LDU accommodates the MG-Y laser diode together with three voltage-to-current converters for the control current generation. Furthermore laser diode driver and temperature controller that bias the laser diode are implemented in the LDU. The FCU distributes the light of the laser diode to all three sensor channels and guides the reflected optical measurement signals back to the LDU. Photo-amplifiers (photo detectors combined with variable gain trans-impedance amplifiers) are used for transformation of the photo currents into voltages that are compatible with the input voltage level of the CDU. The measured intensities are evaluated by the CDU and the mean wavelengths are sent to the PC

where they are visualized and stored. The CDU is completely built by electronic components, the LDU is the interface between the optical and the electrical side where else the FCU and the sensor network consist of passive optical components only.

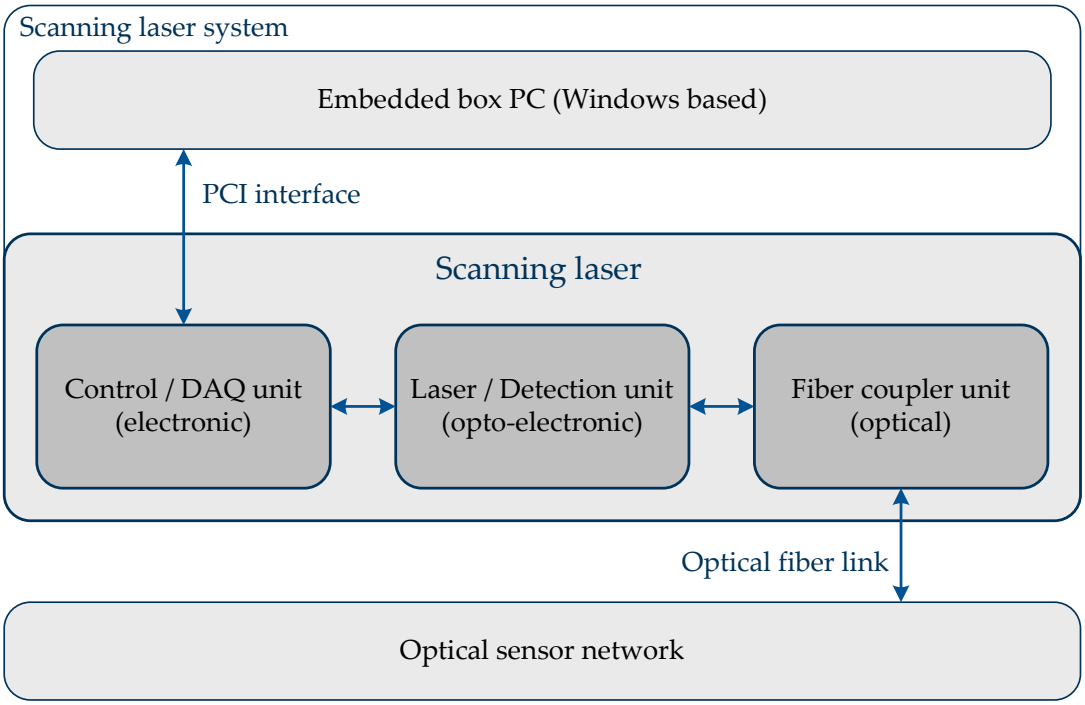

Fig. 8.3.: The scanning laser (SL) system is based on an embedded box PC that accommodates the scanning laser hardware (CDU, LDU and FCU). A sensor network of up to three optical sensor fibers can be connected to the SL interrogator at its current configuration.

8.3.1. Control and Data-Acquisition Unit

The output wavelength of the MG-Y laser diode depends on three input currents. Therefore, three current control loops are implemented within the LDU that lock the control currents to its set values. The CDU is used for generation of three voltages that provide the set points of the current control circuits. The CDU voltages are generated by digital to analog converters (DAC), of which the digital input patterns are set by a field programmable gate array (FPGA).

A memory block (SRAM) holds all necessary bit patterns in form of a look-up table (LUT). A digital signal processor (DSP) commands the FPGA and thereby the analog hardware of the system.

Intensity values (responses of the FBG sensors) are converted to analog voltages by the LDU. Three analog to digital converters (ADC) are used to sample the output voltages of the photo amplifiers of the LDU. The digital values are provided to the FPGA where they are buffered in FPGA internal memory. The DSP polls the FPGA, when a measurement cycle is completed and new measurement data is available. The actual sensor responses are calculated by the DSP with a centroid algorithm and are sent the embedded box host PC.

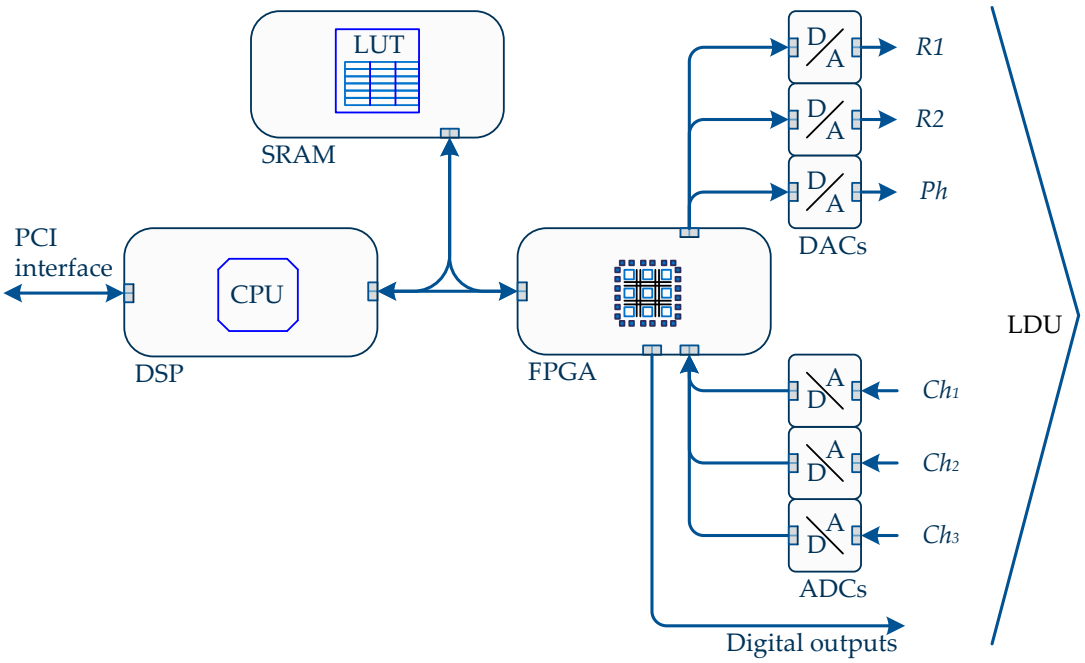

Fig. 8.4.: Overview of control and data acquisition unit (CDU). It basically consists of DSP, FPGA, SRAM, DACs and ADCs.

All of the DAC and ADC devices together require an overall number of 96 bit for input control (three 16 bit DAC devices) and data acquisition output (three 16 bit ADC devices). To allow parallel data streams, an FPGA is implemented which is capable of providing all output data and pick up all input data in parallel. The DSP is best suited for calculation of the centroid algorithm (see section 8.2). The SL hardware has been chosen to yield maximum system

flexibility. If signal filtering (e.g. low-pass filtering) or averaging is required, this can additionally be implemented within the DSP.

8.3.2. Laser and Detection Unit

The core of the SL interrogation system is a MG-Y laser diode of which the technology is explained in detail in section 5.4. Since this laser diode is a monolithic device and the interrogator does not have any free beam optics, the measurement setup is insensitive to shock and vibration loads.

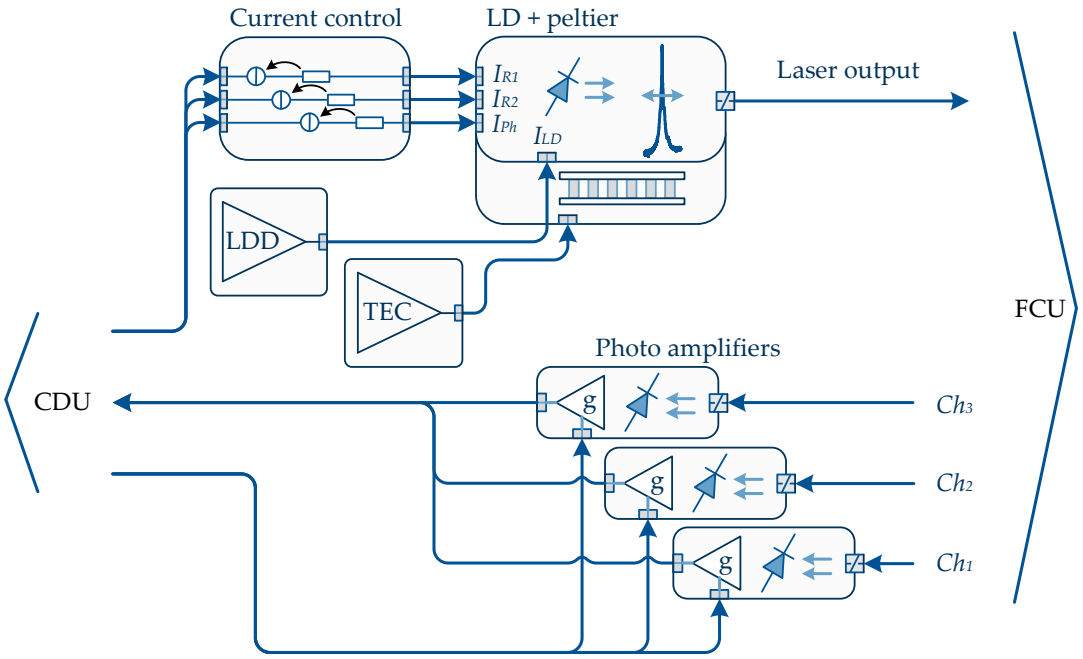

Fig. 8.5.: Overview of control and detection unit (LDU). The MG-Y laser diode is driven and temperature stabilized. The control voltage triplet generated by the CDU feeds the current control and thereby adjusts the wavelength. The input intensities (reflected sensor responses) are transformed into voltages by variable gain photo amplifiers.

The output wavelength of the laser-diode can be adjusted electronically by feeding in two analog currents I_{R1}, I_{R2} into the two grating structures. The injected charge carriers result in a variation of reflected wavelength. A third current I_{Ph} is injected into a common area for phase adjustment. The wavelength cannot

be adjusted continuously due to the principle of wavelength generation based on the vernier-effect (see section 5.4). Only discrete wavelengths, which are not equally spaced in the spectrum of the laser, can be adjusted.

Current Control Circuitry

The output wavelength of the MG-Y laser diode is adjusted by a set of three control currents. Constant carrier injections into the reflection grating sections of the laser branches are achieved that alter the refractive indexes of the reflectors and thereby tune the output wavelength. As long as the resistances of the current input ports are constant, voltages can be applied to the ports that yield constant control currents. Output wavelength tuning is achieved by variation of the input current magnitudes. Varying the input currents leads to variation of the laser temperature (see also section 8.4) whereby the resistances of the control current input ports are altered. In order to provide constant input currents and thereby constant carrier flows into the reflection gratings of the laser, the control currents have to be stabilized. This is achieved by current control circuits (CCC) implemented for each input current as shown in figure 8.6.

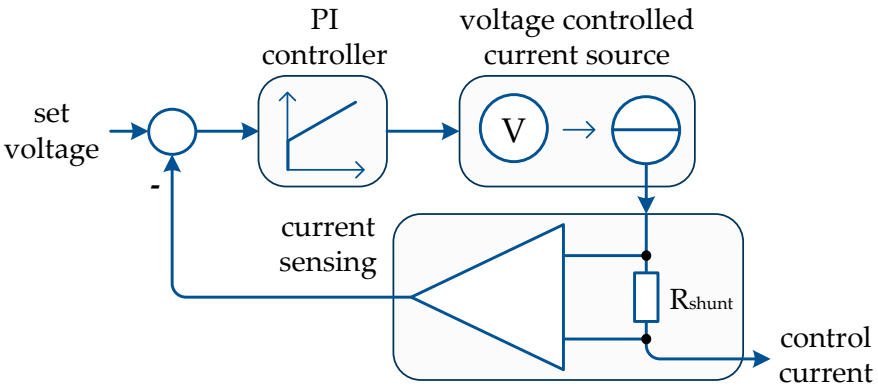

Fig. 8.6.: The current control circuit is used to lock the control current to its set value. Therefore the input voltage is converted to an output current that is kept constant by a feedback loop.

Since the CDU provides analog output voltages as set points for the three laser control currents, conversion into currents has to be obtained by voltage controlled current sources. The actual value of the laser input current is mea-

sured as voltage drop across a shunt resistor by a differential amplifier [92]. Thereby the control variable is transformed into a voltage. This control voltage is subtracted from the set voltage preset by the CDU whereby an error signal is generated. A PI-controller adjusts the voltage controlled current source [164] to adjust the laser control current until the error signal vanishes.

Figures 8.7 and 8.8 show the simulation and measurement results of the CCC.

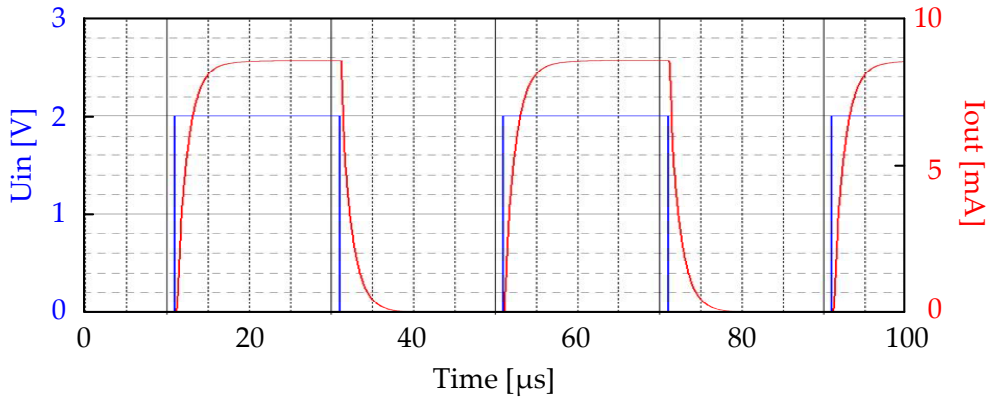

Fig. 8.7.: Simulation of current control circuit using an input voltage U_{in} with maximum amplitude of 2 V and a frequency of 25 kHz.

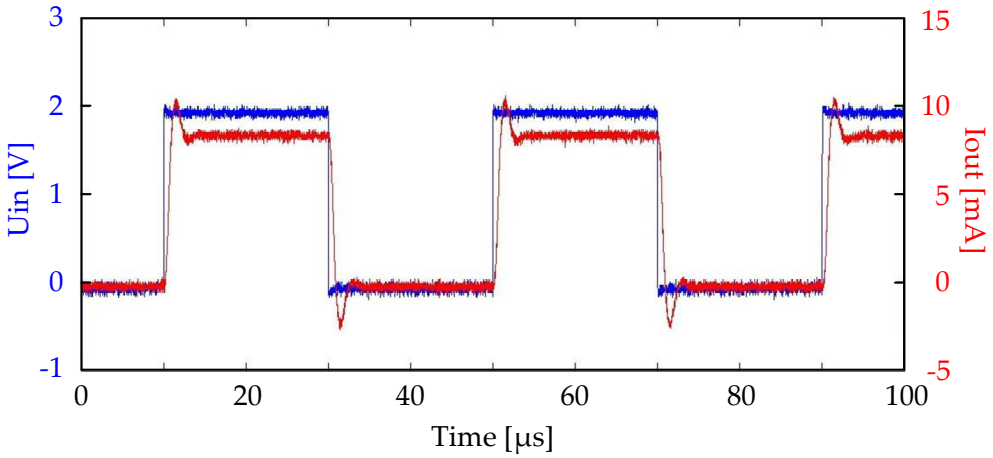

Fig. 8.8.: Measurement of current control circuit using the input voltage U_{in}=2 V at a frequency of 25 kHz.

Switching between zero and maximum common phase current 8 mA is simulated. At a 25 kHz switching frequency of the set voltage U_{in} the rise time for

the output current I_{out} is below 10 μs.

Temperature Controller

The temperature controller (TEC) of the laser diode is based on an integrated circuit of Texas Instrument®). In order to adapt the TEC to the control path consisting of a PWM current control, a Peltier cooler and a thermistor, the frequency response of the TEC circuit has been determined using a frequency response analyzer according to figure 8.9. This measurement device applies a sinusoidal input signal to the PWM current control and measures the resulting output temperature. The result is the transfer function [102] of the control path shown in figure 8.11 as the Bode amplitude and phase diagrams.

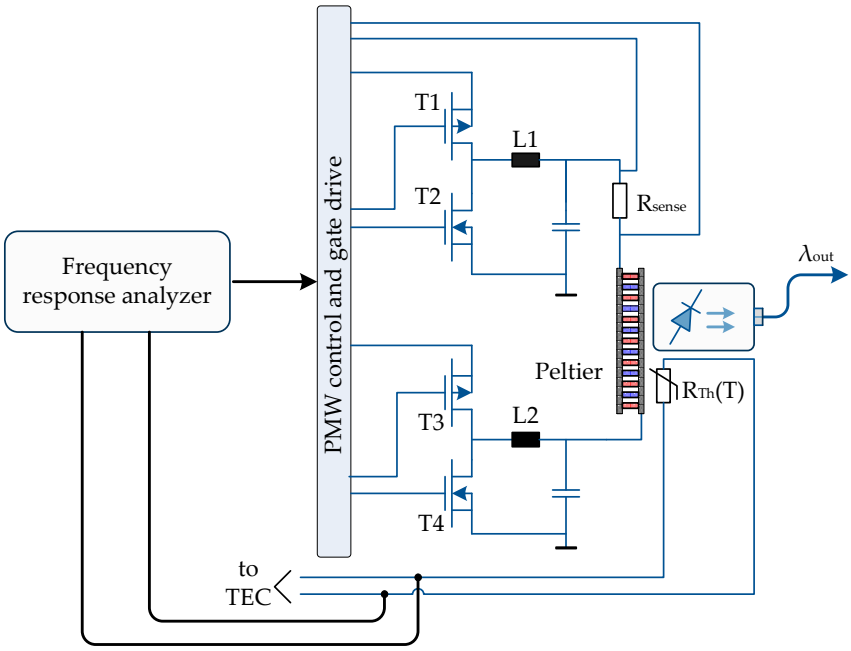

Fig. 8.9.: Frequency response measurement of the TEC circuit.

As shown in Figure 8.10, dimensioning of the PI controller requires the definition of two resistors and one capacitor [15] according to [115]. At 45° phase deviation (see figure 8.11) the I-part K_i takes over the dominant part of the controller, which is at frequency of 0.025 Hz [106].

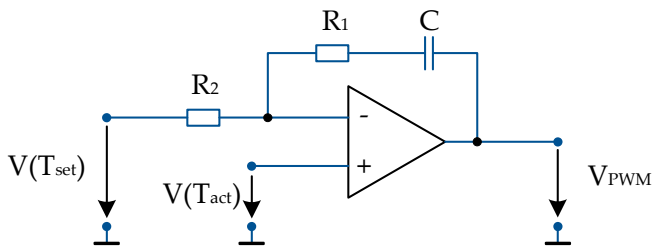

Fig. 8.10.: PI controller based on an operational amplifier used for the TEC circuit of LDU.

For the I-part of the controller, frequency, capacity and resistance are related by the formula

$$K_i = 2 \cdot \pi \cdot f = \frac{1}{R \cdot C}. \tag{8.4}$$

High resistance and capacity values are required in order to reach the low frequency of 25 mHz. Setting the capacity to $20\ \mu F$ results in a resistance of

$$R_2 = \frac{1}{2 \cdot \pi \cdot f \cdot C} \approx 320 k\Omega. \tag{8.5}$$

The P-part K_p of the controller is defined as

$$K_P = \frac{R_2}{R_1}. \tag{8.6}$$

In order to identify the appropriate value for R_1, the crossover frequency, which is set by a phase margin of 50 degrees in our case, is evaluated in the phase diagram of figure 8.11. At the resulting -130 degrees the frequency is 3.5 Hz which in the amplitude plot refers to an amplification of $A = K_p = 15\ dB$. Therefore R_1 according to formula 8.6 is calculated to $R_1 = 1.5\ M\Omega$. These values are used for dimensioning of the PI controller of the TEC circuit.

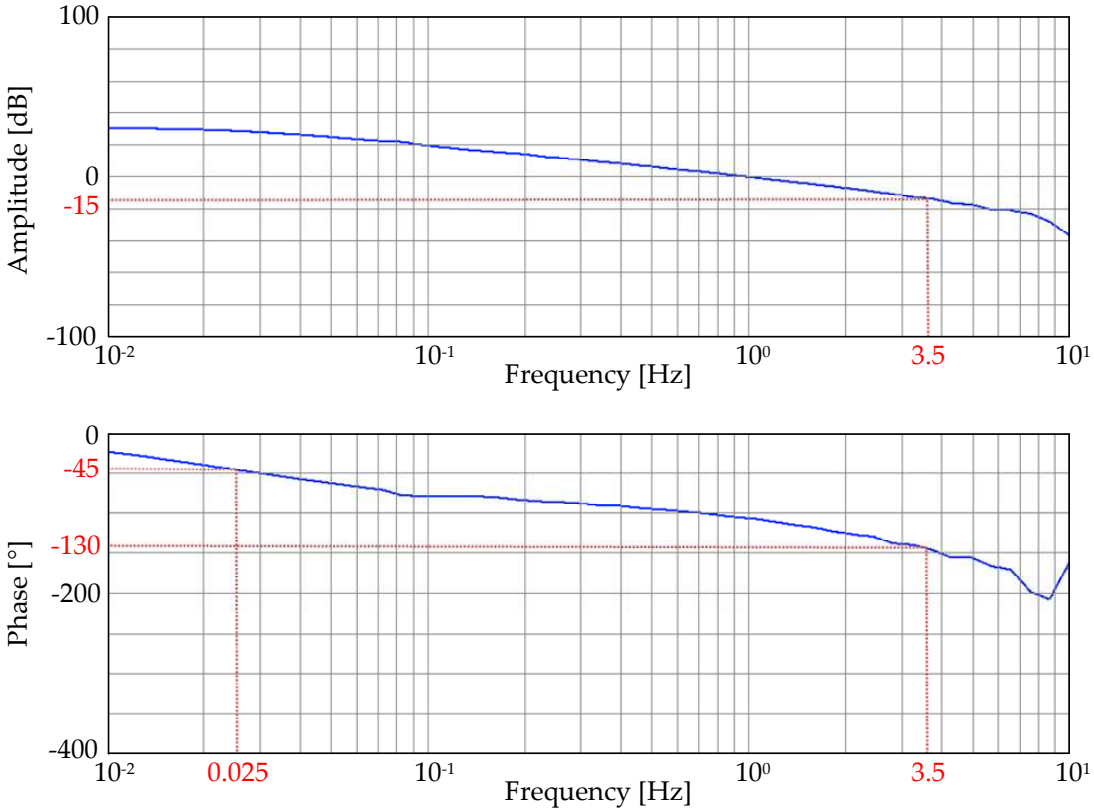

Fig. 8.11.: Bode plot of frequency response measurement of the TEC circuit.

Transimpedance Amplifiers

For data acquisition of the reflected sensor intensities, three fast photo detectors combined with transimpedance amplifiers are used as photo-amplifiers. An inverter and a variable gain amplifier (VGA) adjust the voltage level in the 0 to 2 V range of the DAC [16]. The gain of the VGA is adjusted by a bit pattern of three digital signals that are generated by the FPGA of the CDU. This allows to adapt the signal conditioning for each sensor and compensates fiber damping which may arise due to fiber couplers.

The transimpedance amplifier is designed for high frequency input since incoming pulse rate equals the pulse repetition rate of the SL interrogator [15]. Figure 8.13 shows the PSpice® simulation results of the transimpedance amplifier for a parametric sweep [60] of the feedback capacity C_{fb}. Variation of C_{fb} allows to match the operational amplifier to the photo detector for high speed operation.

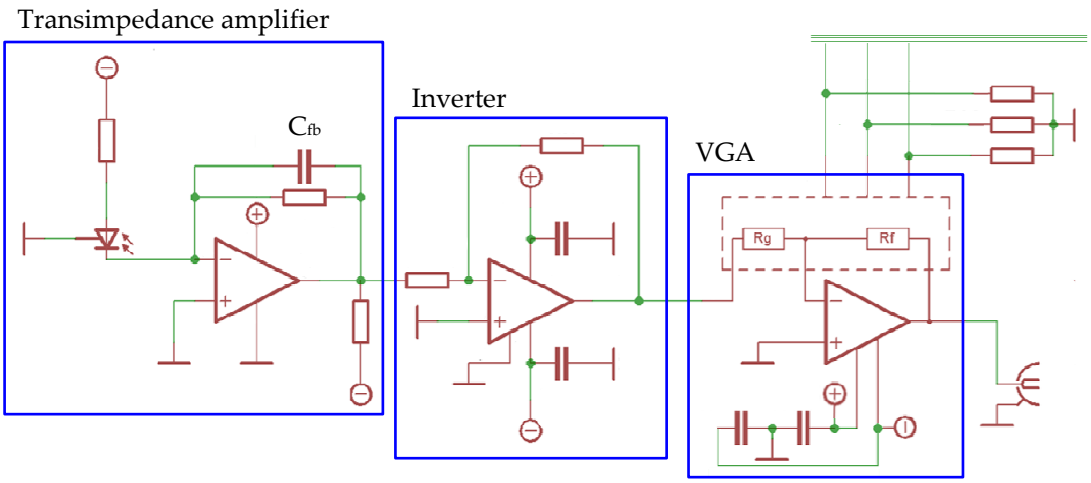

Fig. 8.12.: Circuit of the photo amplifiers. A transimpedance amplifier, an inverter and a variable gain amplifier in series convert the reflected intensities into analog voltages of appropriate magnitude for sampling with the ADC of the CDU.

A value of $C_{fb} = 0.4\,pF$ shows the best result and is chosen for implementation.

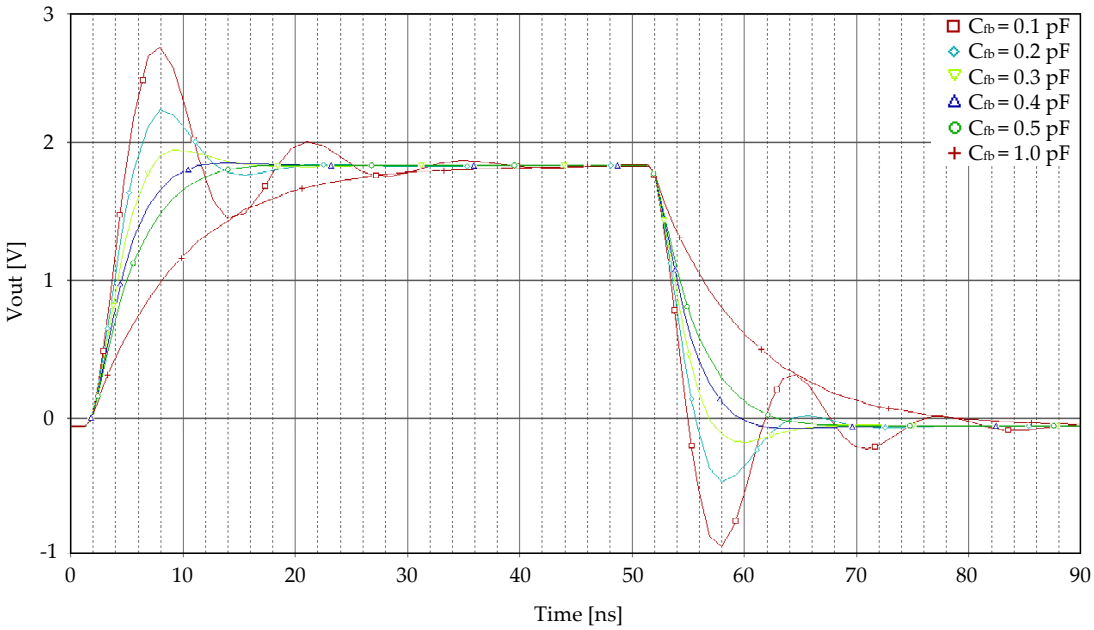

Fig. 8.13.: Simulation result of the transimpedance amplifier. A parametric sweep of the feedback capacity C_{fb} identifies the appropriate value.

In order to verify design and simulation of the transimpedance amplifiers, the frequency response has been measured. Therefore a signal generator was used to provide a frequency sweep as input to the transimpedance amplifier. Up to a frequency of 15 MHz, the transimpedance amplifier shows linearity and the gain stays at a constant value of 10. Figure 8.14 shows the measurement results.

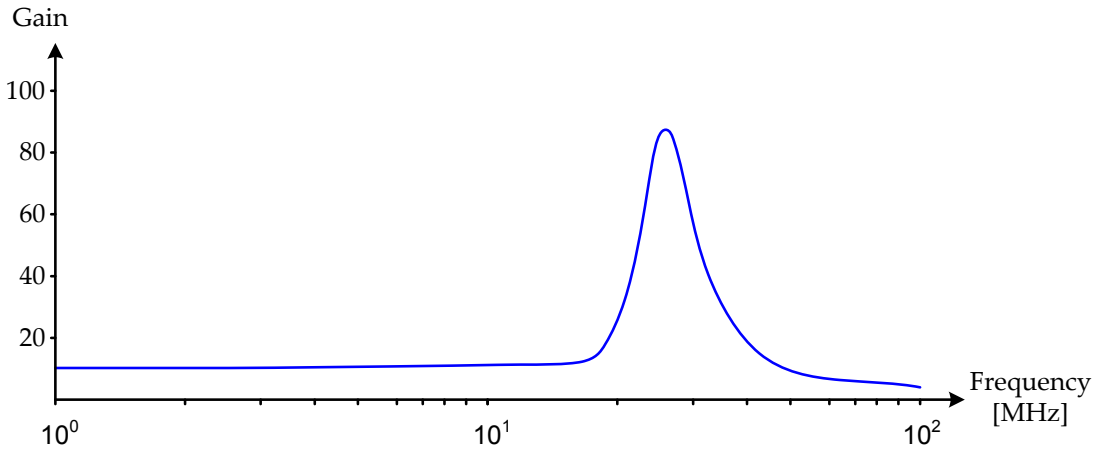

Fig. 8.14.: Large signal frequency response of the transimpedance amplifier. For frequencies up to 15 MHz the response is linear.

8.3.3. Optical Fiber Sensor Network

The fiber coupler unit (FCU) is a completely passive coupling structure shown in figure 8.15. At the current configuration, approximately 1.5 % of laser light that enters the FCU reaches the photo amplifier when the wavelength is adjusted to the center of a FBG. A maximum reflectance of 20 % of the FBG is assumed, which is the case for drawtower gratings that are used. The MG-Y laser diode delivers an optical output power af 20 mW which therefore results in a maximum of 0.3 mW of light that is reflected by an FBG at maximum.

The sensor network consists of optical fibers with inscribed FBG sensors. The SL interrogator provides fiber optic connections for up to three measurement channels (see Figure 8.15). Due to the sampling principle of the SL, there are no requirements for the sensors in terms of spectral width or position. The

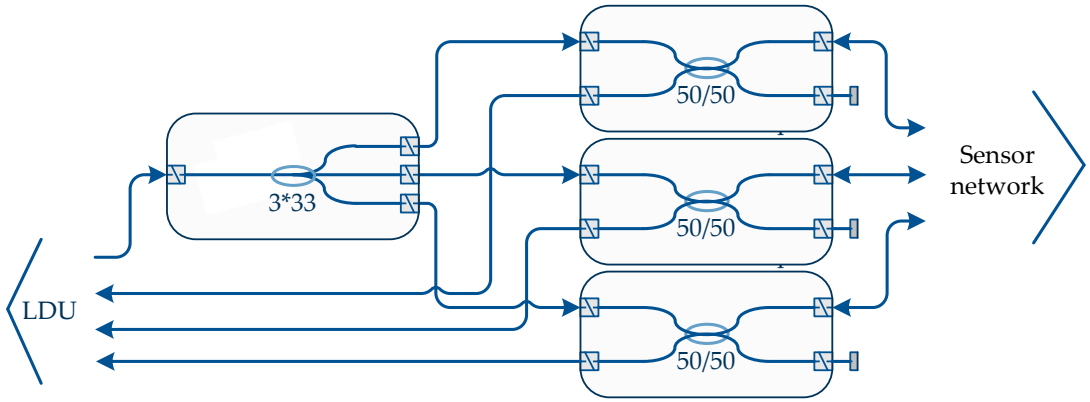

Fig. 8.15.: Fiber coupler unit (FCU). Light coming from the MG-Y laser diode is distributed to three measurement channels by a 1x3 fiber coupler. The reflected signals are guided to the photo-amplifiers of the LDU by three 2x2 couplers.

photo-amplifiers are designed to measure intensities in the range of 10 µW to 0.3 mW.

Since sensors have different distances to the interrogator, wavelength dependent time-of-flights (ToF) occur for pulses that are emitted by the SL and reflected by different FBG sensors. A new Time-of-Flight (ToF) algorithm is implemented that copes with this issue (see chapter 8.5.3).

8.4. Scanning Laser Characterization

As explained in chapter 5.4, the wavelength of the MG-Y laser diode is changed electrical by a set of three control currents that are provided at three inputs: Right reflector, left reflector and common phase current. Changing one of these control currents results in a change of the output wavelength. Since a deterministic relation between control currents and output wavelength is not provided by the operation principle of the MG-Y laser, a characterization cycle has to be performed wherein the three currents are varied systematically and the resulting output wavelength of each applied current triplet is measured and stored.

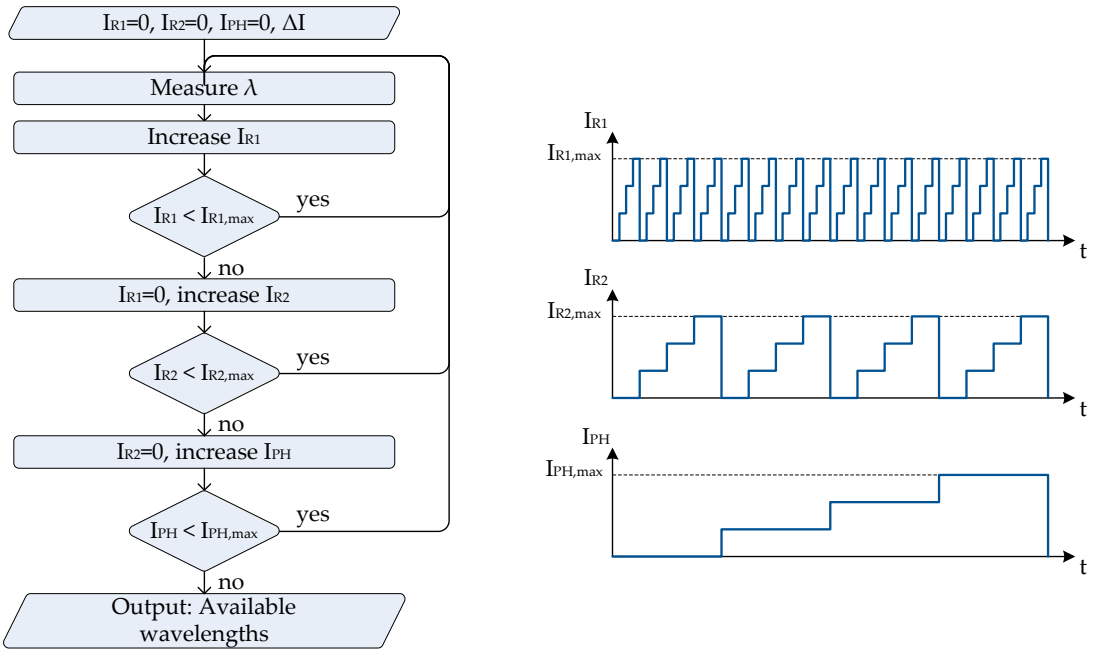

Fig. 8.16.: Flow chart of characterization cycle. The three control currents are increased step-wise by the user defined value ΔI until the maximum input current is reached. Every resulting output wavelength is measured and stored together with the according current values.

Figure 8.16 illustrates the laser characterization. The maximum currents for the control currents are, according to the data sheet of the MG-Y laser:. $I_{R1} = 20\,mA$, $I_{R2} = 20\,mA$ and $I_{PH} = 7\,mA$. The step-size ΔI is set to $0.2\,mA$ for the reflector currents and $2\,mA$ for the phase current. This results in 40000 steps for one characterization cycle, 10000 per phase current.

After characterization, the measurement results are evaluated and wavelengths that do not fulfill the requirements of a side mode suppression ratio higher than 30 dB and an absolute optical output power above 10.5 dBm are rejected. Approximately 85% of the current triplets result in wavelengths that fulfill the requirements. Three characterization cycles under constant conditions are performed in order to ensure reproducibility of the measurement results. Only current triplets that show a wavelength reproducibility within a range of 5 pm are kept in the wavelength table. Figure 8.17 shows the results of three characterization cycles with constant phase current $I_{PH} = 2.1\,mA$. For visualization purpose, offsets of ± 1 nm are added to two graphs to avoid

overlapping.

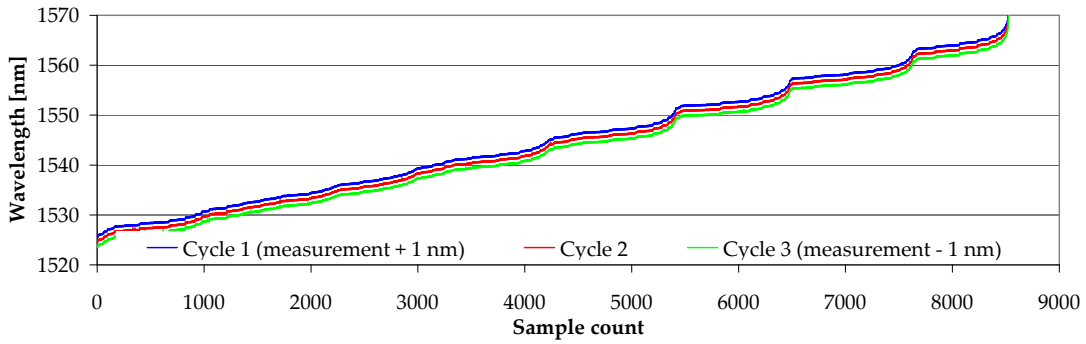

Fig. 8.17.: Three characterization cycles performed under equal conditions with a phase current of 2.1 mA result in approximately 8500 reproducible wavelengths distributed over a 45 nm wide spectrum.

Variation of the phase current I_{PH} results in a shift of the overall output spectrum. Thereby spectral gaps that result from missing overlap between resonator eigen-modes of both reflectors can be filled. Figure 8.18 shows wavelengths stemming from the entire characterization cycle with four different phase currents. Rising phase currents shift the spectrum to lower wavelengths due to the carrier injection into the common phase area of the MG-Y laser diode (see section 5.4).

The output spectrum of the MG-Y laser shows periodicity in terms of the reflector and phase current variations shown in figure 8.18.

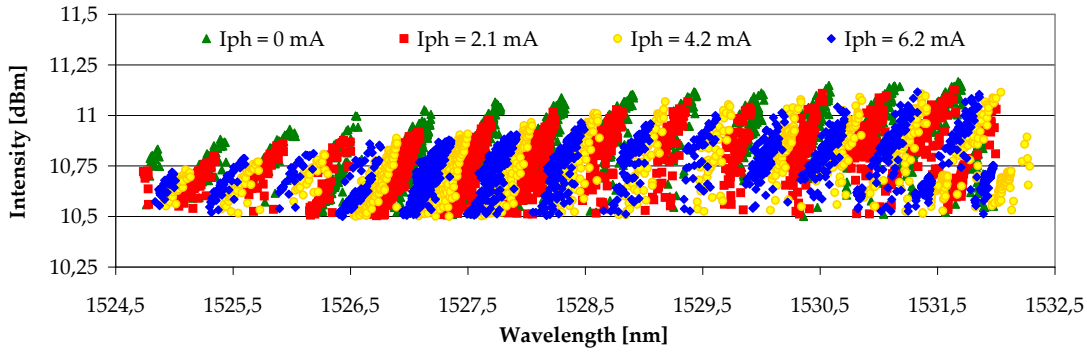

Fig. 8.18.: Variation of the phase current results in a shift of the spectrum towards lower wavelengths. Thereby spectral gaps can be filled.

Approximately every 6 nm, which equals a frequency of the FSR of the laser diode's resonator (see chapter 5.4), a wavelength jump is observed (see figure 8.19). At the points where the jumps occur, the corresponding reflector grating has been varied by carrier insertion, such that two neighboring laser modes overlap. This behavior is due to the vernier effect [175] and prohibits continuous wavelength tuning.

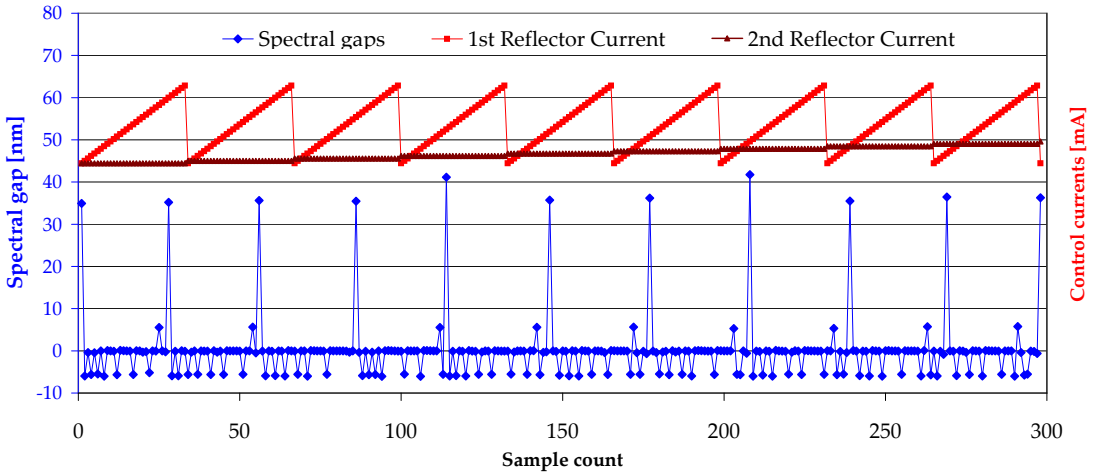

Fig. 8.19.: The output wavelength of the MG-Y laser is tuned. As long as identical modes of both resonators overlap, the output wavelength alters in unchanged spectral direction. At points where different modes are brought to overlap, the output wavelength jumps be integer multiples of the FSR (approximately 6 nm).

The laser temperature during laser characterization is shown in figure 8.20 together with the measured reflector currents. The temperature control loop achieves a constant laser temperature of approximately $29.78 \pm 0.020°C$ in order to ensure constant output wavelength.

A laser characterization cycle using a step width of 0.2 mA for both reflector currents I_{R1}, I_{R2} and three different values for the phase current I_{PH} (according to figure 8.18) yields more than 25000 control current triplets that generate corresponding wavelengths although several of these wavelengths are equal. Therefore another evaluation software scans through the wavelength table and eliminates all wavelengths that are double. Furthermore wavelengths of which the spectral distance is less than 7 pm are sorted out in order not to obtain

a sensor response with more than 32 sampling points. A higher number of sampling points per sensor is not supported by the firmware developed for the interrogator. The result is a wavelength table that contains 4655 different wavelengths λ_i within the available 42.3 nm wide spectrum of the MG-Y laser (see figure 8.21). Two consecutive wavelengths have a mean spectral distance of 9.1 pm within an overall spectrum from $1524.737\ nm < \lambda_i < 1567.068\ nm$.

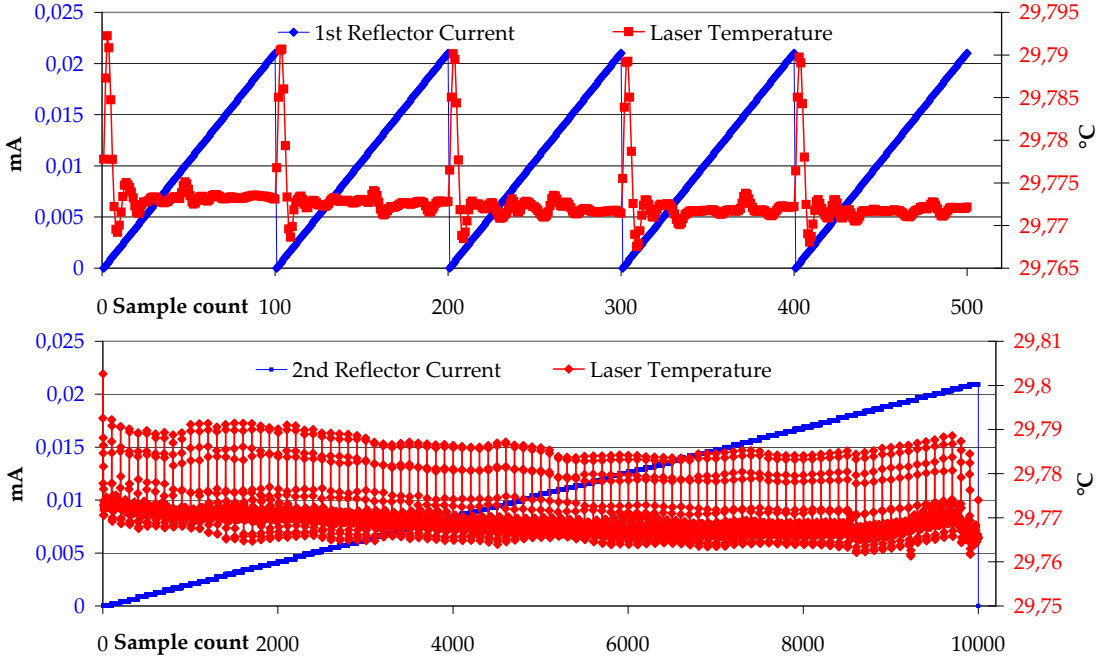

Fig. 8.20.: Variation of laser temperature during laser characterization. The laser TEC keeps the laser temperature constant within a 25 mK frame.

The final wavelength table is ordered by rising wavelengths and implemented in the memory of the CDU (see chapter 8.3.1) as look-up table (LUT) for wavelength generation and centroid calculation. Every line of the RAM therefore holds one wavelength which enables simple execution of the SL software because only pointers to memory cells have to be handled during operation. Figure 8.22 shows the principle configuration of the LUT.

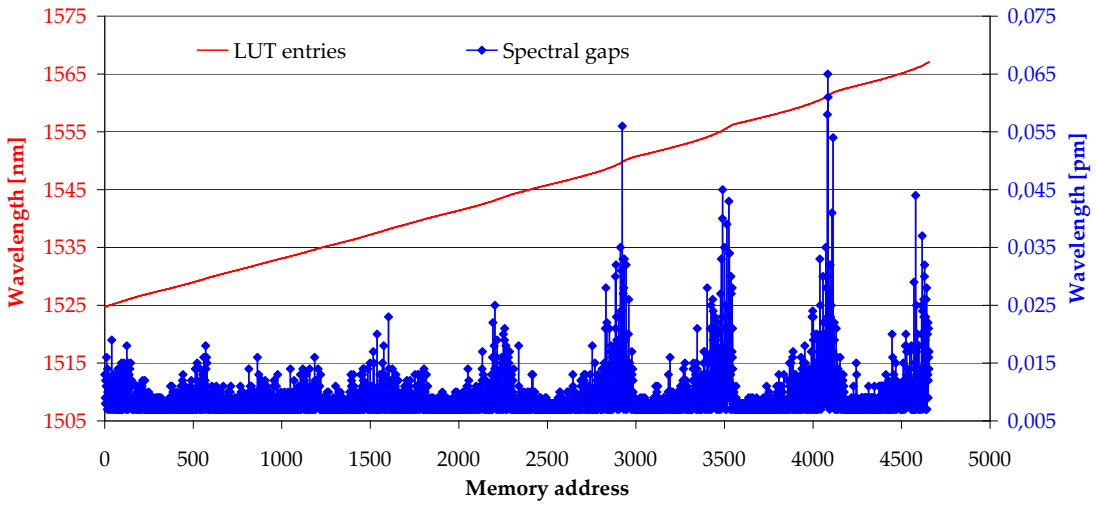

Fig. 8.21.: The look-up table (LUT) holds 4655 wavelengths in rising order. The mean spectral distance between two consecutive wavelengths is 9.1 pm.

n	λ	I_{R1}	I_{R2}	I_{Ph}
1	λ_1	$I_{R1,1}$	$I_{R2,1}$	$I_{Ph,1}$
2	λ_2	$I_{R1,2}$	$I_{R2,2}$	$I_{Ph,2}$
3	λ_3	$I_{R1,3}$	$I_{R2,3}$	$I_{Ph,3}$
		⋮		

Fig. 8.22.: The LUT is implemented in the CDU memory and is used for wavelength generation and centroid calculation.

8.5. Soft- and Firmware Architecture

The hardware architecture of the SL interrogator (see chapter 8.3) has been chosen to ensure high flexibility by software programming of the system. Adjusting the programs running at the Windows based embedded PC (called the host), at the DSP and at the FPGA allows to adapt the functionality of the system to the user requirements. The three programs that have been developed within this work implement the following functionality:

- **Host**: A graphical user interface of the SL based on Microsoft Visual C++® has been implemented. Thereby the user can load the LUT into the CDU memory, scan through the spectrum in order to identify sensors, select sensors for continuous measurement and execute measurements. The interface between the host and the SL hardware is standard PCI, allowing to control the SL hardware and to acquire measurement data that is displayed at the monitor and stored in files at the hard disc drive.

- **DSP**: The DSP connects the SL hardware to the PCI interface. Furthermore it commands the FPGA and thereby all analog hardware. Dependent on the operation mode selected by the user (see section 8.5.1) the DSP is prompted to adjust the hardware accordingly (e.g. to start the peak-tracking algorithm at the FPGA). Code Composer Studio® C++ development environment is used to create DSP programs.

- **FPGA**: Providing input to all DAC and acquiring all ADC data is handled by the FPGA. Since this device allows parallel execution, peak-tracking is done by the FPGA in real-time where at the same time the laser is controlled. Xilinx Webpack® is used for programming the FPGA in VHDL programming language.

An overview of the SL CDU architecture that requires software programming is shown in figure 8.23.

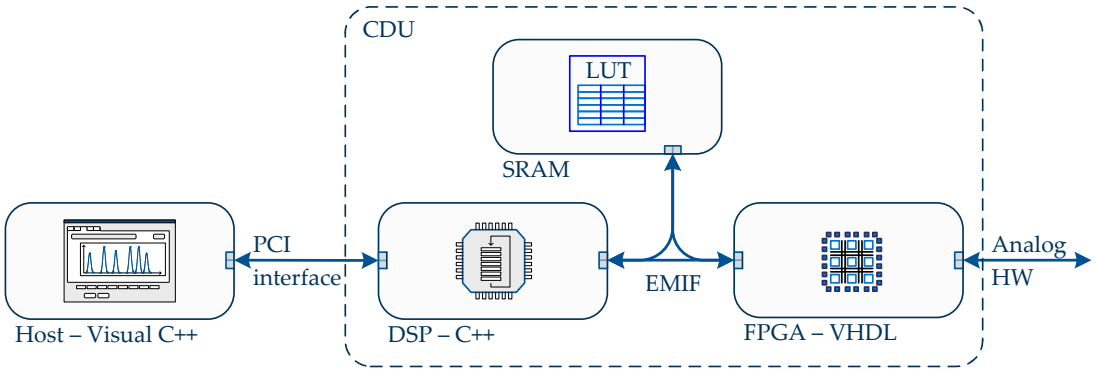

Fig. 8.23.: Overview of SL architecture that is configured by programming. Three different programs are implemented in the host (Windows based PC), the DSP and the FPGA.

The communication between DSP, FPGA and RAM is based on data transfer via the Texas Instruments® external memory interface (EMIF) bus which implements register mapping.

8.5.1. Scanning Laser Operation

Three different measurement modes (see figure 8.24) have been implemented in the SL interrogator:

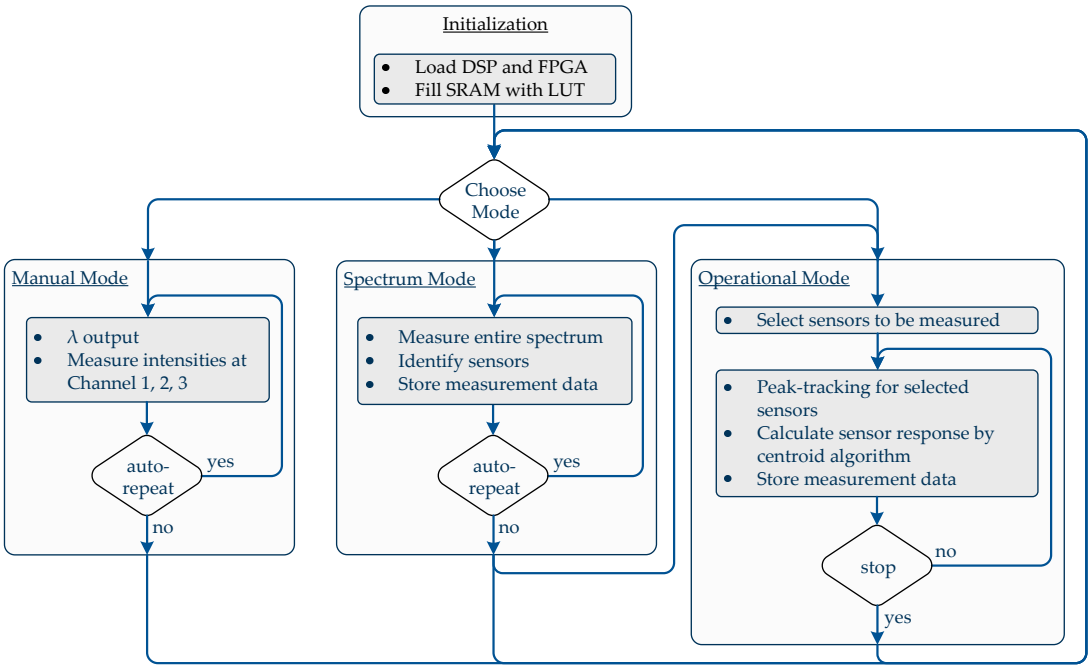

Fig. 8.24.: Three measurement modes are available. In manual mode one wavelength is selected and output, in spectrum mode the entire spectrum is scanned and in operational mode selected sensors are measured continuously by peak-tracking.

- Manual mode: One wavelength that is available in the loaded LUT is generated by the laser diode and sent to all three measurement channels. The reflected intensities are measured, displayed and recorded continuously. Auto-repeat is available wherein a rate for measurement repetition can be set.

- Spectrum mode: All wavelengths within the LUT are generated by the laser diode sequentially. For every wavelength, the reflected intensities are measured. After the spectrum has been scanned using all 4655 wavelengths, the recorded intensities are displayed and stored in a measurement file.
- Operational mode: Peak-tracking is used (see chapter 8.5.2) in order to scan the selected sensors and track them in the case of spectral shifts due to environmental loads. In order to use the operational mode, sensors have to be selected. Therefore the spectrum mode is executed once in order to scan through the entire spectrum. Existing sensors within each measurement channel are identified and displayed. The user selects the sensors that shall be measured, switches to the operational mode and starts the measurement.

8.5.2. Peak-Tracking Algorithm

Contrary to comparable systems, the SL interrogator is capable of switching to any available wavelength within its spectrum in less than a microseconds. Therefore standard continuous sweeping through the entire spectrum is not meaningful. A new measurement scheme, wherein spectral gaps between consecutive sensors are not scanned but skipped is implemented in the SL interrogator. Since most of the reflected spectrum consists of the gaps between the sensors, overall measurement time is thereby reduced significantly. One problem arises from this measurement scheme: Due to the fact that the sensor's spectral answers vary in time, a special algorithm for tracking the spectral movement has to be implemented.

A sensor fiber including a number of eight sensors with a bandwidth of $200\,pm$ each yields a "spectral loading" of $1.6\,nm$. Since the full spectrum of the laser diode comprises $42.3\,nm$ more than 96.2% of the entire spectrum is unused and can be skipped during the measurement. In order not to loose the spectral answers of the sensors, their variation has to be tracked so that the sampling wavelengths can exactly be attained. This is done by the peak tracking algorithm that is explained in this section. Only one single FBG is considered for the sake of simplicity.

As shown in figure 8.2, λ_{start} and λ_{end} are the two wavelengths beside the spectral answer of a FBG that have zero reflected intensity. Since there is always some noise floor level I_{nf}, zero intensity in this case means a reflected intensity has a value less than I_{nf}: $I_{refl}(\lambda_{start}) < I_{nf}$ correspondingly $I_{refl}(\lambda_{end}) < I_{nf}$. By scanning through the entire output spectrum of the laser diode as an initial step, these two wavelengths can be determined. After the measurement has started and the spectral answer of the FBG moves due to alteration of the measurand, the reflected intensities between $I_{refl}(\lambda_{start})$ and $I_{refl}(\lambda_{end})$ are evaluated for determination of the mean wavelength. The movement of the spectral answer peak is tracked by additionally observing the two wavelengths $I_{refl}(\lambda_{start})$ and $I_{refl}(\lambda_{end})$.

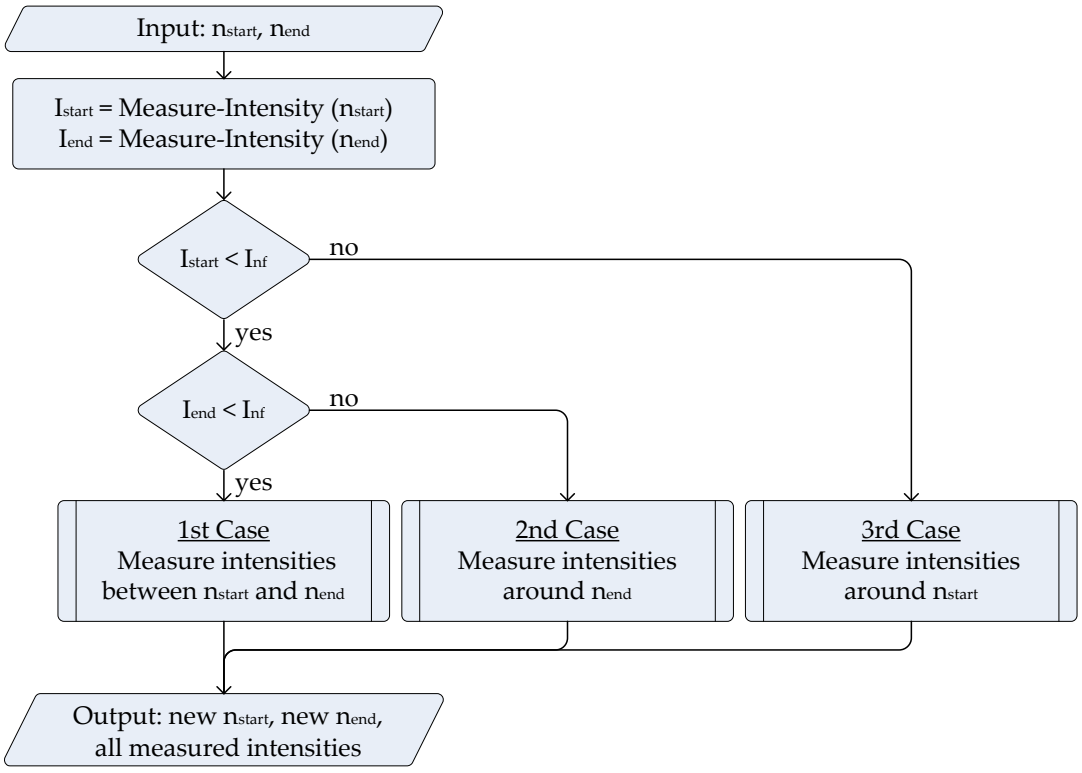

Fig. 8.25.: This program flow diagram shows the different cases in the peak tracking algorithm. Depending on the measured intensity values of $I_{refl}(\lambda_{start})$ and $I_{refl}(\lambda_{end})$, the sensor answer is tracked towards higher or lower wavelengths.

Measurement Case Selection

1st Case: No movement If the measurand change is very slow or even zero, the spectral peak does not move as far as the distance between two sampling points which is approximately 9 pm in average (see section 8.4). This case is indicated by the condition:

$$I_{refl}(\lambda_{start}) < I_{nf} \wedge I_{refl}(\lambda_{end}) < I_{nf} \tag{8.7}$$

In this case no further peak tracking procedure is necessary and all wavelengths between λ_{start} and λ_{end} are sampled in order to recalculate the mean wavelength.

The condition of 8.7 could also be true when the spectral response of the sensor, due to a high gradient of the measurand change, shifts so fast that it moves completely out of the spectral region which is spanned by λ_{start} and λ_{end}. At the end of this section the possibilities for this error are discussed.

2nd Case: Movement to higher wavelengths If the measurand changes in a way that the spectral peak shifts to higher wavelengths, the condition for the second case is:

$$I_{refl}(\lambda_{start}) < I_{nf} \wedge I_{refl}(\lambda_{end}) > I_{nf} \tag{8.8}$$

Because $I_{refl}(\lambda_{start})$ does no longer belong to the spectral answer of the sensor, this case can only be handled by sampling around λ_{end}. Firstly, sampling starts towards higher wavelengths until a wavelength with an intensity less than I_{nf} is detected. This wavelength becomes the new end wavelength $\lambda_{end,new}$ when the peak tracking procedure is started for this sensor the next time. After $\lambda_{end,new}$ has been found, sampling starts again from λ_{start}, but this time towards lower wavelengths. The first wavelength which has a reflected intensity of less than I_{nf} becomes the new start wavelength $\lambda_{start,new}$.

3rd Case: Movement to lower wavelengths If the measurand changes in a way that the spectral peak shifts to lower wavelengths, the condition for the third case is:

$$I_{refl}(\lambda_{start}) > I_{nf} \wedge I_{refl}(\lambda_{end}) < I_{nf} \tag{8.9}$$

Because $I_{refl}(\lambda_{end})$ does no longer belong to the spectral answer of the sensor in this case, it has to be sampled around λ_{start}. The rest of the procedure is performed according to the second case.

4th Case: Broadening of peak The fourth case theoretically is not possible. However, due measurement noise the following condition might occur:

$$I_{refl}(\lambda_{start}) > I_{nf} \wedge I_{refl}(\lambda_{end}) > I_{nf} \tag{8.10}$$

This would indicate a peak that is spectrally broader than the last time it was measured. Handling this case is just the same procedure as in second or third case and therefore not shown in figure 8.25.

Peak tracking measurement

In order to verify the peak tracking algorithm a beam in bending is used. A FBG sensor is glued onto the beam and the start wavelength λ_s was logged during manual bending. A maximum strain of approximately 800 $\mu\epsilon$ is applied to the FBG when the beam is fully bended. Figure 8.26 shows the logged start wavelengths λ_s, the measurement rate during the test was 110 Hz.

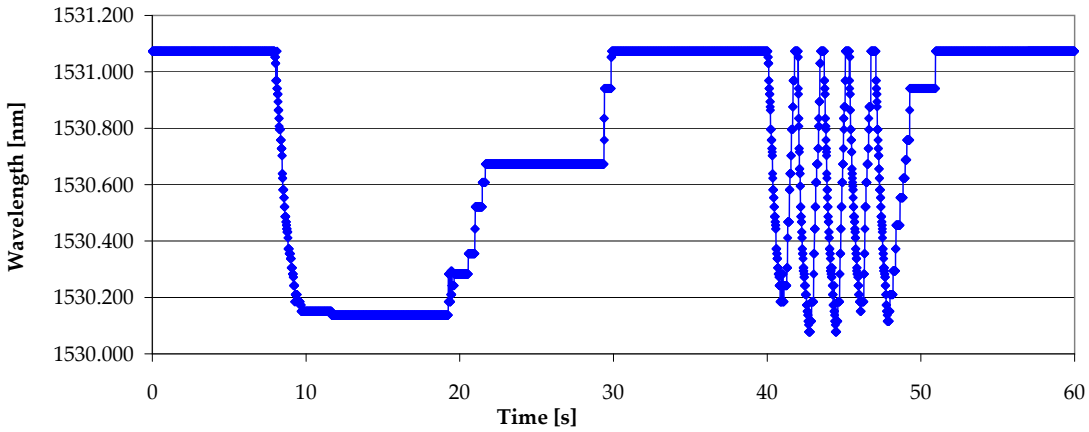

Fig. 8.26.: The logged start wavelength λ_s during measurement with a test setup based on a FBG mounted on a beam in bending.

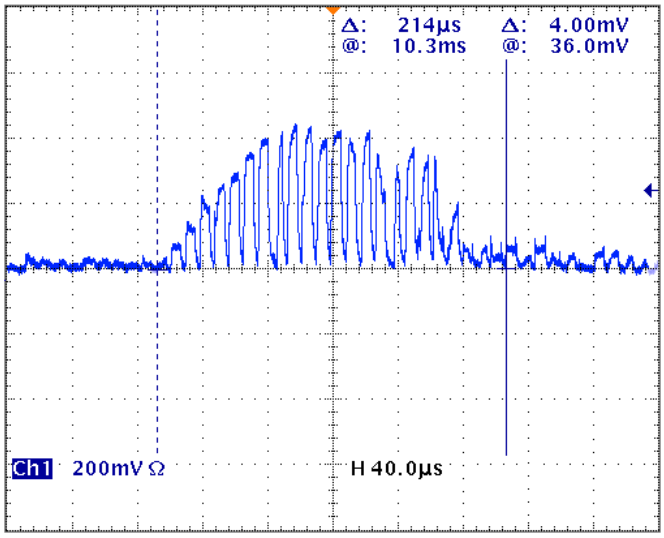

Fig. 8.27.: The sensor is sampled by approx. 20 sampling points. Therefore a sensor sample rate of more than 4.5 kHz is achieved by peak tracking.

Figure 8.27 shows an oscilloscope measurement of the sensor sampled by 19 points when the noise level is set to 100 mV. Therefore a time of 214 μs is required which results in a maximum sensor sample rate of $f_{SR} = 4.67\ kHz$.

Limitations of the peak tracking procedure

Time that passes between two consecutive measurements of one FBG sensor depends on the overall sensor sample rate f_{SR}. Thereby the time delay T_d between consecutive measurements of the same sensor is $T_d = 1/f_{SR}$. The measurement rate f_{SR} depends on the number of senors N_S that are measured sequentially, on the number of wavelength sampling points per sensor n_{spps} and on the pulse repetition rate f_{prr} of the MG-Y laser diode:

$$f_{SR} = \frac{f_{prr}}{N_S \cdot n_{spps}}. \tag{8.11}$$

Considering a mean number of ten wavelength sample points per sensor $n_{spps} = 10$ and a pulse repetition rate of $f_{prr} = 10\ kHz$, the two extreme cases for N_S correspond to either one single sensor or the maximum number of 24 sensors. This results in a range for the time delay T_d of

$$1\,ms\ <\ T_d\ <\ 24\,ms. \tag{8.12}$$

Depending on the time delay T_d between two consecutive measurements of one sensor, a maximum change Δ_{max} of the measurand can be detected. If the measurand change is faster than Δ_{max}/T_d, correct function of the interrogation system is not assured, since the sensor answer peak may be lost. Assuming a FBG sensor with a spectral bandwidth of $200\,pm$, our interrogation setup will work properly if the measurand change satisfies the condition $\Delta_{max} < 8.3\frac{pm}{ms}$ for a fully loaded system ($N_S = 24$) and $\Delta_{max} < 200\frac{pm}{ms}$ for a system holding only one sensor. These values correspond to measurand changes of approximately $0.8\frac{^\circ C}{ms} < \Delta_{max,^\circ C} < 19.3\frac{^\circ C}{ms}$ for a temperature sensor. This gradient that can be measured by the SL is higher than required for practical temperature sensing. This allows to use the SL interrogator for sequential read-out of hundreds of sensors. Sensing of e.g. 200 sensors sequentially would yield a measurement rate of $f_{SR} = 5/s$ for each sensor at a sample rate of $f_{prr} = 10\,kHz$.

8.5.3. Time-of-Flight Algorithm

In the time domain picture all ten sampling wavelengths are sequentially generated by the laser diode (see also figure 8.2). Pulses are sent out by the SL interrogator, guided to the corresponding FBG sensor and reflected back to the SL for intensity measurement. "Time of Flight" (ToF) is defined as the travel time of a sensing light pulse. Since the distance between the interrogator and the sensor is different for each sensor also the ToF values for each sensor are different from each other. In order to ensure that sampling of the measured intensity of the corresponding wavelength pulse is performed at the correct time, the ToF for each sensor has to be evaluated prior to the operation of the system and implemented in the LUT as separate column. According to figure 8.28, the ToF value of sensor number *i* in channel number *j* is defined as

$$ToF_{ji} = \frac{2d_{ji} \cdot n_F}{c} \tag{8.13}$$

wherein d_{ji}, n_F and c stand for the distance between sensor and interrogator, the refractive index of the optical fiber and the speed of light respectively.

At the current configuration of the SL interrogator, three measurement channels accommodate up to eight FBG sensors at different positions. Therefore up to

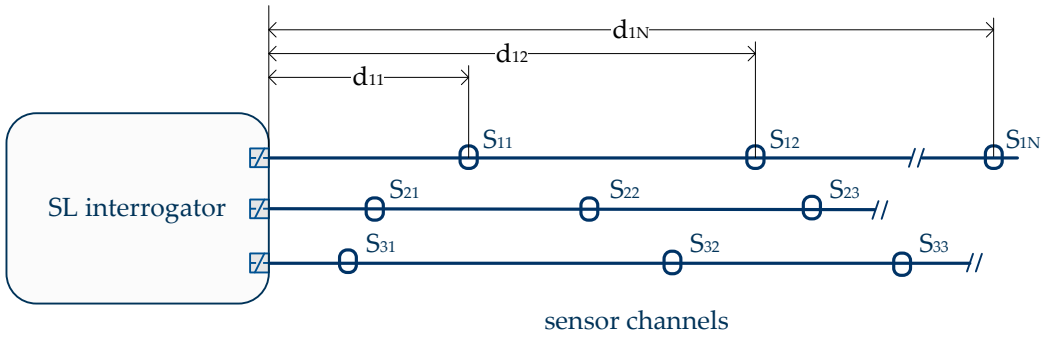

Fig. 8.28.: The Time-of-Flight (ToF) of a pulse depends on the position of the sensor that reflects the pulse.

24 ToF values are possible. Since the SL can be configured to switch between any two wavelengths of the available spectrum, the sensor sampling order can be defined by the user. Because of the different ToF values due to the varying sensor distances (see figure 8.28), overlapping of two reflected pulses can occur. In order to avoid this error, the ToF-algorithm has been developed. Since further development of the SL interrogator is foreseen where the system may have more than three channels, the ToF-algorithm has been developed in general without restriction to the current numbers of channels and sensors.

A maximum number of J measurement channels, each holding a channel dependent maximum number of I_J sensors is assumed. The ToF value of each sensor therefore is characterized by two indexes *j* and *i*. An allowed spectral range has to be defined for each sensor in which the sensor response may vary. Figure 8.29 shows an example of measurement channels with allocated sensor ranges.

The advantage of the MG-Y laser to switch between sensors independently from the spectrum has the drawback that the CDU is in charge of the timing. A sensing pulse sent to sensor S_{ji} yields a reflected intensity that can be measured at the corresponding photo detector after a delay time of ToF_{ji}. Therefore the ToF values of all sensors have to be known either by calculation according to formula 8.13 or by measurement. Furthermore the spectrum has to be allocated to the sensors of each channel. It is required that every sensor stays within its pre-defined spectral range to ensure that sensors are not able to overlap spectrally. Depending on the number of sensors I_J, that are implemented

within one sensor fiber, the overall spectrum is separated according to figure 8.29. The spectral regions may have different widths and are different for each channel. The spectral range for each sensor is dependent on the measurand (strain, temperature) and on the expected measurement range.

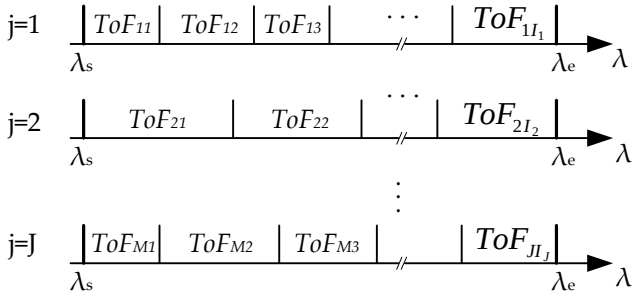

Fig. 8.29.: J fibers are connected to the SL interrogator each holding a different number I_J of sensors. For each measurement channel, the output spectrum of the laser can be allocated to the sensors differently.

The overall measurement rate of the SL interrogation system is limited by the sampling rate f_{ADC} of the ADC devices. Due to this quantization, the SL interrogator can only handle ToF values as multiples of $T_{ADC} = 1/f_{ADC}$. The interrogator emits a pulse and waits a predetermined number of clock cycles of f_{ADC} before it measures the according photo detector input. In order to meet the sampling theorem, the output duty cycle T_P of the laser must be longer than T_{ADC}. Since the sampling rate f_{DAC} of the DAC devices at the current system configuration is two times f_{ADC} the duty cycle is set to a constant value of $T_P \geq= 1.5 \cdot T_{ADC}$. Figure 8.30 illustrates sampling with varying ToF values using the SL interrogator.

Assuming that a single sensor has to be evaluated by a centroid algorithm based on 10 sample points, ten measurements are required. This takes a time of $T_s = 10 \cdot 2 \cdot T_{ADC} = 0.8\ \mu s$ for a single sensor measurement, for $T_0 = 2 \cdot T_{ADC}$. The interrogation system, if operated with one single sensor only, has therefore a maximum measurement frequency of 1.25 MHz. This calculation takes not into account low pass behavior of the LDU which reduces the maximum available sample rate of the SL interrogator.

If a sensor channel holds I_J sensors, it has to be dealt with I_J different ToF

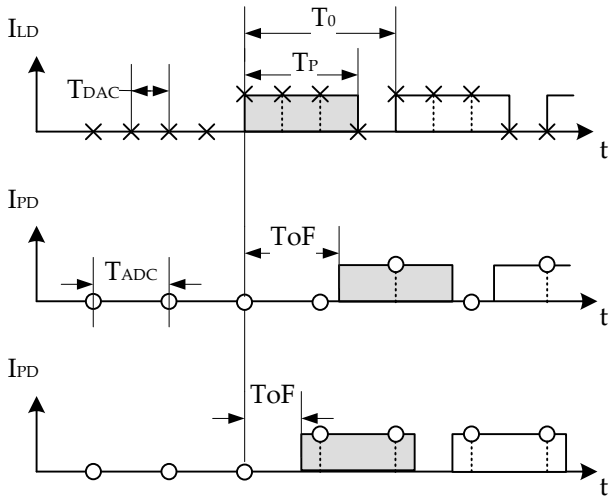

Fig. 8.30.: In order to meet the sampling theorem, each pulse has a length of $T_P = 1.5 \cdot T_{ADC}$.

values. By wavelength switching within the entire spectrum of the laser, $I_J!$ (factorial operation) different sequences and $I_J \times (I_J - 1)$ different transitions from one ToF region to another one are possible. Thereby overlap of incoming pulses at the photo detector of the corresponding channel is possible as shown in figure 8.31. This happens e.g. if two sensors inside the same channel are read out in an inappropriate order. As long as all sensors are read out in the order of rising ToF values, overlapping of pulses does not occur. If two sensors i and $i + 1$ have to be read out in reverse order and overlap, a delay time of Δt

$$\Delta t = (ToF_{ji} + T_P) - \Big(ToF_{j(i+1)} + T_0\Big) \tag{8.14}$$

needs to be inserted.

Considering a number of J sensor channels complicates the overlapping problem. Since every fiber contains I_J different sensors, two or more sensors of different channels can overlap spectrally (see figure 8.32). In order to avoid any overlap at the detectors, each channel has to be read out in the order of rising ToF values. Parallel read out of the two channels shown in figure 8.32 would therefore result in a measurement sequence of $S_{21} \rightarrow S_{11} \rightarrow S_{12} \rightarrow S_{22} \rightarrow S_{23}$. On the right hand side of figure 8.32 the spectral positions of the sensors are shown. Sensor S_{12} spectrally overlaps with sensor S_{23} although the order of

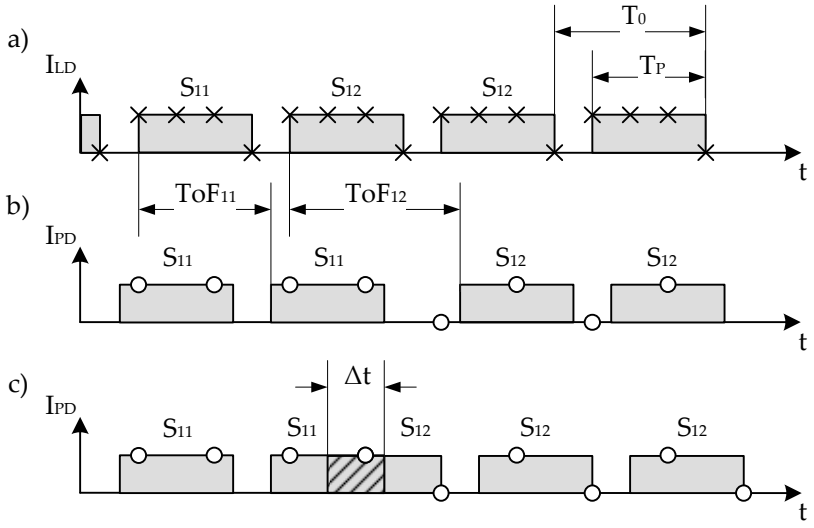

Fig. 8.31.: a) Sensors S_{11} and S_{12} of one measurement channel are sampled consecutively. b) $ToF_{11} < ToF_{12}$ results in a delay at the photo detector. c) $ToF_{11} > ToF_{12}$ may result in an overlap at the photo detector. Inserting a measurement delay of Δ_t avoids overlapping.

rising wavelengths is met. Interrogating all sensors in the above mentioned order could in this example result in an overlap of sensor pulses S_{22} and S_{23} at the photo detector of channel two.

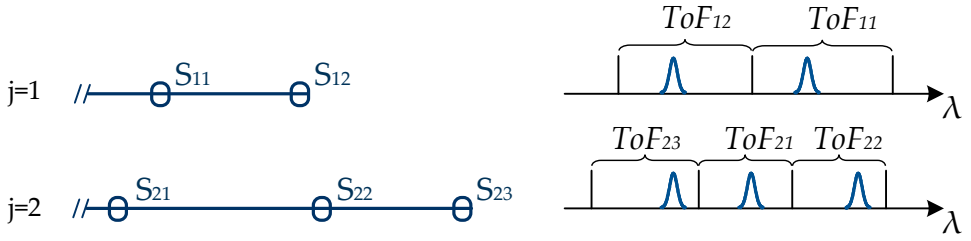

Fig. 8.32.: Two measurement channels are shown. Read-out according to rising ToF values fails because S_{12} and S_{23} overlap spectrally.

One possible solutions to this problem is to design the measurement system in a way that sensors of different channels are not able to overlap. This, however, would restrict the high versatility of the interrogation system. Moreover the adaptability to existing applications, wherein sensor fibers are for example embedded in composite material, would become lost. A solution that can be

implemented by software engineering is the calculation of a delay time Δ_t according to formula 8.14 and its insertion between the consecutive pulses that read out S_{23} and S_{22} in order to avoid overlapping.

8.6. Test Results and Evaluation

Within this section, calibration and test results of the SL interrogator are summarized. Figure 8.33 compares results obtained by the SL interrogator with oscilloscope monitoring of the LDU transimpedance photo amplifier output.

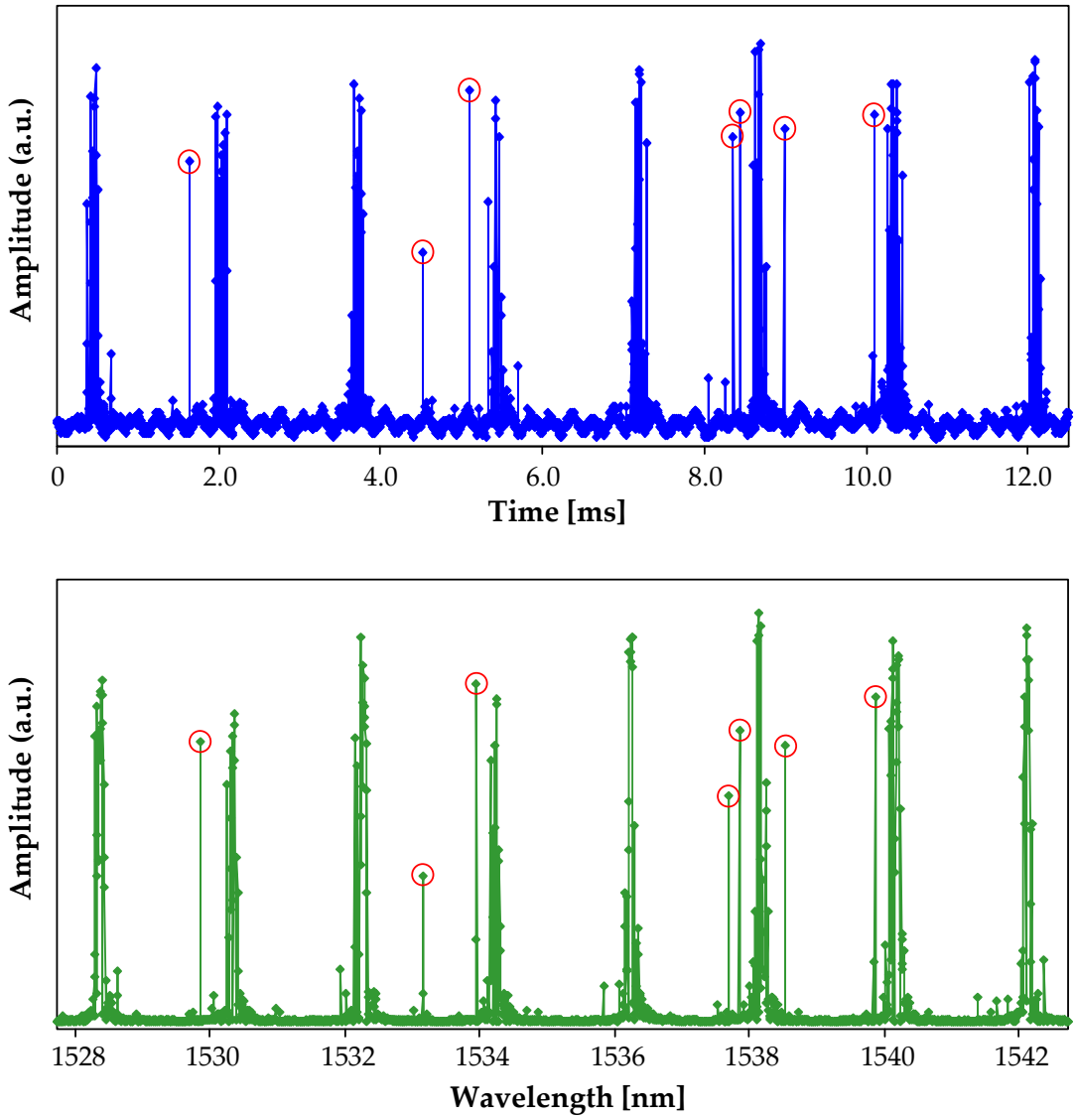

Fig. 8.33.: SL measurement in spectrum mode. The upper diagram was generated by monitoring the SL photo-amplifier output with an oscilloscope. The lower diagram shows the corresponding measurement file that is recorded by the SL. Red circles indicate incorrect measurement values due to mismatches in the LUT.

Some measurement points deviate from the expected value. This is due to the fact that some control current triplets do not yield the expected output wavelength. Red circles in figure 8.33 indicate, where a wavelength was emitted by the SL that should result in reflected zero but results in non-zero intensity. During laser characterization the laser temperature was kept constant (see figure 8.20), because wavelength where only switched every couple of seconds. During the spectrum mode, new control currents are applied to the laser every $100\ \mu s$. Therefore the temperature inside the laser diode varies since the TEC is not able to control the temperature so fast. Thereby instable wavelengths can occur randomly. The developed sensor evaluation algorithms however, can cope with this issue and filter wrong measurement points.

The influence of the number of sample points per sensor on the measurement accuracy has been investigated by measurement of a FBG sensor mounted on a beam in bending. Figure 8.34 shows the calculated standard deviation for different numbers of sampling points of one sensor. The measurement accuracy was estimated by evaluation of fifty sensor measurements for each number of sampling points at constant strain value.

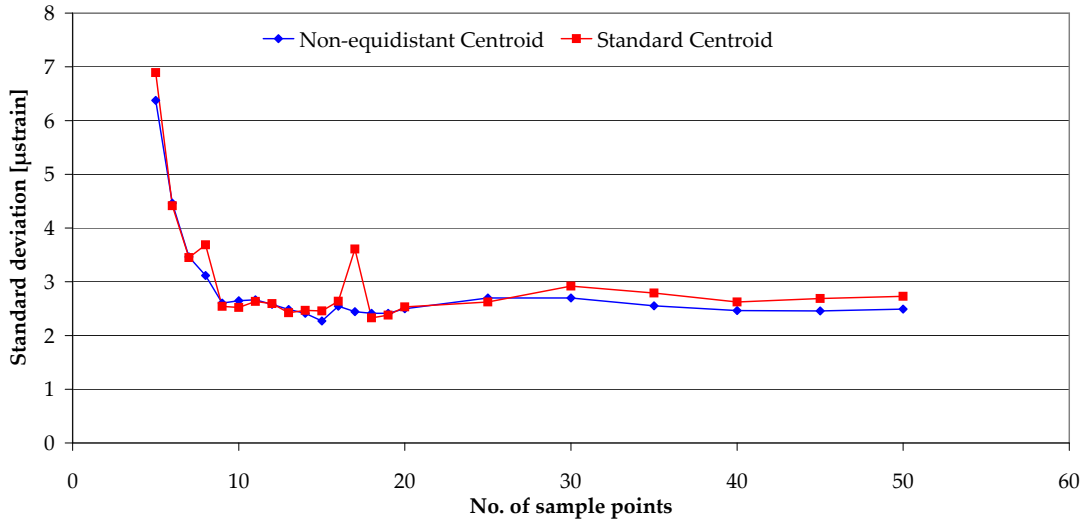

Fig. 8.34.: Down to a number of ten sampling points per sensor, the standard deviation of the measurement of a strain sensor on a beam in bending stays below $3\ \mu\epsilon$. The specially developed centroid algorithm for non-equidistant sampling copes with varying spectral sampling distances in contrast to the standard centroid algorithm.

For a number of approximately fifty down to ten sampling points per sensor, the standard deviation stays constant at a value less than $3\ \mu\epsilon$. Reducing the number of sampling points below ten results in increased standard deviation.

Figure 8.34 compares the specially developed centroid algorithm (SCA) for non-equidistant sampling (see also section 8.2) with the standard centroid algorithm. The standard algorithm shows deviations since the SL interrogator does not supply spectrally equal distributed wavelengths.

Figure 8.35 shows the calibration results of three FBG sensors in one measurement channel at the design wavelengths 1528 nm, 1530 nm and 1532 nm. The sensitivities of the three sensors are linear interpolated to 12.84 pm/K, 13.29 pm/K and 13.60 pm/K.

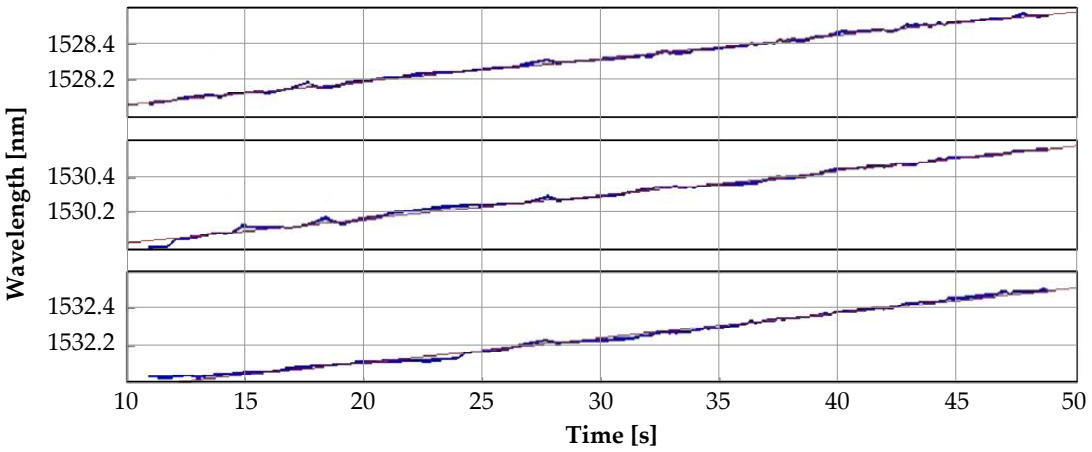

Fig. 8.35.: Three FBG sensor calibrations in a waterbath. The water temperature was measured with an electrical reference at an accuracy of 0.1 K. Sensitivities of the sensors vary between 12.8 and 13.6 pm/K.

After sensor calibration, one sensor was thermally cycled in the waterbath. The measurement result shown in figure 8.36 are confirmed by an electric reference sensor. Deviations of the optical temperature sensing from the electric reference measurement at approximately 1528.6 nm are due to instabilities of the laser output wavelengths at this spectral position.

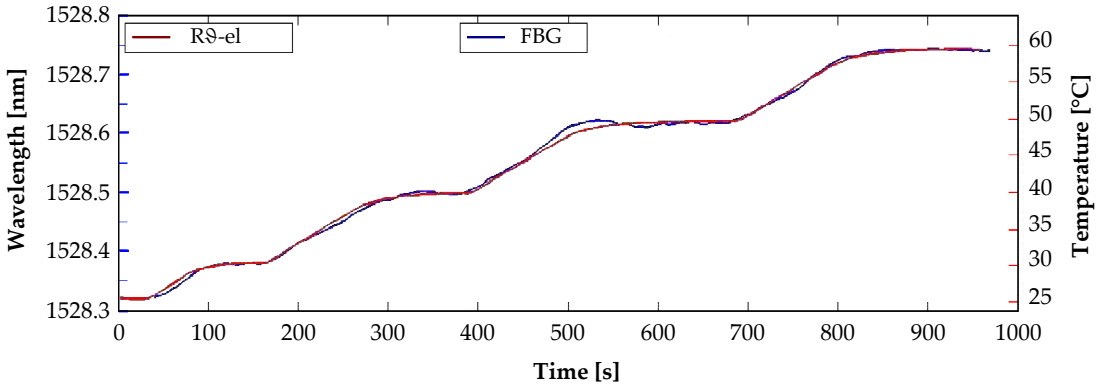

Fig. 8.36.: An FBG configured as temperature sensor after calibration. An electrical reference sensor confirms the measurement results.

Two FBG sensors for high-temperature measurement, for measurement applications at e.g. jet engines, have been mounted an a structural demonstrator and thermally cycled inside a high-temperature oven. Temperatures higher than $700°C$ have been applied to the sensors. Figure 8.37 shows the measurement results.

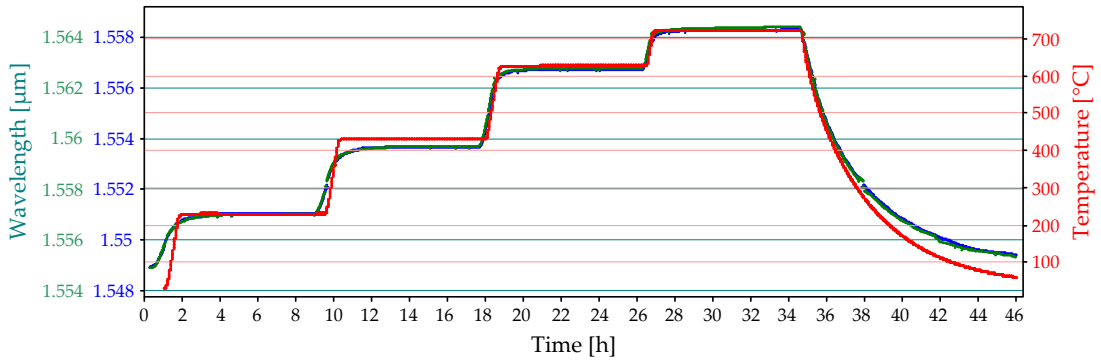

Fig. 8.37.: Temperature measurement results of two FBG sensors inside a high temperature oven before calibration.

At the four temperature plateaus, four wavelength values of each sensor have been measured according to table 8.2. Since FBG1 and FBG2 have different design wavelengths, the offset between both sensors have been additionally calculated and the mean value of the offset is determined to 6022 pm.

Tab. 8.2.: Temperature measurement at four plateaus of figure 8.37.

Temperature [°C]	**Wavelength FBG1 [pm]**	**Wavelength FBG2 [pm]**	**Δλ = FBG2-FBG1 [pm]**
228	1551048	1557023	5975
429	1553683	1559686	6003
624	1556755	1562791	6036
720	1558312	1564389	6077

Using the measurement points of table 8.2 as reference points for mutual FBG sensor calibration, the calibration functions of temperatures T_1 and T_2 in dependence of λ_1 and λ_2 for FBG1 and FBG2 have been quadratically interpolated to

$$T_1(\lambda_1) = -1.68 \cdot 10^{-6} \left(\frac{^\circ C}{pm}\right)^2 \cdot {\lambda_1}^2 + 5.30 \frac{^\circ C}{pm} \cdot \lambda_1 - 4.17 \cdot 10^6\, ^\circ C \quad (8.15)$$

respectively

$$T_2(\lambda_2) = -1.70 \cdot 10^{-6} \left(\frac{^\circ C}{pm}\right)^2 \cdot {\lambda_2}^2 + 5.38 \frac{^\circ C}{pm} \cdot \lambda_2 - 4.25 \cdot 10^6\, ^\circ C. \quad (8.16)$$

Due to the mean offset of $\Delta\lambda \approx 6022pm$ between both sensors, λ_x in the equations is substituted by $\lambda_x + \Delta\lambda$:

$$\begin{aligned} &T_2(\lambda_2) \approx T_2(\lambda_1 + \Delta\lambda) \\ &T_2(\lambda_2) = -1.70 \cdot 10^{-6} \left(\tfrac{^\circ C}{pm}\right)^2 \cdot (\lambda_1 + \Delta\lambda)^2 + 5.38 \tfrac{^\circ C}{pm} \cdot (\lambda_1 + \Delta\lambda) - 4.25 \cdot 10^6\, ^\circ C \end{aligned}$$

$$\begin{aligned} &T_1(\lambda_1) \approx T_1(\lambda_2 - \Delta\lambda) \\ &T_1(\lambda_1) = -1.68 \cdot 10^{-6} \left(\tfrac{^\circ C}{pm}\right)^2 \cdot (\lambda_2 - \Delta\lambda)^2 + 5.30 \tfrac{^\circ C}{pm} \cdot (\lambda_2 - \Delta\lambda) - 4.17 \cdot 10^6\, ^\circ C \end{aligned} \quad (8.17)$$

These functions have been used to determine the calibrated measurement results which are shown in figure 8.38. It can be seen, that the reference temperature sensor was mounted outside the structural demonstrator, since its response to temperature variations is always faster than the FBG sensor responses.

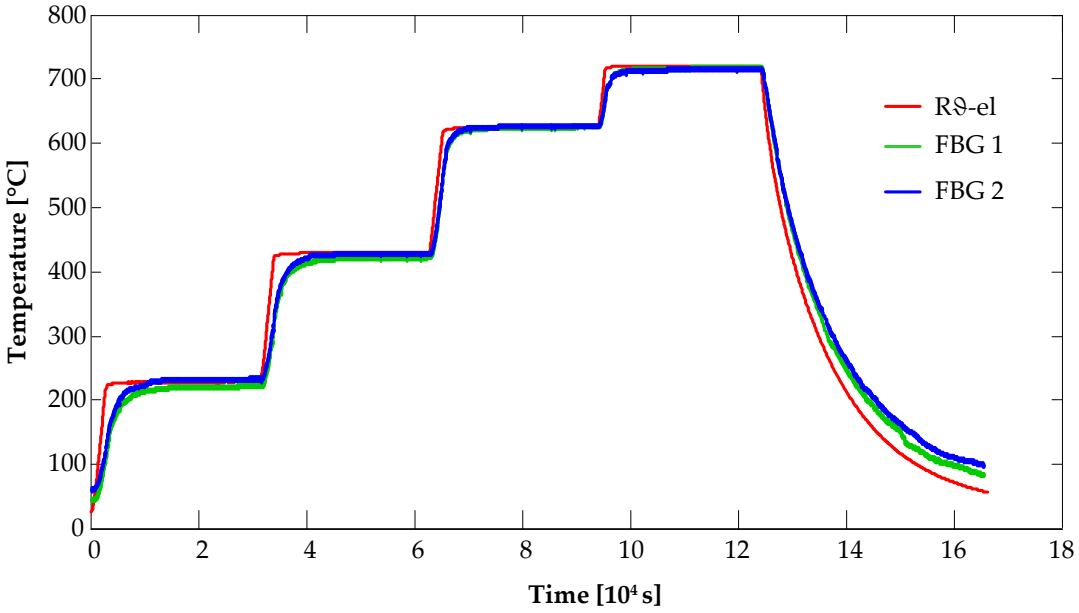

Fig. 8.38.: Temperature measurement results of the two FBG sensors inside a high temperature oven after calibration. The two sensors are mutually calibrated using values of the electrical reference temperature sensor $R_{\vartheta-el}$ and quadratic interpolation functions derived from measurement points of table 8.2.

9. Conclusion

Within this work two kinds of fiber laser based measurement systems have been in focus for further development towards space-borne equipment. The optical frequency comb (OFC) technology was examined in terms of suitability for applications in space. Among the various OFC generation techniques, two promising ultra-short pulsed lasers have been environmentally tested, the results are summarized in section 9.1. Design constraints for development of a future OFC for space applications are described by a development road-map in section 9.2.

In the field of optical fiber sensing, an interrogator bread-board based on a monolithic tunable laser diode has been designed and developed. The new sensing algorithms for Peak-Tracking and Time-of-Flight correction have been established in order to achieve a more flexible system with higher measurement performance. The measurement results, summarized in section 9.3, reveal the suitability of the interrogation system for replacing standard electric sensing. A development road-map for further development of the MG-Y based interrogator is given in section 9.4.

9.1. Discussion of OFC Development Results

This section summarizes the results of this work concerning the suitability of fiber-based optical frequency comb technology for space use. The following main conclusions have been derived from evaluation of measurement results and from experiences during operation of the systems. High priority is given to compatibility of the technology with expected space related requirements.

1. **Mode-locking principle**
   SESAM soliton mode-locking has proven higher robustness and better suitability than non-linear polarization rotation (NLPR) mode-locking. First, performance degradation of the NLPR laser output due to temperature and irradiation has been observed during the environmental tests (see chapters 7.4 and 7.5). The degradation results can result in a failure of OFC generation. Second, up to four actuators are needed for NLPR waveplates rotation. Single failure of one actuator results in total dysfunction of mode-locking search. SESAM mode-locking on the other hand works completely passive without moving parts and results in a less complex and more reliable OFC system. Third, SESAM mode-locking is based on polarization-maintaining (PM) fibers whereas NLPR requires the use of non-PM fibers. PM fibers yield higher robustness of the setup against temperature fluctuations and vibrations. Fourth, NLPR requires free-space optics for polarization control which makes the system susceptible to shock and vibrations leading to misalignment of the free-space optical components. SESAM mode-locking allows to build a all-in-fiber system without free-space optics that is alignment-free and thereby insensitive against shock and vibrations.

2. **Rare-earth doped fibers**
   The gain fibers are the most critical component of an OFCG in terms of qualification for space use. Gamma radiation tests revealed that the used Ytterbium-doped fiber is by a factor of three more radiation resistant than the Erbium-doped fiber (see chapter 7.5). Laser radiation tests have been performed wherein the gain fibers where irradiated during operation of the lasers. Illuminating the fibers with high intense light pulses demonstrated that photo bleaching occurs and cures radiation damages. Permanent operation of the OFCG in space could therefore prevent radiation damage of its gain fiber.

   Hydrogen loading yields radiation hardened Erbium-doped fibers that overcome the drawback of high radiation sensitivity. Since the characteristics of Erbium-doped fibers are dependent on types and concentrations of dopants and co-dopants like Aluminum, it is a challenging task to find the appropriate gain fiber. Hydrogen loading of the OFC's original Er-

bium fiber seems to be a straight-forward solution to achieve a radiation resistant laser.

3. **Performance**
   Test results, investigations, design considerations and an elaborated literature inquiry proved that OFCs based on rare-earth doped fiber lasers can be built compliant to the performance requirements in terms of accuracy and stability as clockwork of an optical atomic clock (see chapter 2.4). Although other types of OFCs show higher measurement performance (e.g. Titanium-sapphire OFC) and could possibly result in an even more compact system (e.g. microresontor OFC), the fiber laser based on SESAM soliton mode-locking seems to be the best overall solution. Due to its high maturity, alignment-free operation and an overall robust and reliable setup it reaches the highest performance in terms of space compatibility. Not only the laser itself, also comb stabilization and control electronics can be built as compact systems.

From the space engineering point of view, the investigated Erbium based and Ytterbium based lasers were not yet suitable for space utilization. The NLPR laser would require additional control loops based on monitoring and actuator mechanisms to achieve a stand-alone system for the use inside a spacecraft. Thereby NLPR mode-locking could be further developed so that operation in space would be possible. The SESAM soliton laser can be built more robust and with lower complexity due to fewer actuating and free-space components. This system is intrinsically stable without the need for redevelopment of control mechanisms and should be further developed towards a space-borne system.

9.2. OFC Development Roadmap

Following the conclusion of the previous section 9.1, an OFC based on a femtosecond fiber laser that deploys SESAM soliton mode-locking is the first choice for further development. All-in-waveguide designs (e.g. [72][157]) shall be developed and space qualified. Therefore the following development steps have to be carried out:

- **Development of OFC Breadboard - Optics**
  A breadboard should be developed based on a SESAM soliton mode-locking technology. The breadboard shall be based on a mechanical and optical redesign, taking into account results from preceding thermal, structural and optical simulations. The design trades between necessary remote control and monitoring mechanisms and automatic control in order to reduce system complexity to the minimum. Additionally to this work the entire OFC shall be developed, i.e. the femtosecond laser (OFCG) including spectral broadening, dispersion compensation and f-2f interferometer.

- **Development of OFC Breadboard - Electronics**
  Within this work, only the optics part of the OFCG was investigated and tested. The control electronic of an OFC has to be analyzed, designed and developed for power supply and control of the OFC. Electrical components shall be selected that can be replaced by qualified counterparts at a later development stage for system qualification. Redesign of laboratory electronic circuits in space compatible versions has to be performed.

- **Erbium / Ytterbium radiation hard fibers**
  The decision between an Erbium or Ytterbium based design will mainly be determined by the desired wavelength range. Components for an Erbium based design are commercially available in broad range and from several suppliers even though not always space qualified. If wavelengths below app. 900 nm are required, an Ytterbium based system may be a better choice since generation of the second harmonic and therefore additional complexity can be avoided. It should be investigated if radiation hardening techniques can be applied to Ytterbium fibers. After it has been decided between Erbium and Ytterbium, the appropriate fiber has to be identified and, if necessary, radiation hardened by e.g. hydrogen loading. The OFCG system can then be parameterized to the fiber (i.e. adjustment of pump power, dispersion control, ...).

- **OFC characteristics and performance**
  Dependent on the application, requirements for the OFC have to be derived for system parameterization. Wavelength range, line-width, stability, accuracy and power per mode etc. have to be identified analyzing the demands on an OFC as clockwork in an OAC. The achieved performance

of the OFC breadboard shall be officially verified e.g. by calibration at a national metrology institute.

The result of this work will provide a firm basis for further development of optical frequency combs based on fiber lasers for space applications.

9.3. Discussion of OFS Scanning Laser Development Results

The scanning laser interrogator system developed in this work has a high potential for a future FBG sensing system onboard a launcher or another spacecraft. Due to its compact all-in-fiber setup based on the monolithic MG-Y laser diode, no free-space or moving parts are necessary for sensor interrogation. The power supply, control and signal measurement electronic within this work was based on commercially available components for the breadboard development of the SL. Since the requirements for radiation hardness of components are low due to the short lifetime of launchers, the development was focused on system compliance with the required measurement performance.

The primary application for a future SL will be temperature measurement acquiring housekeeping data. Therefore the SL is best suited because of its broad optical output spectrum of more than 40 nm that allows to connect a high numbers of sensors to be measured sequentially. Furthermore, due to the developed Peak-Tracking and Time-of-Flight algorithms, measurement performance in terms of sample rate is increased. A maximum sensor sample rate of more than $f_{SR} > 4.5\,kHz/N_S$ has been achieved with the SL breadboard. Since the measurement rate for temperature sensing is usually limited to less than 10 Hz, up to several hundred FBG sensors can be measured by future versions of the SL interrogator.

The achieved measurement performance was $\pm 0.5\ K$ which is comparably to the accuracy of electrical sensing on launchers. The accuracy can be improved by further development according to section 9.4.

9.4. OFS Development Roadmap

Although the SL interrogator has demonstrated reliable measurement results, further development is necessary to come to a system suitable for spacecrafts. The following points not only focus on a system dedicated to launchers but sensing in spacecrafts in general.

- **Temperature stabilization of MG-Y laser**
  Due to the transient oscillations that occur when the laser is switched to a different output wavelength, the settling time required is up to 100 μs although the electronics of the SL could cope with switching rates of more than 1 MHz. The reason for high settling times are temperature changes of the laser diode chip because of varying input currents. The Peltier cooler is not capable of keeping the temperature constant due to thermal capacities between the cooler and the laser diode. This issue results in instable wavelengths that can occur randomly during operation of the SL interrogator (see figure 8.33). A solution to this problem could be the design and implementation of improved Peltier cooling within the laser diode.

- **Influence of Laser Polarization to Measurement Accuracy**
  Up to now polarization of the laser light has not been investigated. Since FBG sensors show birefringence, the measurement results depend on the polarization direction of the laser light. If polarization effects disturb the measurement accuracy to an error higher than allowed, a depolarizer at the output of the laser diode could be a solution. The use of polarization maintaining fibers is another possible way for avoiding polarization issues.

- **Improvement of Measurement Performance**
  Due to instable output wavelengths, i.e. output pulses which show a wavelength different to the wavelength stored in the look-up table, the accuracy of measurement results is reduced. Improved laser characterization that results in a LUT without instable wavelengths would improve accuracy. An etalon filter could be used as wavelength sensing device in order to implement a wavelength control loop. Improved temperature control of the laser diode (see section 8.6) could result in a LUT that is free

of instable wavelengths.

- **Laser Qualification**
  The impact of space environment to the laser diode has not been investigated until now. Since the structure of the laser diode chip shows gratings and nonlinear regions, radiation effects are likely. The level of damage is unknown and should be investigated by radiation testing. Furthermore the lifetime of the laser diode and the long-term stability of the output wavelengths have to be verified. Either the LUT and thereby the correlation between control currents and output wavelength has to stay constant throughout the mission lifetime or means of automated laser characterization have to be implemented.

- **SL Qualified Hardware Development**
  A detailed design phase is necessary to specify the requirements to the SL interrogator in terms of measurement performance (number of sensors, sample rate, measurement range, ...) and budget (size, volume, power consumption, ...). Based on this design, the laser, the supply, control and data acquisition electronics are built. Thereby procedures for wavelength stabilization, in order to avoid instable wavelengths, and hardware electronics that can be transferred to a space qualified version shall be developed. In parallel, environmental and lifetime tests of the laser should be carried out to ensure that the laser can cope with the expected environmental and mission related requirements.

The result of this work will provide a firm basis for further development of optical fiber sensing based on the MG-Y laser diode for space applications.

A. APPENDIX

A.1. Acknowledgment

This work has been performed in cooperation with Kayser-Threde GmbH in the frame of the following ESA and DLR projects:

- ESA 20071/06/NL/PM - Optical Frequency Comb: Critical Elements Predevelopment
- ESA 11446/05/NL/SFe - Fiber Optic Sensors for Structural Monitoring of the Ariane Launcher
- DLR FKZ 50QT0901 - Der Weg zu raumfahrttauglichen Frequenzkämmen
- DLR FKZ 50QT1001 - Entwicklung eines raumfahrtqualifizierbaren Frequenzkamms

The technology of optical atomic clocks has been investigated in the frame of the DLR project

- DLR FKZ 50NA0904 - Einsatz optischer Uhren in der Satellitennavigation

lead by Univ.-Prof. Dr. phil. nat. Urs Hugentobler, head of Forschungseinrichtung Satellitengeodäsie (FESG) at the Institute for Astronomical and Physical Geodesy, Technische Univerisität München.

Hydrogen loaded Erbium doped fibers have kindly been provided by Dr. Alexander L. Tomashuk, Deputy Director of the Fiber Optic Research Center (FORC), Moscow.

In the context of this work, the following publications (A.2) and student theses (A.3) were authored resp. supervised and are not cited formally.

A.2. Own Publications

- Plattner M.P., Müller M.S., Hoffmann L., Hirth F., Buck T.C., Koch A.W.: *A Versatile Fibre Optic Sensor Interrogation System for the Ariane Launcher Based on an Electro-optically Tunable Laser Diode.* Proceedings of International Conference on Space Optics, 14.-17.10.2008, Toulouse, France.
- Plattner M.P., Zeh T., Klein V., Koch A.W.: *Radiation Sensitivity of Ytterbium and Erbium Based Frequency Combs.* Proceedings of International Conference on Space Optics, 14.-17.10.2008, Toulouse, France.
- Plattner M.P., Hirth F., Müller M.S., Hoffmann L., Buck T.C., Koch A.W.: *Optimizing Performance of a Fiber Optic Sensor Interrogator by Time of Flight Measurement.* Proceedings of OPTO, 26.-27.05.2009, Nürnberg, Germany.
- Buck T.C., Müller M.S., Plattner M.P., Koch A.W.: *Performance analysis of interrogators for Fiber-Bragg-grating sensors based on arrayed waveguide gratings.* Proceedings of the SPIE Europe Optical Metrology Conference, 14.-18.06.2009, Munich, Germany.
- Plattner M.P., Brand C.N., Mair T., Schupfer S., Buck T.C., Koch A.W.: *Spectral Peak Tracking for Enhanced Fiber Optic Sensing.* Proceedings of the SPIE Europe Optical Metrology Conference, 14.-18.06.2009, Munich, Germany.
- Hugentobler U., Plattner M.P., Voithenleitner D., Heinze M., Klein V., Bedrich S.: *Optical Clocks in Future Global Navigation Satellites.* Proceedings of 2nd International Colloquium - Scientific and Fundamental Aspects of the Galileo Program, 14.-16.10.2009, Padua, Italy.
- Müller M.S., Hoffmann L., Bodendorfer T., Hirth F., Petit F., Plattner M.P., Buck T.C., Koch A.W.: *Fiber Bragg Grating Interrogation based on monolithic tunable laser diode.* IEEE Transactions on Instrumentation and Measurement 59(3), pp. 696-703, 03/2010.

- Plattner M.P., Hugentobler U., Voithenleitner D., Heinze M., Klein V., Kemmerle K., Bedrich S.: *Optical Clock Technology for Optimized Satellite Navigation.* Proceedings of EFTF, 13.-16.04.2010, Noordwijk, Netherlands.
- Plattner M.P., Zeh T., Koch A.W.: *Femtosekundenlaser-basierte Frequenzkämme für optische Atomuhren.* DGaO-Proceedings (ISSN: 1614-8436), 25.-29.05.2010, Wetzlar, Germany.
- Plattner M.P., Koch A.W., Zeh T., Reutlinger A.: *FBG-Sensor-Interrogator mit Time-of-Flight- und Peak-Tracking-Algorithmen.* Technisches Messen (77), pp. 342-348, 06/2010.
- Plattner M.P., Kemmerle K., Stuffler T.: *Optical Clock Technology for Space Applications.* Presentation at the 38th scientific assembly of the committee on space research COSPAR, 21.07.2010, Bremen, Germany.
- Plattner M.P., Buck T.C., Eder B., Reutlinger A., McKenzie I.: *Development of fiber optic sensing interrogators for launchers.* Proceedings of the International Conference on Space Optics, 04.-08.10.2010, Rhodos, Greek.

A.3. Supervised Student Theses

- Daniel Dorigo: *Report on Locking Mechanisms on Spacecrafts.* Advanced Seminar, Technische Universität München, 2008.
- Christoph Brand: *FPGA Programmierung des SMAFO-SL Sensorinterrogators.* Bachelor Thesis, Technische Universität München, 2009.
- He Chi: *Closed Loop Control of an Optical Laser Interferometer LISA Pathfinder based on LabVIEW Realtime.* Diploma Thesis, Technische Universität München, 2009.
- Daniel Dorigo: *Analysis on a Commercial Femtosecond Laser for Space Use.* Diploma Thesis, Technische Universität München, 2009.
- Matthias Grünefeld: *Entwicklung einer Flugeinheit zur On-Orbit-Verifikation eines Satelliten-Sensorbusses.* Diploma Thesis, Technische Universität München, 2009.
- Manuel Kofler: *Radiation Tests of Erbium and Ytterbium Based Ultra-short Pulsed Lasers.* Bachelor Thesis, Technische Universität München, 2009.
- Thomas Mair: *SMAFO Laser- und Detektionssystem, Design und Inbetriebnahme.* Bachelor Thesis, Technische Universität München, 2009.
- Philipp Putzer: *Thermal-vacuum Tests of Erbium and Ytterbium Based Ultra-short Pulsed Lasers.* Bachelor Thesis, Technische Universität München, 2009.
- Philipp Putzer: *Optical Frequency Combs - Literature Inquiry.* Advanced Seminar, Technische Universität München, 2009.
- Stefan Schupfer: *SMAFO Transimpedance Amplifier Selection.* Advanced Seminar, Technische Universität München, 2009.
- Thomas Ganka: *Optical Frequency Comb - F-2f Interferometer Breadboard Development* Master Thesis, University of Applied Science Munich, 2010.
- Manuel Kofler: *Optical Frequency Combs - Component Selection.* Advanced Seminar, Technische Universität München, 2010.

- Hong Li: *Process Monitoring for Smart Tooling.* Diploma Thesis, University of Applied Science Munich, 2010.
- Philipp Putzer: *Optical Frequency Comb - Stabilization Electronics Breadboard Development* Diploma Thesis, Technische Universität München, 2010.
- Stefan Schupfer: *DSP Automation of the SMAFO Scanning Laser Sensor Interrogator.* Bachelor Thesis, Technische Universität München, 2010.
- Martin Trowbridge: *Femtosecond Laser Based Measurements for Space Technology.* Diploma Thesis, University of Applied Science Munich, 2010.

A.4. Glossary

ACES	Atomic Clock Ensemble in Space
ACF	Auto Correlation Function
ADC	Analog to Digital Converter
ASE	Amplified spontaneous emission
AWG	Arrayed Waveguide Grating
CC	Current Control
CDU	Control and Detection Unit
CEO	Carrier Envelope Offset
CPU	Central Processing Unit
DAC	Digital to Analog Converter
DLR	Deutsches Zentrum für Luft- und Raumfahrt
DSP	Digital Signal Processor
DUT	Device Under Test
ECSS	European Cooperation for Space Standardization
EF	Edge Filter
EMC	Electromagnetic Compatibility
EMIF	External Memory Interface
EN	European Norm
Er	Erbium
ESA	European Space Agency
FBG	Fiber Bragg Grating
FCU	Fiber Coupler Unit
FORC	Fiber Optic Research Center
FOS	Fiber Optic Sensing
FPGA	Field Programmable Gate Array
FSR	Free Spectral Range
GEO	Geostationary Earth Orbit
GIOVE	Galileo In-Orbit Verification
GNSS	Global Navigation Satellite System
GVD	Group Velocity Dispersion
HNLF	Highly Non-Linear Fiber
ISO	International Organization for Standardization
KLM	Kerr-Lense Modelocking

LDU	Laser and Detection Unit
LEO	Low Earth Orbit
LUT	Look-Up Table
MEO	Medium Earth Orbit
MG-Y	Modulated Grating Y-structure
NASA	National Aeronautics and Space Administration
NF	Noise Floor
NIEL	Non-Ionizing Energy Loss
NL	Non-Linear
NLPR	Non-Linear Polarization Rotation
OAC	Optical Atomic Clock
OFC	Optical Frequency Comb
OFCG	Optical Frequency Comb Generator
OSA	Optical Spetrum Analyzer
PCF	Photonic Crystal Fiber
PFD	Phase Frequency Detector
PLL	Phase Locked Loop
PM	Polarization Maintaining
PPLN	Periodically-Poled Lithium Niobate
PROBA	Project for On-Board Autonomy
PT	Peak-Tracking
PWM	Pulse Width Modulator
REP	Repetition rate
SAM	Saturable Absorber Mirror
SCA	Special Centroid Algorithm
SEE	Single Event Effect
SEL	Single Event Latchup
SESAM	Semiconductor Saturable Absorber Mirror
SET	Single Event Transient
SEU	Single Event Upset
SL	Scanning Laser
SNR	Signal to Noise Ratio
SOC	Space Optical Clocks
SPENVIS	Space Enviroment Invormation Center
SPM	Self-Phase Modulation

TEC	Temperature Controller
TID	Total Ionizing Dose
TML	Total Mass Loss
ToF	Time of Flight
TRL	Technology Readiness Level
TV	Thermal Vacuum
ULE	Ultra Low Expansion
UV	Ultra-Violett
VGA	Variable Gain Amplifier
Yb	Ytterbium

Bibliography

[1] *All Things Photonic - The CVI Melles Griot Technical Guide*. CVI-MellesGriot, 2011.

[2] Adler F., et al.: *Phase-Locked Two-Branch Erbium-Doped Fiber Laser System for Long-Term Precision Measurements of Optical Frequencies*. Optics Express, 12(24):5872–5880, November 2004.

[3] Agrawal, G.P.: *Applications of Nonlinear Fiber Optics*. Academic Press, 2001.

[4] Agrawal, G.P.: *Nonlinear Fiber Optics*. Academic Press, 2001.

[5] Alnis J., et al.: *Subhertz Linewidth Diode Lasers by Stabilization to Vibrationally and Thermally Compensated Ultralow-Expansion Glass Fabry-Pérot Cavities*. Physical Review A, 77:053809 (9pgs), 2008.

[6] Arissian L., Diels J. C.: *Carrier to Envelope and Dispersion Control in a Cavity with Prism Pairs*. Physical Review A, 75(1):013814–1 to 013814–10, 2007.

[7] Armani D.K., et al.: *Ultra-High-Q Toroid Microcavity on a Chip*. Nature, 421:925–928, February 2003.

[8] Arrigoni M., et al.: *Aktive Phasenstabilisierung zur Erzeugung kurzer Laserpulse und Frequenzkämme*. Photonik, 4:34–36, 2009.

[9] Astronomical Institute, University of Berne: *Bernese GPS Software*. `http://www.bernese.unibe.ch/`.

[10] Audoin C., Guinot B.: *The Measurement of Time*. Cambridge University Press, 2001.

[11] Balling P., et al.: *Femtosecond Frequency Comb based Distance Measurement in Air*. Optics Express, 17(11):9300–9313, May 2009.

[12] Barrett, C.: *Fractional/Integer-N PLL Basics*. Technical report, Texas Instruments, August 1999.

[13] Barth J.L., Dyer C.S., Stassinopoulos E.G.: *Space, Atmospheric, and Terrestrial Radiation Environments*. IEEE Transactions on Nuclear Science, 50(3):466–482, June 2003.

[14] Bergmahns F., et al.: *Radiation hardness of fiber-optic sensors for monitoring and remote handling applications in nuclear environments*. Proceedings of SPIE International Symposium on Industrial and Environmental Monitors and Biosensors Harsh Environment Sensors, 3538:28–39, November 1998.

[15] Bergtold, F.: *Schaltungen mit Operationsverstärkern*, volume 2. Oldenbourg Wissenschaftsverlag GmbH, 1973.

[16] Bergtold, F.: *Schaltungen mit Operationsverstärkern*, volume 1. Oldenbourg Wissenschaftsverlag GmbH, 2nd edition, 1973.

[17] Black, E.D.: *An Introduction to Pound–Drever–Hall Laser Frequency Stabilization*. American Journal of Physics, 69(1):79–87, January 2001.

[18] Boas G. (ed), et al.: *Photonics in space*. Photonics Spectra, pages 30–33, December 2010.

[19] Borgermans P., et al.: *Dosimetry with Optical Fibres: Results for Pure Silica, Phosphorous and Erbium doped Samples*. Proceedings of SPIE on Fiber Optic Sensor Technology II, 4204:151–160, March 2001.

[20] Boyd, R.W.: *Nonlinear Optics*. Academic Press, 3rd edition, May 2008.

[21] Brichard B., et al.: *Dedicated Optical Fibres for Dosimetry Based on Radiation-Induced Attenuation: Experimental Results*. Proceedings of SPIE on Photonics for Space and Radiation Environments EUROPTO, 3872:36–42, September 1999.

[22] Brichard B., et al.: *Study of the Radiation-Induced Optical Sensitivity in Erbium and Aluminium doped Fibres*. Proceedings on Radiation and its Effect on Components and Systems RADECS, pages 35–38, 2003.

[23] Brichard B., et al.: *True Dose Rate Enhancement Effect in Phosphorous doped Fibre Optic Radiation Sensors*. Proceedings of SPIE on 2nd European Workshop on Optical Fibre Sensors, 5502:184–187, 2004.

[24] Cacciapuoti, L.: *Aces mission concept and scientific objectives*. Technical report, ESA-ESTEC, 2007.

[25] Caussanel M., et al.: *Assessing Space Radiation Environment Effects on Erbium-doped Fiber Amplifier*. Proceedings on Radiation and its Effects on Components and Systems RADECS, pages 533–536, September 2003.

[26] Chou C.W., et al.: *Frequency Comparison of Two High-Accuracy Al+ Optical Clocks*. Physical Review Letters, 104(7):70802–70805, February 2010.

[27] Coen S., et al.: *White-Light Supercontinuum Generation with 60-Ps Pump Pulses in a Photonic Crystal Fiber*. Optics Letters, 26(17):1356–1358, September 2001.

[28] Cundiff, S.T.: *New generation of combs*. Nature, 450(20):1175–1176, December 2007.

[29] CVI-MellesGriot: *Dispersion Equations*. Product Catalog, Appendix, page 6, 2011.

[30] Daly E., et al.: *Standards for Space Radiation Environments and Effects*. Proceedings of 7th European Conference on Radiation and its Effects on Components and Systems RADECS, pages 175–180, 2003.

[31] Del'Haye P., et al.: *Optical Frequency Comb Generation From a Monolithic Microresonator*. Nature, 450:1214–1217, December 2007.

[32] Diddams, S.A.: *Optical Frequency Combs for Space? Some Considerations, Projections and Possibilities*. Presentation at the OFCS Workshop at NPL, October 2006.

[33] Diddams S.A., et al.: *An Optical Clock based on a Single Trapped 199Hg+ Ion*. Science, 193:825–828, August 2001.

[34] Diels J.-C., Rudolph W.: *Ultrashort Laser Pulse Phenomena*. Academic Press, 2nd edition, 2006.

[35] Drever R.W.P., et al.: *Laser Phase and Frequency Stabilization Using an Optical Resonator*. Applied Physics B, 31:97–105, February 1983.

[36] Dyer C.S., Hopkinson G.R.: *Space Radiation Effects For Future Technologies and Missions*. Technical report, QinetiQ Space Department, 2001.

[37] Eaton, D.F.: *Nonlinear Optical Materials*. Science, 19:281–287, July 1991.

[38] Ecke W., et al.: *Fibre Optic Sensor Network for Spacecraft Health Monitoring*. Measurement Science and Technology, 12(7):947, January 2001.

[39] ECSS: *ECSS-E-10-03A Testing*. February 2002.

[40] ECSS: *ECSS-Q-ST-30-11C Derating - EEE components*. July 2008.

[41] ECSS: *ECSS-E-HB-10-02A Verification Guidelines*. December 2010.

[42] Eichler J., Eichler H. J.: *Laser*. Springer, 2006.

[43] Ellis A.B., et al.: *Teaching General Chemistry: A Materials Science Companion*. An American Chemical Society Publication, May 1993.

[44] ESA: *The space environment information system spenvis*. `http://www.spenvis.oma.be/`.

[45] ESA: *Technology Readiness Levels Handbook For Space Applications*, September 2008.

[46] ESA-ESTEC: *ECSS System - Description, Implementation and General Requirements*, July 2008.

[47] ESA-ESTEC: *Release Note for ECSS Standards CD-ROM*. Technical report, European Cooperation for Space Standardization, April 2010.

[48] ESCC, European Space Components Coordination: *Total dose steady-state irradiation test method*, March 2007.

[49] Esfandiari, A.: *Magnetic quadrupole moment*. `http://en.wikipedia.org/wiki`.

[50] Farell T., et al.: *Novel FBG interrogation technique for achieving < 100 nstrain accuracies at remote distances > 70 km*. Procedings of SPIE of Opto-Ireland 2005: Optical Sensing and Spectroscopy, 5826:663–669, 2005.

[51] Fermann M.E., et al.: *Fiber-lasers for ultrafast optics*. Applied Physics B, 65:259–275, April 1997.

[52] Fernandez A.F., Brichard B., Berghmans E.: *Long-term radiation effects on fiber Bragg grating temperature sensors in mixed gamma neutron fields*.

Proceedings of Conference on Radiation and its Effects on Components and Systems RADECS, September 2003.

[53] Figger H., Meschede D., Zimmermann C.: *Laser physics at the limits*. Springer, 2002.

[54] Fleetwood D.M., et al.: *Physical mechanisms contributing to enhanced bipolar gain degradation at low dose rates*. IEEE Transactions on Nuclear Science, 41(6):1871–1883, December 1994.

[55] Fox B.P., et al.: *Gamma Radiation Effects in Yb-Doped Optical Fiber*. Proceedings of SPIE on Conference of Fiber Lasers IV: Technology, Systems, and Applications, 6453, 2007.

[56] Fracis Y.T.S., Shizhuo Y.: *Fiber Optic Sensors*. Marcel Dekker AB, 2002.

[57] Friebele E.J., et al.: *Optical Fiber Sensors For Spacecraft Applications*. Smart Materials and Structures 8 (1999) 813–838., 8:813–838, August 1999.

[58] Förste B., Öing S.: *EMV-Design Richtlinien*. Franzis' Verlags GmbH, 2003.

[59] Fukada C., et al.: *Gammy-ray irradiation durability of erbium doped fibres*. IEEE Transactions on Nuclear Science, 30(16):1342–1344, 1994.

[60] Georgi W., Metin E.: *Einfuehrung in LabVIEW*. Fachbuchverlag Leipzig, 2007.

[61] Gill P., et al.: *Feasibility and applications of optical clocks as frequency and time references in ESA deep space stations*. Technical report, NPL, PTB, Timetech, DLR, 2007.

[62] Gill P., Margolis H.S., et al.: *Optical Atomic Clocks for Space*. Technical report, National Physics Laboratory, 2008.

[63] Gill P., Riehle F.: *On Secondary Representations of the Second*. Proceedings of the European Time and Frequency Forum EFTF, 2006.

[64] Girard S., et al.: *Radiation Effects on Ytterbium- and Ytterbium/Erbium-Doped Double-Clad Optical Fibers*. IEEE Transactions on Nuclear Science, 56(6):3293–3299, December 2009.

[65] Gusarov A., et al.: *Effect of the Fiber Coating on the Radiation Sensitivity of Type I FBGs*. IEEE Photonics Technology Letters, 20(21):1802–1804, November 2008.

[66] Gusarov A., Brichard B., Nikogosyan D.N.: *Gamma-Radiation Effects on Bragg Gratings Written by Femtosecond UV Laser in Ge-Doped Fibers*. IEEE Transactions On Nuclear Science, 57(4):2024–2028, August 2010.

[67] Gusarov A.I., et al.: *High Total Dose Radiation Effects on Temperature Sensing Fiber Bragg Gratings*. IEEE Photonics Technology Letters, 11(9):1159–1161, September 1999.

[68] Gusarov A.I., et al.: *Behavior of Fibre Bragg Gratings Under High Total Dose Gamma Radiation*. IEEE Transactions on Nuclear Science, 47(3):461–465, August 2002.

[69] Gusarov A.I., et al.: *Stabilization of Fiber Bragg Gratings Against Gamma Radiation*. IEEE Transactions on Nuclear Science, 55(4):2205–2212, August 2008.

[70] Gusarov A.I., et al.: *Gamma Radiation Induced Short-Wavelength Shift of the Bragg Peak in Type I Fiber Gratings*. IEEE Transactions On Nuclear Science, 57(6):3775–3778, December 2010.

[71] Harland D.M., Lorenz R.D.: *Space Systems Failures - Disasters and Rescues of Satellites, Rockets and Space Probes*. Springer, 2005.

[72] Hartl I., et al.: *Integrated Self-Referenced Frequency-Comb Laser Based On A Combination Of Fiber And Waveguide Technology*. Optics Express, 13(17):6490–6496, August 2005.

[73] Hawthorn C.J., Weber K.P., Scholten R.E.: *Littrow configuration tunable external cavity diode laser with fixed direction output beam*. Review of Scientific Instruments, 72(12):4477–4479, December 2001.

[74] Henschel H., et al.: *Radiation induced loss of Rare Earth doped silica fibres*. IEEE Transactions on Nuclear Science, 45(3):1552–1557, June 1998.

[75] Henschel H., Köhn O., Weinand U.: *Radiation Hardening of Pure Silica Optical Fibers by High-Pressure Hydrogen Treatment*. IEEE Transactions On Nuclear Science, 49(3):1401–1409, June 2002.

[76] Henschel H., Kuhnhenn J., Weinand U.: *Radiation Hard Optical Fibers*. In *Optical Fiber Communication Conference*, 2005.

[77] Hill K.O., Meltz G.: *Fiber Bragg Grating Technology Fundamentals and Overview*. Journal Of Lightwave Technology, 15(8):1263–1276, August 1997.

[78] Holmes-Siedle A., Adams L.: *Handbook of radiation effects*. Oxford Science Publications, 1993.

[79] Holzwarth R., et al.: *Optical Frequency Synthesizer for Precision Spectroscopy*. Physical Review Letters, 85(11):2264–2267, September 2000.

[80] Itano W.M., et al.: *Optical frequency standards based on mercury and aluminum ions*. Proceedings of SPIE, 6673:667303 (11pgs), 2007.

[81] Johns S.T., et al.: *Temporal responses of actively modelocked erbium-doped fibre laser irradiated by gamma-rays*. Electronics Letters, 39(18):1310 – 1312, September 2003. Referenzen mit drin :).

[82] Johnston A.H., Rax B.G., Lee C.I.: *Enhanced Damage in Linear Bipolar Integrated Circuits at Low Dose Rate*. IEEE Transactions on Nuclear Science, 42(6):1650–1659, Dezember 1995.

[83] Johnston A.H., Rax B.G., Lee C.I.: *Enhanced Damage in Linear Bipolar Devices at Low Dose Rate: Effects at Very Low Dose Rates*. IEEE Transactions on Nuclear Science, 43(6):3049–3059, December 1996.

[84] K., Predehl: *Frequenzkämme für Weltraumanwendungen*. Diplomarbeit, Ludwig Maximilian Universität München, 2006.

[85] Keller, U.: *Recent Developments In Compact Ultrafast Lasers*. Nature, 424:831–838, August 2003.

[86] Keller, U.: *Sättigbare Halbleiter-Absorberspiegel für ultraschnelle Festkörperlaser*. Photonik, 4:44–47, 2004.

[87] Kersey A.D., et al.: *Fiber Grating Sensors*. IEEE Journal Of Lightwave Technology, 15(8):1442– 1463, August 1997.

[88] Klein H., et al.: *Optical Clocks for ESA Deep Space Ground Stations*, 2007.

[89] Kneubuehl F.K., Sigrist M.W.: *Laser*. Teubner, 2005.

[90] Koke S., et al.: *Direct Frequency Comb Synthesis With Arbitrary Offset And Shot-Noise-Limited Phase Noise*. Nature Photonics, 4:462–465, July 2010.

[91] Komarov A., Leblond H., Sanchez F.: *Modelling of Harmonic Passive Mode-Locking of Fiber Laser with Nonlinear Polarization Rotation*. Proceedings of the 7th International Conference Transparent Optical Networks, 2:295–298, September 2005.

[92] Kories R., Schmidt Walter H.: *Taschenbuch der Elektrotechnik*. Verlag Harri Deutsch, 4th edition, 200.

[93] Kriedte, W.: *ECSS - A Single Set of European Space Standards*. In Proceedings of Conference on Spacecraft Structures, Materials & Mechanical Testing, pages 321–327, June 1996.

[94] Krieger, J.: *Laser Doppler Cooling*. `http://de.wikipedia.org/wiki/Datei:Laseforce.png`.

[95] Krieger, J.: *Setup of a MOT*. `http://de.wikipedia.org/wiki/Bild:Cobalt-60_Decay_Scheme.svg`.

[96] Kärtner F.X., Au J. aus der, Keller U.: *Mode-Locking with Slow and Fast Saturable Absorbers—What's the Difference?* IEEE Journal Of Selected Topics In Quantum Electronics, 4(2):159–168, April 1998.

[97] Kruzelecky R.V., et al.: *Fiber-Optic Sensor Demonstrator (FSD) Integration with Proba-2*. 7th International Conference on Space Optics, 2008.

[98] Kruzelecky R.V., et al.: *Fiber-Optic Sensor Demonstrator (FSD) Preliminary Test Results on Proba-2*. 8th International Conference on Space Optics, 2010.

[99] Kubina P., et al.: *Long-term comparison of two fiber based frequency comb systems*. Optics Express, 13(3):904–909, February 2005.

[100] Kuchling, H.: *Taschenbuch der Physik*. Fachbuchverlag Leipzig, 17th edition, 2001.

[101] Ley W., Wittmann K., Hallmann W.: *Handbuch der Raumfahrttechnik*. Hanser, 2008.

[102] Lindner H., Brauer H., Lehmann C.: *Taschenbuch der Elektrotechnik und Elektronik*. Fachbuchverlag Leipzig, 7th edition, 2001.

[103] Litchinitser N., Sumetsky M., Westbrook P.: *Fiber Based Dispersion Compensation*. Optical and Fiber Communications Reports, 5:379–423, 2007.

[104] Locke C.R., et al.: *Frequency stabilisation of a fibre-laser comb using a novel microstructured fibre*. Optics Express, 17:5897–5904, 2009.

[105] Lopez, S.: *The Universe Measured with a Comb*. Science, 321:1301–1302, September 2008.

[106] Lutz H., Wendt W.: *Taschenbuch der Regelungstechnik*. Verlag Harri Deutsch, 5th edition, 2003.

[107] M., Bass (editor): *Handbook of Optics*. Optical Society of America, 1995.

[108] Ma L.-S., et al.: *International Comparisons of Femtosecond Laser Frequency Combs*. IEEE Transactions On Instrumentation And Measurement, 54(2):746–749, April 2005.

[109] Maas D.J.H.C., et al.: *High Precision Optical Characterization of Semiconductor Saturable Absorber Mirrors (SESAMs)*. Optics Express, 16(10):7571–7579, 2008.

[110] Mankins, J.C.: *Technology Readiness Levels - White Paper*. Technical report, Advanced Concepts Office NASA, April 1995.

[111] Margolis, H.S.: *Frequency metrology and clocks*. Journal Of Physics B: Atomic, Molecular And Optical Physics, 42:154017 (16pp), July 2009.

[112] Margolis, H.S.: *Trapped ion optical clocks*. European Physical Journal Special Topics, 172:97–107, 2009.

[113] Margolis, H.S.: *Optical frequency standards and clocks*. Contemporary Physics, 51(1):37–58, 2010.

[114] Margolis H.S., et al.: *Hertz-Level Measurement of the Optical Clock Frequency in a Single 88Sr+ Ion*. Science, 306:1355–1358, November 2004.

[115] Maxim: *How to Control and Compensate a Thermoelectric Cooler (TEC)*. Technical Report AN3318, Maxim, September 2004.

[116] McKenzie I., Karafolas N.: *Fiber Optic Sensing in Space Structures: The Experience of the European Space Agency*. Procedings of SPIE on 17th International Conference on Optical Fiber Sensors, 5855:262–269, 2005.

[117] McNamara P., Vitale S., Danzmann K.: *LISA Pathfinder*. Classical and Quantum Gravity, 25(11), June 2008.

[118] Mei M., Holzwarth R., Kozma I.Z.: *Frequenzkämme und Frequenzverteilung für Anwendungen in Wissenschaft und Industrie*. Photonik, 5:58–61, 2006.

[119] Miller, G.D.: *Periodically Poled Lithium Niobate: Modeling, Fabrication, And Nonlinear-Optical Performance*. Ph. D. thesis at the University of Stanford, 1998.

[120] Moudrak A., et al.: *Future Time - Opportunities for Using Optical Clocks in GNSS Systems*. Inside GNSS, pages 45–50, September/October 2008.

[121] Nassau, K.: *The origins of color in minerals*. American Mineralogist, 63:219–229, 1978.

[122] Newbury N.R., Washburn B.R.: *Theory of the Frequency Comb Output From a Femtosecond Fiber Laser*. IEEE Journal Of Quantum Electronics, 41(11):1388–1402, November 2005.

[123] O'Bryan M.V., et al.: *Radiation Damage and Single Event Effect Results for Candidate Spacecraft Electronics*. Radiation Effects Data Workshop, 2000.

[124] OFS: *Highly Non-Linear Fiber*. May 2004.

[125] Oldham T.R., McLean F.B.: *Total Ionizing Dose Effects in MOS Oxides and Devices*. IEEE Transactions on Nuclear Science, 50(3):483–499, June 2003.

[126] Oppenheim A.V., Willsky A.S.: *Signale und Systeme*. VCH Verlagsgesellschaft, 2nd edition, 1992.

[127] Optics, OZ: *ASE Broadband Light Source*. March 2010. `http://www.ozoptics.com`.

[128] Othonos A., Kalli K.: *Fiber Bragg gratings*. Artech House Inc, 1999.

[129] Ott, M.: *Fiber Laser Components Technology Readiness Overview NASA Electronic Parts and Packaging Program*. Technical report, NASA Goddard Space Flight Center, March 2003.

[130] Ott, M.: *Radiation Effects Expected for Fiber Laser/Amplifier Rare Earth Doped Optical Fiber*. Technical report, NASA Goddard Space Flight Center, March 2004.

[131] Ott, M.: *Validation of Commercial Fiber Optic Components for Aerospace Environments*, March 2005.

[132] Ott, M.: *Space Flight Applications of Optical Fiber; 30 Years of Space Flight Success*. Avionics, Fiber-Optics and Photonics (AVFOP) Technology Conference, September 2010.

[133] Ott, M.N.: *Radiation Effects Data On Commercially Available Optical Fiber: Database Summary*. Nuclear And Space Radiation Effects Conference, July 2002.

[134] Paschotta, R.: *Field Guide to Laser Pulse Generation*. SPIE Press Book, 2008.

[135] Paschotta R., Keller U.: *Passive Mode Locking With Slow Saturable Absorbers*. Applied Physics B, 73:653–662, November 2001.

[136] Paul, W.: *Electromagnetic traps for charged and neutral particles*. Review of Modern Physics, 62:531–540, 1990.

[137] Pease, R.L.: *Total Ionizing Dose Effects in Bipolar Devices and Circuits*. IEEE Transactions on Nuclear Science, 50(3):539–551, June 2003.

[138] Peik E., Sterr U.: *The Development of Accurate Optical Clocks*. PTB Mitteilungen: QUEST - Centre for Quantum Engineering and Space-Time Research at the PTB, 119(2):25–32, 2009.

[139] Perez, E.: *Ariane 5 - User's Manual*. Arianespace, 5th edition, July 2008.

[140] Pfau, B.: *Formelsammlung Thermodynamik*. Technical report, Hochschule Darmstadt, 2008.

[141] Phillips, W.D.: *Laser cooling and trapping of neutral atoms*. Reviews of Modern Physics, 70(3):721–741, July 1998.

[142] Photonics, NKT: *Supercontinuum generation in photonic crystal fibers*. July 2009.

[143] Rade L., Westergren B., Vachenauer P.: *Springers Mathematische Formeln. Taschenbuch für Ingenieure, Naturwissenschaftler, Wirtschaftswissenschaftler*. Springer, 3rd edition, 2000.

[144] Ranka J.K., Windeler R.S., Stentz A.J.: *Visible continuum generation in air–silica microstructure optical fibers with anomalous dispersion at 800 nm*. Optics Letters, 25(1):25–27, January 2000.

[145] Rax B.G., Johnston A.H., Miyahira T.: *Displacement Damage in Bipolar Linear Integrated Circuits*. IEEE Transactions on Nuclear Science, 46(6):1660–1665, December 1999.

[146] Reichert J., et al.: *Measuring the frequency of light with mode-locked lasers*. Optics Communications, 172:59–68, December 1999.

[147] Riehle, F.: *Frequency Standards*. Wiley-VCH, 2004.

[148] Robertson G.J., et al.: *GIOVE-B Satellite Design and Performance Validation*. Institute of Navigation (ION) GNSS Conference, September 2009.

[149] Rodgers D., et al.: *Galileo Radiation Environment from Giove-A and -B*, 2008.

[150] Rosenband T., et al.: *Frequency Ratio of Al+ and Hg+ Single-Ion Optical Clocks; Metrology at the 17th Decimal Place*. Science, 319:1808–1812, 2008.

[151] Rullière, C.: *Femtosecond laser pulses*. Springer, 2005.

[152] Russell, P.St.J.: *Photonic-Crystal Fibers*. Journal Of Lightwave Technology, 24(12):4729–4749, December 2006.

[153] Rusu, M.: *Frequency Conversion Using Ultrafast Fiber Lasers*. PhD thesis, Tampere University of Technology, 2006.

[154] Saleh B.E.A., Teich M.C.: *Fundamentals of photonics*. Wiley Series in Pure and Applied Optics, 2nd edition, 2007.

[155] Salomon Ch., et al.: *Laser Stabilization at the Millihertz Level*. Journal of Optical Society of America B, 5(8):1576–1587, August 1988.

[156] Sauerbrey, R.: *Nichtlineare optik - vorlesungsskript*. Technical report, TU Dresden, 2007.

[157] Schibli T.R., et al.: *Frequency metrology with a turnkey all-fiber system*. Optics Letters, 29(21):2467–2469, November 2004.

[158] Schibli T.R., et al.: *Optical frequency comb with submillihertz linewidth and more than 10W average power*. Nature Photonics, 2:355–359, June 2008.

[159] Schiller S., et al.: *Optical Clocks in Space*. Nuclear Physics B, 166:300–302, 2007.

[160] Schiller S., et al.: *Einstein Gravity Explorer–A Medium-Class Fundamental Physics Mission*. Experimental Astronomy, 23(2):573–610, November 2008.

[161] Schiller S., et al.: *Space Optical Clocks (SOC) - Midterm Report*. Technical report, ESA, DLR, September 2008.

[162] Schmidt P.O., et al.: *Quantum Logic for Precision Spectroscopy*. PTB Mitteilungen: QUEST - Centre for Quantum Engineering and Space-Time Research at the PTB, 119(2):54–59, 2009.

[163] Schmitt-Landsiedl, D.: *Elektronische Bauelemente*. Lehrstuhl für Technische Elektronik, 2003.

[164] Schruefer, E.: *Elektrische Messtechnik*. Hanser, 2001.

[165] Scialdone J., Isaac P., Clatterbuck C. Hunkeler R.: *Material Total Mass Loss in Vacuum Obtained from Various Outgassing Systems*. Technical report, NASA Goddard Space Flight Center, July 2000.

[166] Siegman, A.E.: *Lasers*. University Science Books, 1986.

[167] Srour J.R., Marshall C.J., Marshall P.W.: *Review of Displacement Damage Effects in Silicon Devices*. IEEE Transactions on Nuclear Science, 50(3):653–670, June 2003.

[168] Srour J.R., McGarrity J.M.: *Radiation Effects on Microelectronics in Space*. Proceedings of the IEEE, 76(11):1443–1469, November 1988.

[169] Steinmetz T., et al.: *Laser Frequency Combs for Astronomical Observations*. Science, 321:1335–1337, September 2008.

[170] Steinmeyer, G.: *A review of ultrafast optics and optoelectronics*. Journal Of Optics A: Pure And Applied Optics, 5:R1–R15, 2003.

[171] Stenger J., et al.: *Ultraprecise Measurement of Optical Frequency Ratios*. Physical Review Letters, 88(7):073601 (4pgs), February 2002.

[172] Stumpf M.C., et al.: *Self-Referencable Frequency Comb From A 170-Fs, 1.5-Micrometer Solid-State Laser Oscillator*, November 2009.

[173] Swann W.C., et al.: *Fiber-laser frequency combs with subhertz relative linewidths*. Optics Letters, 21(20):3046–3048, October 2006.

[174] Swann W.C., et al.: *Residual stability of a fiber-based frequency comb*. Conference on Lasers and Electro-Optics CLEO, 2007.

[175] Syntune, AB: *Syntune widely tunable laser technology*. Technical report, AB Syntune, 2005.

[176] Tamura K., et al.: *Technique for obtaining high-energy ultrashort pulses from an additive-pulse mode-locked erbium-doped fiber ring laser*. Optics Letters, 19(1):46–48, January 1994.

[177] Tauser F., Leitenstorfer A., Zinth W.: *Amplified femtosecond pulses from an Er:fiber system: Nonlinear pulse shortening and selfreferencing detection of the carrier-envelope phase evolution*. Optics Express, 11(6):594–600, March 2003.

[178] Taylor, E.W.: *Space and Enhanced Radiation Induced Effects in Key Photonic Technologies*. Proceedings of IEEE Aerospace Conference, 3, 1999.

[179] Taylor E.W., et al.: *Gamma-ray induced effects in Erbium doped fiber optic ampfliers*. Proceedings of SPIE on Conference of Photonics for Space Environments VI, 3440:16–23, July 1998.

[180] Taylor E.W., et al.: *Overview Of Photonic Materials And Components For Application In Space Environments*. EUROPTO Conference on Photonics for Space and Radiation Environments, pages 72–83, September 1999.

[181] Thorlabs, Inc.: *Periodically Poled Lithium Niobate (PPLN) - Tutorial*. Thorlabs Catalog, pages 686–688, 2010.

[182] Tini, Aerospace: *Frangibolt actuator*. `http://www.tiniaerospace.com`.

[183] Titus J.L., Emily D., Krieg J.F. et al.: *Enhanced Low Dose Rate Sensitivity (ELDRS) of Linear Circuits in a Space Environment*. IEEE Transactions on Nuclear Science, 46(6):1608–1615, December 1999.

[184] U. Keller, et al.: *Semiconductor Saturable Absorber Mirrors (SESAM's) for Femtosecond to Nanosecond Pulse Generation in Solid-State Lasers*. IEEE Journal of Selected Topics in Quantum Electronics, 2(3):435–453, 1996.

[185] Udem Th., et al.: *Accurate Measurement Of Large Optical Frequency Differences With A Mode-Locked Laser*. Optics Letters, 24(13):881–883, July 1999.

[186] Udem Th., Holzwarth R., Hänsch T.W.: *Optical Frequency Metrology*. Nature, 416:233–237, March 2002.

[187] Vasilescu, G.: *Electronic noise and interfering signals*. Springer, 2005.

[188] Waller P., et al.: *In-Orbit Performance Assessment Of Giove Clocks*. In *Proceedings of the 40th Precise Time and Time Interval (PTTI) Systems and Applications Conference*, December 2008.

[189] Wesstroem J.-O., et al.: *Design of a widely tunabel modulated grating y-branch laser using the additive vernier effect for improved super-mode selection*. Proceeding of 18th IEEE International Semiconductor Laser Conference, 2002. IEEE, pages 99–100, December 2002.

[190] Wolf P., et al.: *Quantum Physics Exploring Gravity In The Outer Solar System: The Sagas Project*. Experimental Astronomy, 23(2):651–687, November 2008.

[191] Wright, C.: *Spectroscopic Characterization of Fluorite: Relationships Between Trace Element Zoning, Defects and Color*. Technical report, Miami University, Department of Geology, 2002.

[192] Xapsos M.A., et al.: *Co-60 Gamma Ray and Electron Displacement Damage Studies of Semiconductors*. IEEE Transactions on Nuclear Science, 41(6):1945–1949, December 1994.

[193] Xiang N., et al.: *Broadband Semiconductor Saturable Absorber Mirrors in the 1.55 Micrometer Wavelength Range for Pulse Generation in Fiber Lasers*. IEEE Journal Of Quantum Electronics, 38(4):369–374, April 2002.

[194] Ye, J.: *Absolute Measurement Of A Long, Arbitrary Distance To Less Than An Optical Fringe*. Optics Letters, 29(10):1153–1155, May 2004.

[195] Ye J., Cundiff S.T. (editor): *Femtosecond Optical Frequency Comb Technology*. Springer, 2005.

[196] Ye J., et al.: *Accuracy Comparison of Absolute Optical Frequency Measurement between Harmonic-Generation Synthesis and a Frequency-Division Femtosecond Comb*. Physical Review Letters, 85(18):3797–3800, October 2000.

[197] Zhang J., et al.: *Absolute Mode Number Determination of Frequency Combs*. Joint IFCS/EFTF Conference, pages 104–106, October 2007.

[198] Zotov K.V., et al.: *Radiation-Resistent Erbium-Doped Fiber For Spacecraft Applications*. 9th European Conference on RADECS, 2007.

[199] Zotov K.V., et al.: *Radiation Resistant Er-Doped Fibers: Optimization of Pump Wavelength*. IEEE Photonics Technology Letters, 20(17):1476–1478, September 2008.